MAGNETIC FIELD EFFECT IN ORGANIC FILMS AND DEVICES

by

Bhoj Raj Gautam

A dissertation submitted to the faculty of
The University of Utah
in partial fulfillment of the requirements for the degree of

Doctor of Philosophy

in

Physics

Department of Physics and Astronomy

The University of Utah

August 2013

THE UNIVERSITY OF UTAH GRADUATE SCHOOL

STATEMENT OF DISSERTATION APPROVAL

The dissertation of **Bhoj Raj Gautam**

has been approved by the following supervisory committee members :

Zeev Valy Vardeny	**,** Chair	**04/24/2013**
		Date
Christoph Boehme	**,** Member	**04/24/2013**
		Date
Oleg Starykh	**,** Member	**04/24/2013**
		Date
Kyle Dawson	**,** Member	**04/24/2013**
		Date
Ashutosh Tiwari	**,** Member	**04/24/2013**
		Date

and by **David Kieda** , Chair of

the Department of **Physics and Astronomy**

and by **Donna M. White**, Interim Dean of The Graduate School.

ABSTRACT

In this work, we focused on the magnetic field effect in organic films and devices, including organic light emitting diodes (OLEDs) and organic photovoltaic (OPV) cells.

We measured magnetic field effect (MFE) such as magnetoconductance (MC) and magneto-electroluminescence (MEL) in OLEDs based on several π-conjugated polymers and small molecules for fields $|B|<100$ mT. We found that both MC(B) and MEL(B) responses in bipolar devices and MC(B) response in unipolar devices are composed of two B-regions: (i) an 'ultra-small' region at $|B| < 1–2$ mT, and (ii) a monotonic response region at $|B| >\sim 2$mT. Magnetic field effect (MFE) measured on three isotopes of Poly (dioctyloxy) phenylenevinylene (DOO-PPV) showed that both regular and ultra-small effects are isotope dependent. This indicates that MFE response in OLED is mainly due to the hyperfine interaction (HFI).

We also performed spectroscopy of the MFE including magneto-photoinduced absorption (MPA) and magneto-photoluminescence (MPL) at steady state conditions in several systems. This includes pristine Poly[2-methoxy-5-(2-ethylhexyl-oxy)-1,4-phenylene-vinylene] (MEH-PPV) films, MEH-PPV films subjected to prolonged illumination, and MEH-PPV/[6,6]-Phenyl C61 butyric acid methyl ester (PCBM) blend, as well as annealed and pristine C_{60} thin films. For comparison, we also measured MC and MEL in organic diodes based on the same materials. By directly comparing the MPA and MPL responses in films to MC and MEL in organic diodes based on the same active layers, we are able to relate the MFE in organic diodes to the spin *densities* of the

excitations formed in the device, regardless of whether they are formed by photon absorption or carrier injection from the electrodes.

We also studied magneto-photocurrent (MPC) and power conversion efficiency (PCE) of a 'standard' Poly (3-hexylthiophene)/PCBM device at various Galvinoxyl radical wt%. We found that the MPC reduction with Galvinoxyl wt% follows the same trend as that of the PCE enhancement. In addition, we also measured the MPC response of a series of OPV cells. We attribute the observed broad MPC to short-lived charge transfer complex species, where spin mixing is caused by the difference, Δg of the donor/acceptor g factors; whereas narrow MPC is due to HFI within long-lived polaron-pairs.

To my parents, and family

TABLE OF CONTENTS

ABSTRACT ..... **iii**

LIST OF FIGURES ..... **ix**

ACKNOWLEDGEMENTS ..... **xvi**

CHAPTER

1. INTRODUCTION **1**

1.1 π-Conjugated Organic Semiconductors 1
1.2 Excitation Models for π-Conjugated Polymers 5
1.3 Major Excitations in π-Conjugated Polymers 6
1.3.1 Excitons 7
1.3.2 Polarons, Polaron Pairs and Bipolarons 9
1.4 Charge Transport in Organic Semiconductors 12
1.5 Organic Light Emitting Diodes 13
1.6 Magnetic Field Effects 15
1.7 Organic Photovoltaics 17

2. EXPERIMENTAL TECHNIQUES **20**

2.1 Materials 20
2.2 Organic Light Emitting Diodes Fabrication 21
2.3 Organic Light Emitting Diodes Characterization 26
2.3.1 Current-Voltage and Electroluminescence-Voltage Characteristics .. 27
2.3.2 Magnetoconductance and Magneto-electroluminescence 28
2.4 Organic Photovoltaic Device Fabrication 32
2.5 Organic Photovoltaic Device Characterization 32
2.5.1 Current-Voltage Characteristics 32
2.5.2 Magneto-photocurrent Measurement 35
2.6 Material Characterization 36
2.6.1 Linear Absorption Measurement 36
2.6.2 Photoinduced Absorption Measurement 38
2.6.3 Magneto-photoinduced Absorption Measurement 41
2.6.4 Photoluminescence and Magneto-photoluminescence Measurement 43

2.6.5 X-ray Diffraction Measurement 44

3. MAGNETIC FIELD EFFECT IN ORGANIC DIODES 48

3.1 Introduction 48
3.2 Experimental 49
3.3 Experimental Results and Discussion 50
3.3.1 Magnetoconductance Response in Organic Diodes at Ultra-small Fields 50
3.3.2 Magneto-electroluminescence Response in Organic Diodes at Ultra-small Fields 62
3.3.3 Illumination Effect on Magnetoconductance Response of MEH-PPV Devices 67
3.4 Conclusion 72

4. MAGNETIC FIELD EFFECT IN ORGANIC FILMS 73

4.1 Magnetic Field Effect on Excited State Spectroscopies of π-Conjugated Polymer Films 73
4.1.1 Introduction 73
4.1.2 Experimental 77
4.1.3 Experimental Results 79
4.1.3.1 Pristine MEH-PPV Films 79
4.1.3.2 Irradiated Pristine MEHPPV Films and Devices 81
4.1.3.3 Films and Devices of MEH-PPV/PCBM Blends 84
4.1.4 Discussion 86
4.1.5 Conclusion 92
4.2 Magnetic Field Effect Spectroscopy of C_{60} Based Films and Devices 93
4.2.1 Introduction 93
4.2.2 Experimental 95
4.2.3 Experimental Results 97
4.2.4 Discussion 105
4.2.4.1 Magneto-photoinduced Absorption; Narrow Component 107
4.2.4.2 Magneto-photoinduced Absorption; Δg Mechanism 109
4.2.4.3 Magnetoconductance and Magneto-photoluminescence 111
4.2.5 Conclusion 111

5. ORGANIC PHOTOVOLTAIC DEVICES 113

5.1 Efficiency Enhancement in Organic Bulk Heterojunction Photovoltaic Devices 113

5.1.1 Introduction 113
5.1.2 Experimental 115
5.1.3 Experimental Results and Discussion 117
5.1.3.1 Spin Enhanced Organic Bulk Heterojunction Photovoltaic Devices 117
5.1.3.2 Low Band Gap Organic Bulk Heterojunction Photovoltaic Devices 127
5.1.4 Conclusion 131
5.2 Magneto-photocurrent of Charge Transfer Complex in Organic Blends for Photovoltaic Applications 132
5.2.1 Introduction 132
5.2.2 Experimental 133
5.2.3 Experimental Results and Discussion 134
5.2.4 Conclusion 143

6. CONCLUSION 144

APPENDIX: LIST OF PUBLICATIONS 148

REFERENCES 149

LIST OF FIGURES

Figure

1.1 Chemical structures of π-conjugated organic semiconductors: Polyfluorine and P3HT are π-conjugated polymers whereas Alq_3 and Pentacene are small molecular semiconductor 3

1.2 Electronic orbitals and bonds in sp^2 hybridized carbon atoms, adapted from www.orgworld.de (a). A conjugated backbone with overlapped P_z orbitals (b). Chemical structure of trans-polyacetylene showing the alternation of carbon-carbon single and double bonds (c) 3

1.3 Various photoexcitations in conjugated polymers: polaron excitation (charge manifold; uncorrelated) with P1 and P2 transitions on the left and exciton (neutral manifold; correlated) bands on the right 9

1.4 Energy level diagrams and possible optical transitions in polaron-pairs 11

1.5 Energy levels and associated optical transitions of (a) positive, and (b) negative bipolarons 11

1.6 Typical device structure of an organic light emitting diode 14

1.7 Schematic of different processes (recombination, dissociation and intersystem crossing) in an OLED device 14

1.8 Summary of magnetic field effects on the singlet-triplet conversion of polaron pairs and physical effect yield with B 17

1.9 Typical device structure of BHJ OPV solar cell 19

1.10 Energy level diagram for typical OPV showing different electronic processes, figure adapted from Ref. [37] 19

2.1 Chemical structures of (a) H-DOO-PPV, (b) D-DOO-PPV, (c) C-13-DOO-PPV, (d) Rubrene, (e) PFO, (f) MEHPPV, (g) RR P3HT, (h) RRa P3HT, (i) PTB7, (j) C_{60} , (k) $PC_{61}BM$, and (l) $PC_{71}BM$ 22

2.2 ITO pattern on the substrate after etching (a). Top view of completed OLED device (b). The typical OLED device structure (c) 25

2.3 Typical I-V and EL-V characteristics of OLED device based on MEHPPV as an active layer at 10 K 28

2.4 The experimental set up for measuring the organic magnetic field effect in films and devices 30

2.5 Typical MC and MEL responses of an OLED based on MEHPPV as the active organic interlayer, measured at 10 K 31

2. 6 Standard 'AM1.5 spectrum', under which the integrated illumination intensity is 100 mW/cm2 33

2.7 The experimental set-up for measuring the I-V response of an OPV cell 34

2.8 Typical I-V characteristics of PTB7/PC70BM OPV cell with 3 wt% of 1,8-diiodooctane, under 'AM 1.5' illumination spectrum 34

2.9 MPC(B) response of PTB7/PC70BM-based OPV cell with 3 wt% of 1,8-diiodooctane, measured at room temperature 37

2.10 Typical optical density spectrum of MEHPPV film 38

2.11 The experimental setup for measuring the PA spectrum 40

2.12 The photoinduced absorption spectrum of an irradiated MEH-PPV film. The PA bands P_1 and $T+P_2$ are denoted 42

2.13 Magneto-photoinduced absorption response of irradiated MEHPPV film measured at50 K 44

2.14 Photoluminscence spectrum of Pristine MEHPPV film at 50 K 45

2.15 Magneto-photoluminscence response of pristine MEHPPV film measured at 50 K 45

2.16 X-ray diffraction patterns of a C_{60} film, where the background scattering was removed for clarity. The numbers represents various (hkl) Bragg bands 47

3.1 Magnetoconductance (MC) response vs. field, B in bipolar organic diodes based on: three isotopes of DOO-PPV Panel (a) shows MC(B) for $|B|<50$ mT; whereas panel (b) shows the *normalized* MC(B) measured with high field resolution, for $|B|<3$ mT (some MC responses are shifted vertically for clarity); MC_{max} is the saturation MC value at large B. ΔB is the HWHM for the normal MC(B) response,

as defined in (a); whereas MC_{min} and B_m are for the USMFE response, as defined in (b). Panel (c) summarizes B_m vs. ΔB for the MC(B) responses in (a) and (b); the straight line is guide to the eye 53

3.2 Magnetoconductance (MC) response vs. field, B in bipolar organic diodes based on MEH-PPV, PFO (MCx3), and rubrene RBRN; (MCx8). Panel (a) shows MC(B) for $|B|<50$ mT; whereas panel (b) shows the *normalized* MC(B) measured with high field resolution, for $|B|<3$ mT (some MC responses are shifted vertically for clarity). Panels (c) summarizes B_m vs. ΔB for the MC(B) responses in (a) and (b) 55

3.3 Normalized MC(B) response of a bipolar diode based on D-DOO-PPV for $|B|<0.5$ mT at (a) various bias voltages at T=10 K, and (b) various temperatures at V= 3.4 Volt; MC_{max} is defined in Figure 3.1. The insets in (a) and (b), respectively summarize MC_{min}/MC_{max} at various voltages at 10 K, and various temperatures at 3.4 Volt 56

3.4 Normalized MC(B) response for (a) $|B|<30$ mT, and (b) $|B|<2$ mT of hole- and electron-only *unipolar* diodes based on MEH-PPV, measured at room temperature and V=3 Volt and 20 Volt, respectively. For clarity, the MC(B) responses are multiplied by a factor in (b) 57

3.5 Normalized MC(B) response for (a) $|B| < 60$mT, and (b) $|B| < 3$mT of hole-only unipolar diodes based on H- and C13-DOO-PPV, measured at room temperature 59

3.6 Calculated spin energy levels and magnetoconductance. (a)Example of calculated spin energy levels vs. B for a spin pair with isotropic HFI; a_1=3, a_2=3 mT, and J=0. Note the multiple level-crossing at B=0. (b) Calculated MC(B) response for a SP with axially symmetric HFI averaged over all magnetic field directions. The isotropic HFI is the same as in (a). The anisotropic HFI component is $a_{zz}=0.15a_i$ for the respective SP constituent 63

3.7 Magneto-electroluminescence (MEL) response vs. field, B in bipolar organic diodes based on MEHPPV polymer as an active layer. Panel (a) shows MEL(B) for $|B|<60$ mT; panel (b) shows the MEL(B) measured with high field resolution, for $|B|<3$ mT 65

3.8 Magneto-electroluminescence (MEL) response vs. field, B in bipolar organic diodes based on rubrene small molecule as active layer. Panel (a) shows MEL(B) for $|B|<60$ mT; panel (b) shows the MEL(B) measured with high field resolution, for $|B|<3$ mT 66

3.9 Magneto-conductance MC(B) response in bipolar, hole-only and electron-only unipolar organic diodes based on MEHPPV. The latter responses are multiplied by a factor of 100 and 10, respectively 69

3.10 Magneto-conductance MC(B) response in pristine and UV irradiated (20 minutes) MEH-PPV OLED, measured at 10 K 70

3.11 MC(B) response of (a) hole-only and (b) electron-only unipolar devices at 10 K, illuminated with 532 nm laser for 30 min at different power 71

4.1 Schematic illustration of the magnetic field dependent pump-probe PA processes. (a) The pump beam with above gap photon energy $h\upsilon_L$ excites the polymer MEH-PPV to the singlet exciton (SE) level ($S_0 \rightarrow S_1$). The SE relaxes via intersystem crossing to a triplet exciton (TE) or ionizes into separate charges forming polaron pair, PP ($S_1 \rightarrow X_0$). The steady state density of the X species is controlled by the spin dependent decay coefficient, κ. The incandescent probe beam monitors the photoinduced absorption, PA ($X_0 \rightarrow X_1$, PA_X), which is proportional to the X_0 steady state density. In a magnetic field $B>0$, X_0 splits according to its spin multiplicity, and the decay rate of each spin sub-level becomes field dependent, resulting in a B-dependent density and PA_X (thus forming MPA_X)..... 76

4.2 Excited state spectra (PA and PL) and magnetic field effects in pristine MEH-PPV films. (a) The triplet PA band, PA_T at B=0 and 100 mT (black and red lines, respectively), respectively, generated using a laser excitation at $h\upsilon_L$=2.54 eV @ I_L=200 mW/cm^2, and their difference spectrum $\Delta PA_T=[PA_T(100mT)-PA_T(0)]$ (blue line). The region near the peak is magnified (within a circle). Right inset: PL spectrum at B=0 (black line) and 100 mT (red line), respectively. The lines in the circles show the data on a higher resolution scale. (b) $MPA_T(B)$ response measured at 1.37 eV probe, for various laser excitation intensities (normalized). (c) MPL(B) response measured at 2.05 eV probe for various laser excitation intensities (normalized). (d) Model calculations of $MPA_T(B)$ response using the TE mechanism (blue line, corresponds to the 10 mW data in (b)) and TTA mechanism (green line, corresponds to the 400 mW data in (b)) mechanisms; see text. (e) Model calculation of MPL(B) response using the model of singlet exciton quenching by TE (SE-TE collision, see text)..... 78

4.3 Excited state spectra and magnetic field effects in UV irradiated MEH-PPV film and in organic light emitting diode. (a) PA spectrum at I_L=100 mW/cm^2 for B=0 (black line) and B=100 mT (red line), respectively, and their difference spectrum, $\Delta PA=[PA(100mT)-PA(0)]$ (blue line) in MEH-PPV film. (b) MPA(B) response measured at 1.4 eV probe for various laser excitation intensities (normalized). (c) MEL(B) and MC(B) responses in MEH-PPV diode. (d) Model calculations of $MPA_{PP}(B)$ response in MEH films using the PP mechanism (see text). (e) MPA(B) response at 1.1 eV probe up to B=1.5 mT (filled squares) and B=60 mT (blue line, inset) 82

4.4 Excited state spectra and magnetic field effects in MEH-PPV/PCBM film and diode. (a) PA spectrum of MEH-PPV film at I_L=mW/cm^2 for B=0 (black line) and B=15 mT (red line), respectively, and their difference spectrum, $\Delta PA=PA(15mT)-PA(0)$ (blue line). (b) MPA(B) response measured at 1.37 eV

probe for various laser excitation intensities (normalized). Inset: high resolution data, showing USMPA peaks at |B|~0.1 mT. This data was measured upon shielding from the earth magnetic field and any stray field. (c) MC(*B*) response in a diode at various bias voltages, V. (d) and (e) Model calculations of $MPA_{PP}(B)$ and MC(B) response, respectively, using the 'Δg + HFI' mechanism (see text, Section 4.1.4) 85

4.5 The X-ray diffraction pattern of annealed and pristine C_{60} films in the range (a) $2\theta = 6\text{-}25^0$, (b) $2\theta = 8\text{-}13^0$; the miller indices are denoted on the Bragg scattering bands. The inset in (b) shows the chemical structure of C_{60}. TEM images of annealed (c) and pristine (d) C_{60} films; the grey grains are C_{60} microcrystallites. The scale bar is 50 nm. Also shown are the grain size distributions extracted from the TEM images for the annealed (e) and pristine (f) C_{60} films 98

4.6 Photomodulation spectra of annealed (a) and pristine (b) C_{60} films at T=50 K and I_L=0.2W/cm^2 for *B*=0 (black lines) and *B*=180 mT (red lines). The blue negative lines are the difference spectra ΔPA=PA(*B*=180 mT)-PA(0) 100

4.7 MPA(*B*) response of an annealed C_{60} film at various pump excitation intensities, measured at photon energy E=1.8 eV and T=50 K. (b) The spectra $\Delta PA(B_1,B_2,E)$ for B_1=0, B_2=20 mT (black line, lower curves), and B_1=20 mT, B_2=180 mT (blue line, upper curves) for I_L=1.5 W/cm^2. The smooth green and red lines through the data are to guide the eye, and show the TE- and polaron-related MPA bands, respectively 101

4.8 MC(*B*) response of an annealed C_{60} diode for various bias voltages measured at T=10 K. (a) high resolution for |B|<0.2 T; (b) low resolution for |B|<1 T. (c) MC(*B*) response of devices based on ^{13}C-rich C_{60} (black line) compared with that of devices based on regular C_{60} (red line) for |B|<40 mT 104

4.9 PL spectrum (a) and MPL(*B*) response (b) of annealed C_{60} film at T=50 K 106

4.10 Model fitting for MPA(*B*) of C_{60}. (a) Low field, |B|<40 mT. The blue line is calculated based on the TE mechanism (see text); the black points are measured MPA(*B*) taken from Fig. 4.7 (a). (b) Intermediate field, |B|<0.2 T. Blue line: calculated using the 'Δg mechanism' (see text); black line: measured MPA(*B*) respectively 109

5.1 J-V characteristics of P3HT:PCBM OPV devices at different percentages of PCBM under AM 1.5 illumination 118

5.2 J-V characteristics of OPV solar cells of pristine P3HT/PCBM blend (η = 3.4%, Black line), the blend doped with 3 wt% galvinoxyl radicals (η = 4.0%, Red line) and the blend doped with 3 wt% precursor (η = 2.8%, Blue line) under AM1.5

'sun illumination' condition. The inset shows the galvinoxyl molecular structure.. 119

5.3 The change in OPV device properties with galvinoxyl-additive concentration; J_{sc} (triangles) and η (squares) are shown versus galvinoxyl wt% in the P3HT/PCBM blend. η of OPV devices doped with galvinoxyl precursor that does not possess spin 1/2 radical is also shown for comparison (circles). 120

5.4 MPC response of OPV devices doped with galvinoxyl up to field, *B* of 190 mT. The inset summarizes the MPC value at 190 mT versus galvinoxyl wt%..... 121

5.5 The UV/Vis absorption spectrum of pure galvinoxyl (dash-dot line), pristine (dashed line) and doped (solid line) P3HT/PCBM blend (a). The EQE spectrum of OPV solar cells based on pristine (dashed line) and galvinoxyl-doped (solid line) P3HT/PCBM blend (b). The XRD pattern of pristine (green dash) and doped (red solid) P3HT/PCBM films (c). PL spectrum of pristine (dashed line) and doped (solid line) P3HT/PCBM. The phonon replicas are assigned. Norm., normalized (d)..... 123

5.6 The spin exchange mechanism where the photogenerated PP at the D–A domain interface changes its spin configuration from singlet to triplet augmented by the galvinoxyl spin 1/2 radical (a). The calculated HOMO, LUMO, and SOMO levels of P3HT, PCBM, and galvinoxyl that show a clear resonance between the radical and acceptor LUMO levels (b). 126

5.7 Linear absorption spectrum of P3HT and PTB7 polymer 128

5.8 Linear absorption spectrum of PTB7 and its blend with $PC_{71}BM$..... 128

5.9 J-V characteristics of PTB7/ $PC_{71}BM$ device under AM 1.5 illumination..... 129

5.10 J-V characteristics of PTB7/$PC_{71}BM$ OPV devices at different percentage of dio under AM 1.5 illumination, inset shows the chemical structure of dio 130

5.11 The PCE and MPC(B) response of RRa P3HT/$PC_{61}BM$ (1:2) based OPV cell. 135

5.12 The PCE and MPC(B) response of MEH-PPV/$PC_{61}BM$ (1:4) based OPV cell. 136

5.13 The PCE and MPC(B) response of RR P3HT/$PC_{61}BM$ (1.2:1) based OPV cell.137

5.14 The PCE and MPC(B) response of PTB7/$PC_{71}BM$ (1:1.5) based OPV cell 138

5.15 The PCE and MPC(B) response of PTB7/$PC_{71}BM$ (1:1.5) based OPV cell with 3 wt% of 1,8-diiodooctane..... 139

5.16 PA spectra of a ~100 nm thick film of P3HT/PCBM (1.2:1 by weight) blend at B=0 (black line) and B=150 mT (red line). The difference ΔPA (enlarged) is plotted as a blue line (a). The MPA(B) response monitored at E_1=0.35 eV (b) . 140

ACKNOWLEDGEMENTS

I would like to express my utmost gratitude to my advisor, Prof. Zeev Valy Vardeny, for his sincere and unfailing support throughout my thesis and throughout my years at the University of Utah. His knowledge, patience, and encouragement were instrumental to the completion of this study. I must express my sincere thanks to Prof. Eitan Ehrenfreund for his theoretical guidance and Prof. Tho Nyugen for his research guidance. I would also like to thank my supervisory committee members, Professors Christoph Boehme, Oleg Starykh, Kyle Dawson, and Ashutosh Tiwari for their encouraging discussions and suggestions.

I would like to thank Dr. Randy Polson, Dr. Mathew Delong, and Mr. Leonard Wojcik for their help and suggestions. My sincere thanks is extended to my current group members, Tek Prasad Basel, Dr. Dali Sun, Ella Olejnik, Uyen Huynh, Yaxin Zhai, Ryan McLaughlin, and Peter Peroncik for their help, support, and suggestions. I would not forget my former group members Dr. Bill Pandit, Dr. Golda Hukic Markosian, Dr. Ye Zang, Dr. Sanjeev Singh, and Dr. Maria Navas for their help.

I am indebted to my family for their love, care, support, and inspiration. I must express my gratitude to Dipa Sharma, my wife, for her continuous support and encouragement. Also, thanks goes to my brother in law Deepesh Poudel and friend Sajjan Koirala for their valuable suggestions.

CHAPTER 1

INTRODUCTION

For a long time, organic materials have been associated with electrical insulators. Research on organic semiconductors was boosted after the discovery of the highly conducting oxidized iodine-doped polyacetylene [1]. Although to date, inorganic semiconductors are still the most popular materials in the electronic industry, the unique properties of organic semiconductors such as electroluminescent properties, flexibility, solubility, light weight, low cost, and easily modified band gap make these semiconductors very attractive for a number of novel optoelectronic applications such as: organic light emitting diodes (OLEDs) [2, 3], organic field effect transistors (OFETs) [4], organic photovoltaic cells (OPVs) [5, 6], organic spin valves [7, 8], thin film magnetometers [9], biological sensors, etc. In this chapter, we will give a brief review of π-conjugated organic semiconductors and their use in OLEDs and OPV cells. The focus of this work will be the magnetic field effect in organic semiconductor films and devices.

1.1 π-Conjugated Organic Semiconductors

Π-conjugated organic semiconductors are divided into two groups based on their molecular weight, namely polymers and small molecules. Chain-like macromolecules

with high molecular weight (>1000 g/mol) are polymers that are soluble and can be deposited easily, whereas materials with molecular weight less than 1000 g/mol are small molecules and are usually deposited by thermal evaporation. Both of these groups have a cocommon π-conjugated chemical structure, as shown in Figure 1.1. Π-conjugated semiconductors are unsaturated carbon compounds with alternating single and double bonds between the carbon atoms, as shown in Figure 1.2. The sp^2p_z hybridization causes three electrons to establish strong planar σ-bonds with neighboring atoms and one electron to be bound in π-bond perpendicular to the polymer backbone. The π-electrons are delocalized over many carbon atoms along the chain, giving the relatively high conducting properties [10]. These delocalized electrons occupy the bonding π–orbitals while antibonding π*–orbitals remain empty. The bonding π–orbitals form the highest occupied molecular orbitals (HOMO) and antibonding π*–orbitals form the lowest unoccupied molecular orbitals (LUMO), which are roughly equivalent to the inorganic semiconductor's valence and conduction band edges, respectively. The energy gap between HOMO and LUMO lies in the range 1.4-3.0 eV in most of the organic semiconductors, which makes them promising for applications in optoelectronic operation in the visible spectral range By changing the extent of delocalization, the gap between occupied and empty states can be altered, which makes them interesting in both academic and industrial research. The π- electrons are delocalized over many carbon atoms over the chain and hence, the quantum mechanical wave function is confined to a single chain. Π-conjugated organic semiconductors are often treated as one-dimensional systems with half-filled electronic bands as there is one π-electron per carbon atom. By taking an account of either electron-phonon interaction or electron-electron interactions

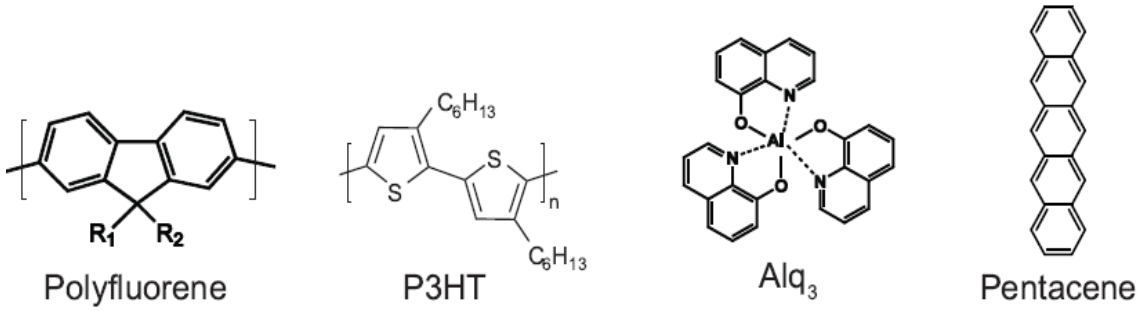

Figure 1.1. Chemical structures of π-conjugated organic semiconductors: Polyfluorine and P3HT are π-conjugated polymers whereas Alq_3 and Pentacene are small molecular semiconductors.

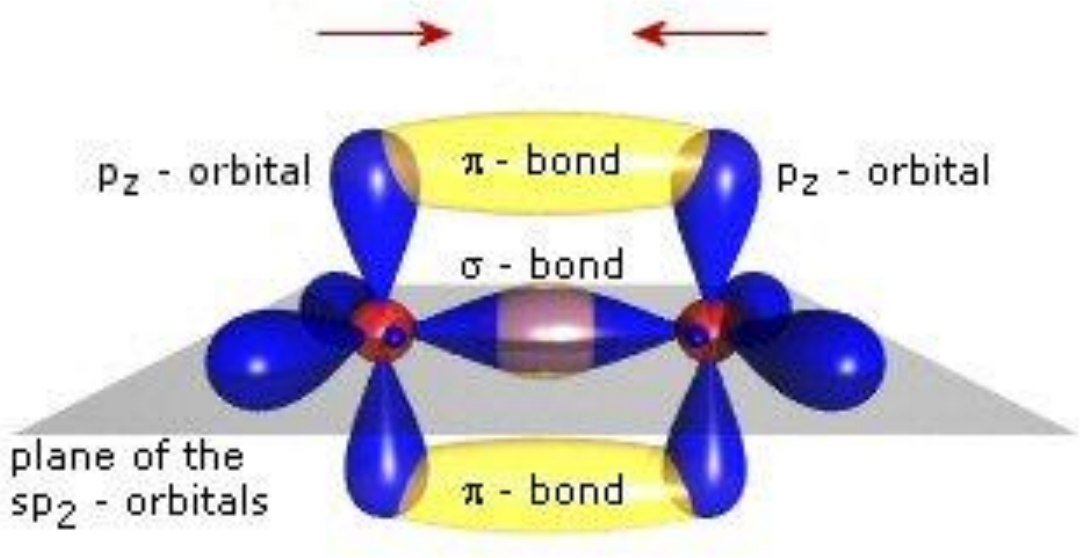

(a)

Figure 1.2. Electronic orbitals and bonds in sp^2 hybridized carbon atoms, adapted from www.orgworld.de (a). A conjugated backbone with overlapped P_z orbitals. (c) Chemical structure of trans-polyacetylene showing the alternation of carbon-carbon single and double bonds (b).

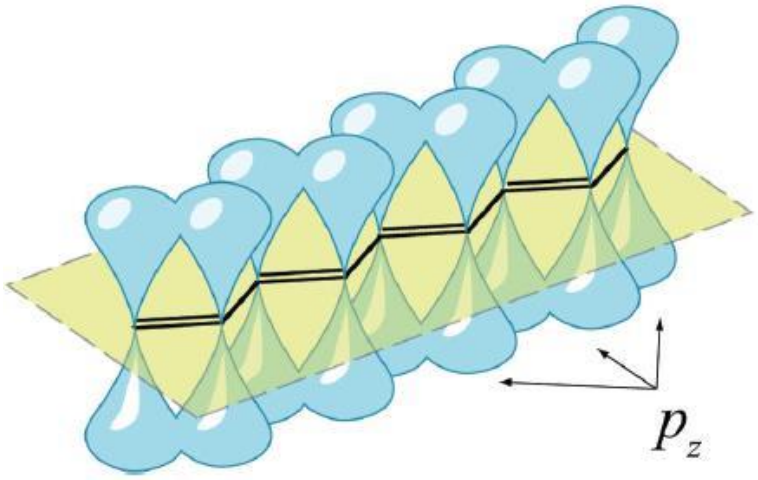

(b)

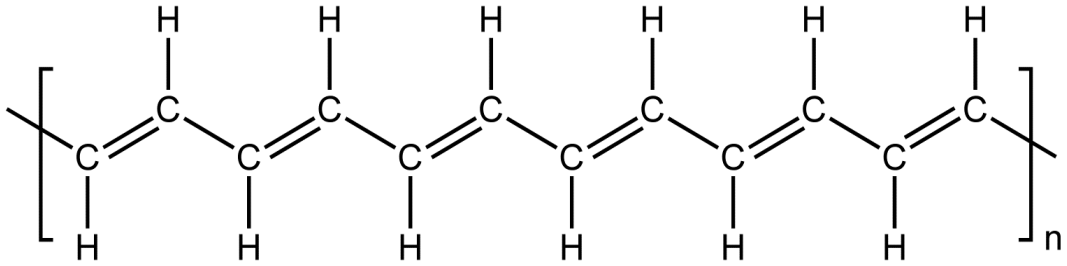

(c)

Figure 1.2. Continued

among the π-electrons, the formation of the band gap can be explained.

1.2 Excitation Models for π-Conjugated Polymers

Excitations in π-conjugated polymers are described by using several models. Su, Schrieffer, and Heeger proposed a model, named SSH model, for trans-polyacetylene (t-$(CH)_x$), based on tight binding approximation calculation by taking an account of electron phonon interaction and neglecting the electron-electron interaction [11]. In this model, they applied a semiclassical Huckel Hamiltonian. The Hamiltonian contains the lattice kinetic energy, which is treated classically, and the electron-phonon interaction, which is treated quantum mechanically, as written in Equation 1.1:

$$H_{SSH} = \frac{k}{2}\Sigma_n (u_n - u_{n-1})^2 + \frac{M}{2}\Sigma_n (\frac{du_n}{dt})^2 - \Sigma_{n,s}(t_0 + \alpha(u_{n+1} - u_n))(C^+_{n+1,s}C_{n,s} + C^+_{n,s}C_{n+1,s}) \quad (1.1)$$

where t_0 is the hopping integral between the nearest neighbors for an undistorted chain, α is the electron lattice coupling constant, and $C^+_{n,s}$ and $C_{n,s}$ are the creation and annihilation operators of an electron on site n with spin s. k is the spring constant due to π-electrons and u_n is the deviation of n^{th} site from the equilibrium position in an undistorted chain with equal distance between sites.

According to the SSH model, dimerization caused by strong electron-phonon interaction lowers the system energy and creates an energy gap $E_g=4\alpha u$ where u is the dimerization amplitude in equilibrium. Thus, the occupied electronic states in equilibrium are lowered, resulting in a more stable configuration. Therefore, the system no longer acts

as a one-dimensional metal, but instead behaves as a semiconductor with a direct energy gap.

On the other hand, the Hubbard model that includes electron-electron interaction and 3D intrachain coupling can also explain the energy levels of charged and neutral excitations. Although this model includes the coulomb repulsion of two electrons on the same site, it ignores the electron-phonon interaction, which is quite strong in the polymer system. The model which includes both interactions, i.e., combination of SSH and the Hubbard model, is more realistic to explain the energy levels of excitations in the class of π-conjugated polymers. The Pariser-Parr-Pople (PPP) is such a model [12].

1.3 Major Excitations in π-Conjugated Polymers

Two kinds of electronic excited states (excitations), namely charged (polarons) and neutral (excitons), are dominant in π-conjugated polymers. Upon photoexcitation (with above-gap photon energy), neutral, spinless excitations called singlet excitons (SE) are generated. The SE may either radiatively recombine; or convert into long-lived neutral excitations, i.e., triplet excitons (TE) via intersystem crossing; or separate into positive and negative charge excitations (polarons), some of which may form long-lived polaron pairs (neutral excitations). On the other hand, upon electrical excitation, charged excitations are injected; these may recombine to form neutral excitations or other types of charged excitations [13]. In the following, we summarize the main properties of the charged and neutral photoexcitations.

1.3.1 Excitons

Excitons are electron-hole pairs that are bound through their mutual coulombic interaction. Upon photon absorption, an electron is promoted from lower energy level to higher energy level and an exciton is generated. This excitation causes structural relaxation of the surrounding geometry, which leads to an exciton binding energy E_b. Typical E_b is between 0.3-0.5 eV in most π-conjugated polymers.

Depending upon the mutual spin configuration, an electron and hole in an exciton may form singlet or triplet state with total spin 0 or 1, respectively; both species are neutral. The wave function describing two particle systems (exciton) is asymmetric in spin and electronic coordinates and can be obtained from Slater determinant:

$$\Psi = \frac{1}{\sqrt{2}} \begin{vmatrix} \psi_i(r)\chi_i(\sigma) & \psi_i(r')\chi_i(\sigma') \\ \psi_j(r)\chi_j(\sigma) & \psi_j(r')\chi_j(\sigma') \end{vmatrix} \tag{1.2}$$

where $\psi_i(r)$ and $\sigma_i(r)$ represent the electronic and spin part of wave function.

The wave functions that have a different total quantum number, S, constructed from the above equation are:

$$\Psi^{S=0} = \frac{1}{2}[\psi_1(1)\psi_2(2) + \psi_2(1)\psi_1(2)][\uparrow(1)\downarrow(2) - \uparrow(2)\downarrow(1)] \tag{1.3}$$

$$\Psi^{S=1} = \frac{1}{2}[\psi_1(1)\psi_2(2) - \psi_2(1)\psi_1(2)][\uparrow(1)\downarrow(2) + \uparrow(2)\downarrow(1)] \tag{1.4}$$

$$\Psi^{S=1} = \frac{1}{2}[\psi_1(1)\psi_2(2) + \psi_2(1)\psi_1(2)][\uparrow(1)\uparrow(2)] \tag{1.5}$$

$$\Psi^{S=1} = \frac{1}{2}[\psi_1(1)\psi_2(2) + \psi_2(1)\psi_1(2)][\downarrow(1)\downarrow(2)] \tag{1.6}$$

where ↑and ↓ represent the spin up and spin down projection of χ. Singlet and triplet energy levels are degenerate in the noninteracting case. However, in the presence of spin-spin interaction such as an exchange interaction, they are nondegenerate with triplet taking the lower energy. The energy bands in excitons are shown in the right panel of Figure 1.3.

Although a singlet exciton is formed immediately after photoexcitation, it may convert into a long-lived triplet exciton within ~10 ns or less via intersystem-crossing that results by a spin flip of one of the electrons involved in the exciton due to spin orbit coupling, hyperfine interaction, or the existence of radical impurities on the chains. The excited singlet state may recombine radiatively by emitting light in the form of fluorescence (PL). This process is usually fast with a lifetime of ~100 picoseconds. As the optical transition from the triplet lower state to the ground state is forbidden, the radiative emission from the excited triplet state, namely phosphorescence (PH), is usually weaker in organic materials. The transition may be possible if one of the two paired electrons spins flips due to spin orbit interaction. However, the optical transition of the triplet exciton is relatively small, resulting in long lifetime, of the order of milliseconds [14].

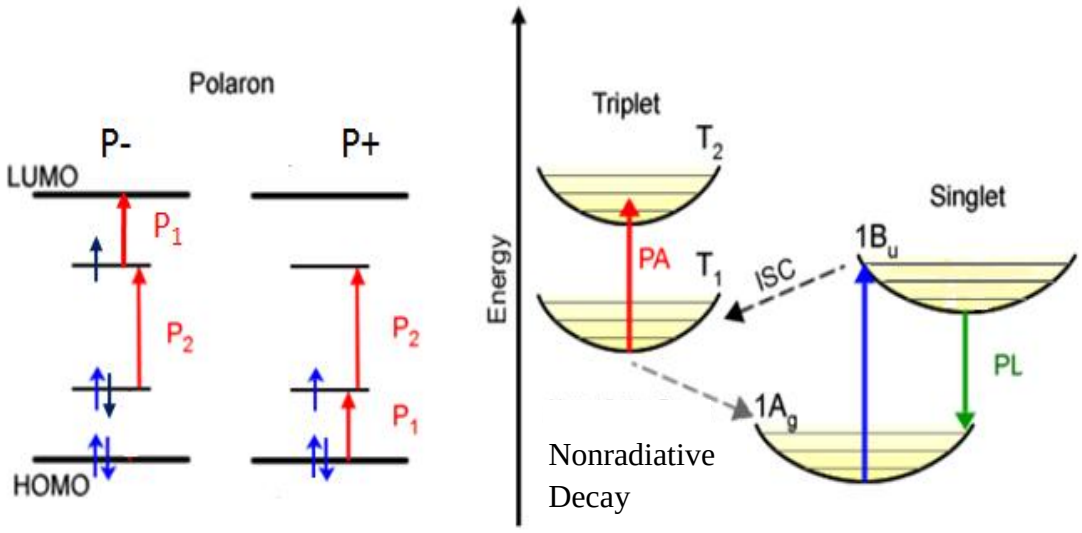

Figure 1.3. Various photoexcitations in π-conjugated polymers: polaron excitation (charge manifold; uncorrelated) having P_1 and P_2 transitions on the left, and exciton (neutral manifold; correlated) bands on the right.

1.3.2 Polarons, Polaron Pairs and Bipolarons

The interaction between neighboring molecules in an organic material in solid state is due to Van der Waals forces, which are much weaker than the covalent and ionic bonds in inorganic materials. As a consequence of this, organic materials are less rigid than inorganic materials. Therefore, the charge carrier that propagates in organic material is able to distort the host material and thus form a quasi-particle called a polaron.

The polaron is charged negative (P^-) or positive (P^+), and has spin ½. It has two symmetrical, localized states within the gap and has two allowed below-gap optical transitions P_1 and P_2, as shown in Figure 1.3. Doping-induced absorption, charge injection through metallic electrodes, photo-doping, i.e., exciting the sample with photon

absorption, are some methods for creating polarons in organic materials. Polaron transport from one chain to another is usually described by the hopping process between the localized states.

A Polaron pair (PP) is a bound pair of two oppositely charged polarons (P^+ and P^-), formed on two adjacent chains. The PP binding energy is mainly Coulombic. The PPs are the intermediate step between free polarons and excitons. These are the prerequisite for the formation of singlet and triplet excitons in OLEDs, and hence, their related physics is very important for device applications. In optical excitation, PPs are generated by the relaxation of higher energy singlet excitons. The species keeps the original spin 0 configuration and is hence dubbed a geminate pair. Upon electrical excitation, the electrons and holes that are injected into the active layer via the metal electrodes capture each other by Coulomb interaction and form PPs; these are nongeminate PPs. The nongeminate PPs can have spin 0 or 1 with high probability of having triplet configuration because of the degeneracy of the spin sublevels (in fact 3 to 1). The energy levels and possible transitions for PPs are shown in Figure 1.4.

When two polarons with the same charge come together with opposite spins on the same site, the resulting species with energy lower than two separate polarons is called a bipolaron. A bipolaron can either be doubly positive ($BP^{+\,+}$) or doubly negative ($BP^{-\,-}$). A bipolaron has two in-gap electronic states (like the polaron), but has only one allowed optical transition, as shown in Figure 1.5.

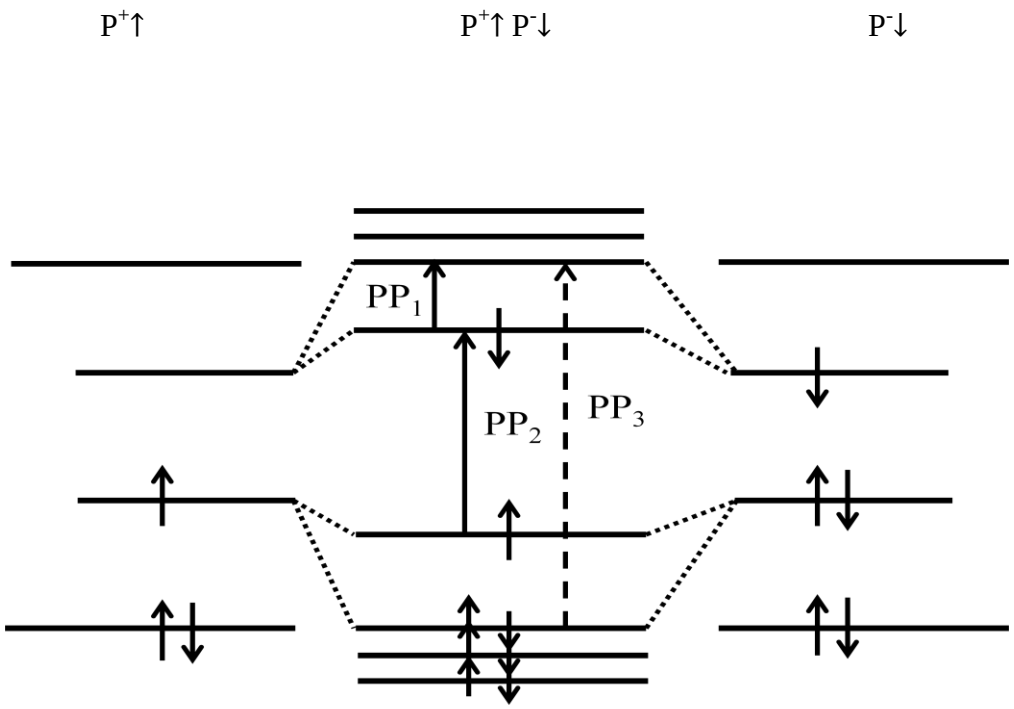

Figure 1.4. Energy level diagrams and possible optical transitions in polaron-pairs.

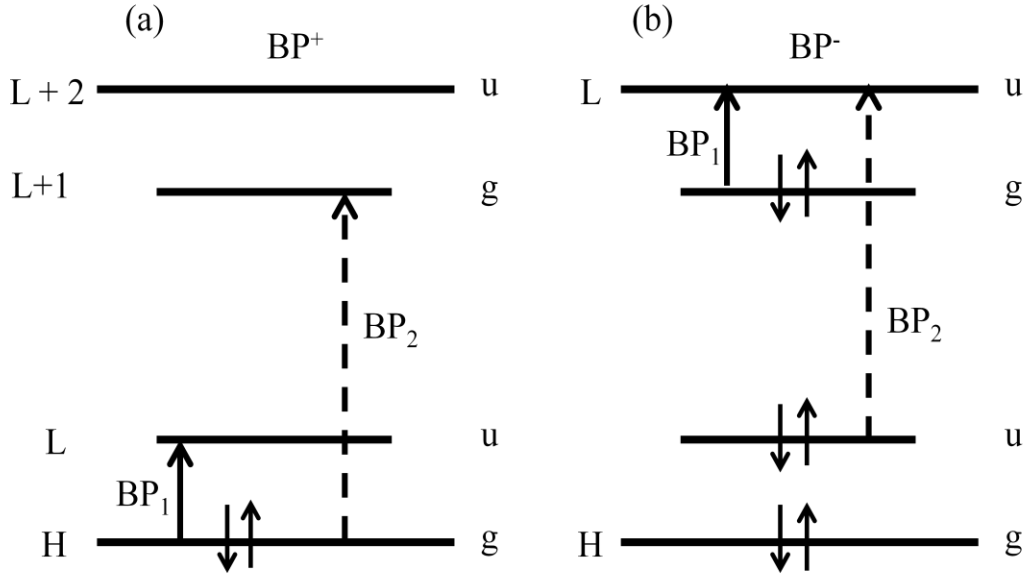

Figure 1.5. Energy levels and associated optical transitions of (a) positive, and (b) negative bipolarons

1.4 Charge Transport in Organic Semiconductors

Most of the organic semiconductor films are grown either by vacuum deposited small molecules or from solution processed polymers. Irregular packing of molecules due to vacuum deposition or spin coating causes energetic disorder in the HOMO and LUMO levels. The distribution of chain length, kinks, and twists present in polymer chains also causes structural, and hence, energetic disorder. Therefore, the HOMO and LUMO levels are distributed, and the band conduction transport concept (i.e., relaxation time approximation) does not apply to organic semiconductors.

As a result of the energetic disorder in organic semiconductors, charges are localized on molecular sites. Charge transport occurs via phonon-assisted tunneling or hopping [15] between the localized states in disordered materials and depends strongly on the parameters like temperature, electric field, traps present in the material, etc. For hopping, charge transport is very poor. The probability to hop from one energetic site to another, described by Miller-Abrahams formalism [16], is given by:

$$p = \upsilon_0 \exp(2\alpha R_{ij}) \begin{cases} \exp\left(-\dfrac{E_j - E_i}{K_B T}\right) & E_j > Ei \\ 1 & E_j < E_i \end{cases} \qquad (1.7)$$

where α is the inversion localization radius of the electronic wave function, R_{ij} is the distance between the localized sites i and j, and K_B is the Boltzmann constant. The disorder in the position and energy of hopping sites leads to much smaller mobility than via delocalized band states, as in inorganic semiconductors.

1.5 Organic Light Emitting Diodes

The first organic light emitting diode (OLED) based on the small molecule material (Alq_3) was demonstrated by Tang and Van Slyke in 1987 [17] and a polymer-based OLED was demonstrated three years later by Burroughs et al [2]. Extensive research activities were then carried out to optimize the device parameters and understand the physical processes that occur during OLED operation.

Charge carrier injection, charge carrier transport, polaron pair, followed by exciton formation and exciton decay (light emission) are the four important electronic processes that occur when OLED is in operation. Figure 1.6 shows a typical OLED structure. Here, the large work function material PEDOT:PSS is used as a hole transport layer whereas the low work function metal calcium is used as an electron transport layer. Electroluminescence in the OLEDs results from recombination of polaron pairs (PP) in the spin singlet configuration. The electrons and holes that are injected into the active layer via the metal electrodes can form loosely bound polaron pairs, which are the precursor of excitons. Following the PP generation, they may undergo three possible processes. They (i) may combine to form excited state singlet excitons (SE) and triplet excitons (TE), (ii) can dissociate into free charge carriers again, or (iii) can exchange spins via intersystem crossing (ISC). SEs may decay radiatively, resulting in electroluminescence. The long-lived TEs may decay nonradiatively or show delayed fluorescence via the process of triplet-triplet annihilation. The schematic of the different electronic processes in OLED such as recombination, dissociation, and intersystem crossing are shown in Figure 1.7.

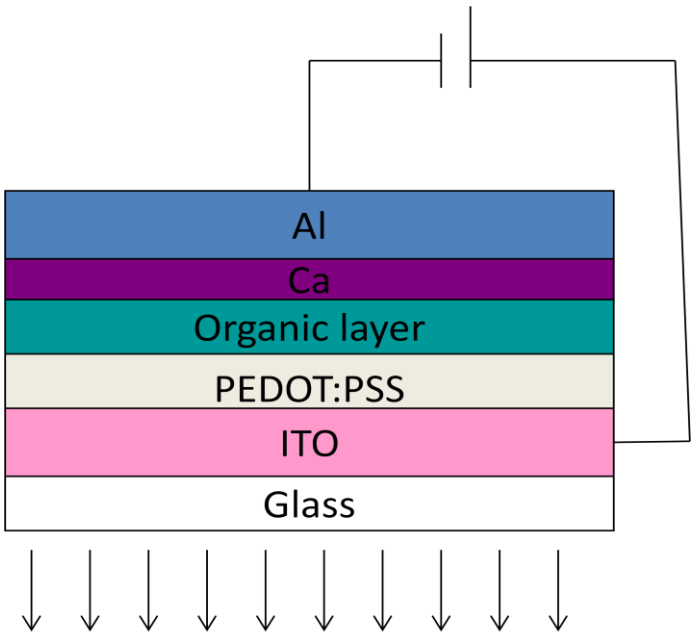

Figure 1.6. Typical device structure of an organic light emitting diode.

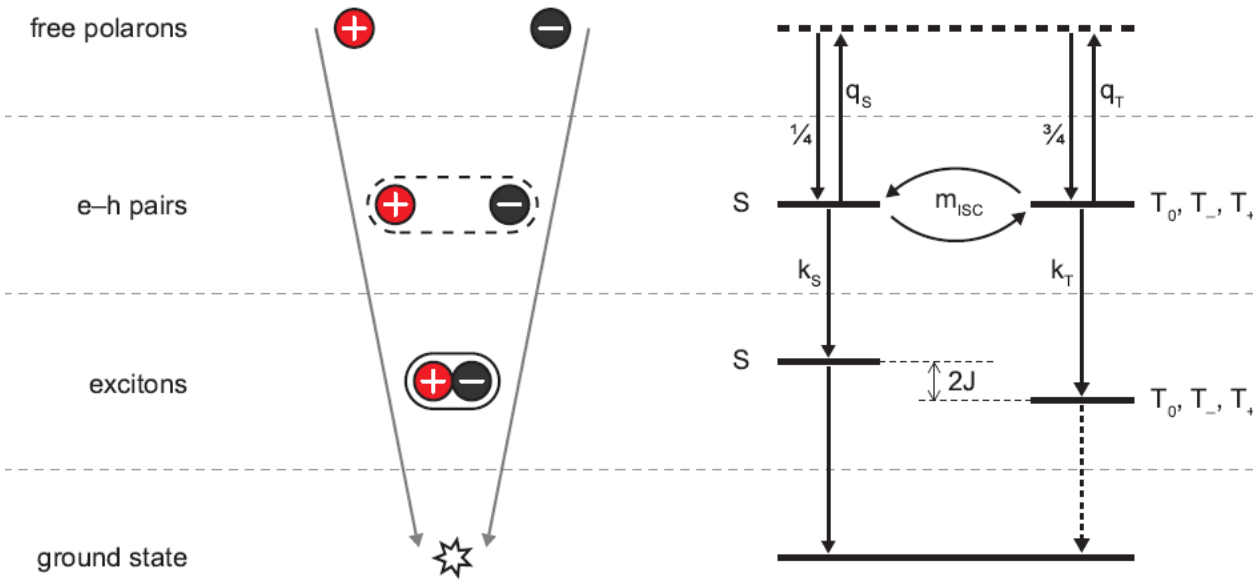

Figure 1.7. Schematic of different processes (recombination, dissociation, and intersystem crossing) in an OLED device. Figure adapted from Ref. [18].

1.6 Magnetic Field Effects

Magnetic field effects include the field-induced changes in chemical and bio-chemical reaction yields, magneto-conductance, magneto-electroluminescence, magneto-phosphorescence, magneto-photoconductance, etc. and have been intensively studied over the recent years [19-33]. Various mechanisms that account for the magnetic field effects (MFE) have emerged from these studies. This includes (a) spin-mixing by the hyperfine (HF) interaction within polaron pairs (PP) and bipolarons, (b) the difference, Δg, in the electron and hole g-factors, and (c) a number of mechanisms that involve triplet excitons (TE).

The polaron pair mechanism accounts for the spin mixing between the singlet-triplet (S-T) polaron pairs that can be influenced by weak magnetic interactions such as Zeeman and hyperfine. If neither spin couples to any magnetic nuclei (hyperfine coupling constant A_i is zero for both of them), then to have S-T conversion, they must have different g values. The precession frequency of the two individual spins transforms singlet pair state to triplet pair state, and vice versa, driven by the difference in precision frequencies, i.e., $(g_1-g_2)\mu_B \Delta g B/\hbar$. It can be seen that this mechanism is applicable only in the presence of external magnetic fields (B), and that the spin mixing frequency increases with increase in external magnetic field. In contrast, in the presence of hyperfine interaction, S-T conversion at zero B may occur between the singlet state and all three triplet sublevels. With increasing B field, the hyperfine interaction (HFI)-driven spin mixing decreases and saturates at fields higher than the hyperfine coupling constant. If we take into account the exchange interaction, J, there is no S-T conversion at zero B, as S and T levels are separated by exchange energy (2J). However, with increasing B field,

S and T_{+1} or T_{-1} can exchange the spin at a certain field called the level-crossing field (B_{LC}). S-T conversion rate increases suddenly at B_{LC} through the hyperfine field. Figure 1.8 shows the magnetic field effects on the S-T mixing of the polaron pairs and the physical effect yield with B [31].

The bipolaron model proposed by Bobbert et al. [24] based on the experimental observation of magnetic field effect in unipolar devices suggests the influence of magnetic field on the mobility of charge carriers and hence the current. The model is based on the competition between B-dependent bipolaron formation and B-independent hopping to empty sites. Using Monte Carlo simulation, two different line shapes in agreement with the experimental observation were shown to exist. A crucial point of this model is that carrier mobility and current density in a device are directly affected by the probability of magnetic field dependent bipolaron formation.

Desai et al. [22] proposed another model to explain the magnetic field effect observed in organic diodes. These authors considered the reduction in carrier mobility by polaron scattering from triplet excitons. They assumed that magnetic field acts on the intersystem crossing of singlet and triplet excitons, thereby decreasing the triplet concentration, consequently decreasing the scattering and, in turn, increasing the mobility.

Recently, we observed the magneto-photoinduced absorption (MPA) and magneto magneto-photoluminscence (MPL) in organic polymer films. We explained the MPA observation in terms of triplet-triplet annihilation (TTA) and spin-mixing among the triplet spin sublevels, in addition to the spin mixing in PP and Δg mechanism that are viable in polymer/fullerene blends. Since the PL is affected by the nonradiative decay

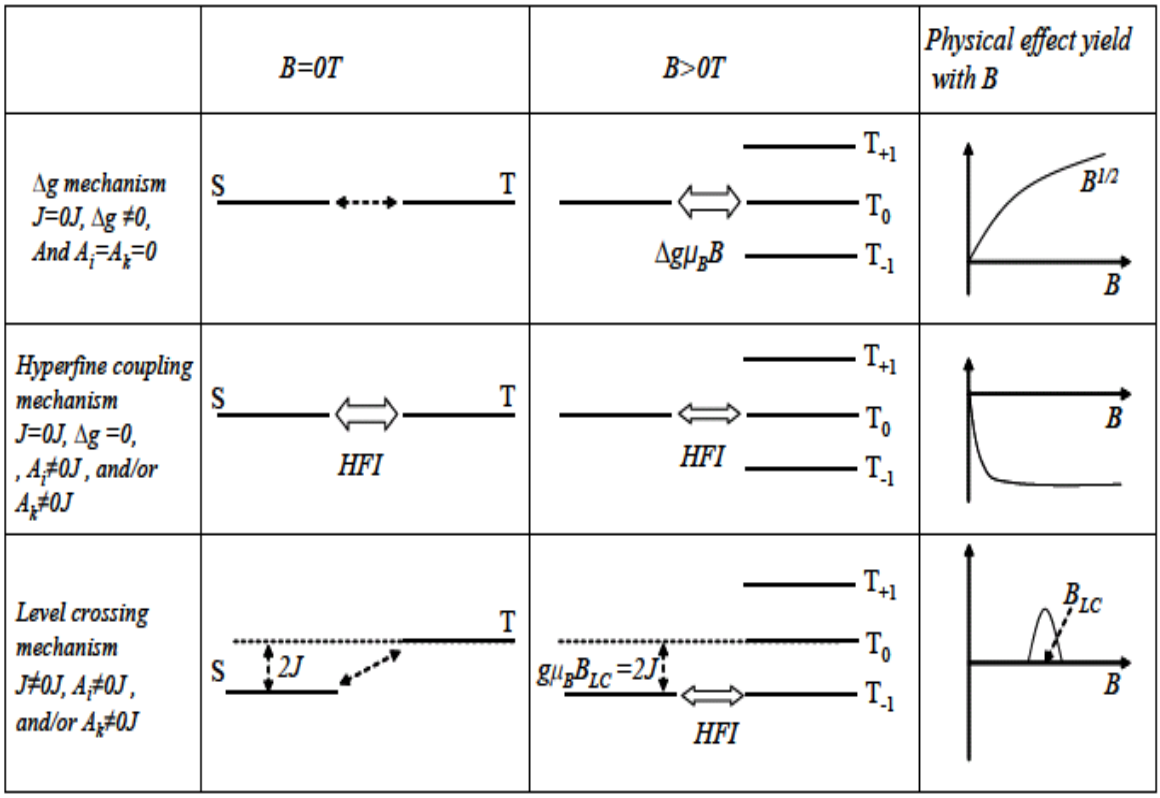

Figure 1.8. Summary of magnetic field effects on the singlet-triplet conversion of polaron pairs and physical effect yield with B.

channel of singlet excitons' collisions with triplet excitons (TE), of which density varies with *B*, MPL (B) can be explained by the magnetic field dependent TE density.

1.7 Organic Photovoltaics

Tang was the first to implement a bilayer heterojunction solar cell device [34] in 1986 and achieved 1% power conversion efficiency (PCE). After this discovery, intensive research on solar cells comprising organic semiconductors has been carried out and 10.6% PCE [35] including tandem structure is the record value to the date.

The working principle of bulk heterojunction (the active layer consists of donor and acceptor) organic photovoltaics (OPVs) starts with photoexcitation of donor material. The photons that are absorbed in the active layer excite the polymer and form a coulombically bound electron-hole pair, known as an exciton. Dissociation of the photogenerated excitons is facilitated by the energy level difference between the LUMO of the donor and acceptor, as well as between their HOMO levels. The exciton diffuses to the donor-acceptor (D-A) interface within few picoseconds [36, 37], and forms a charge transfer exciton (CT) upon arrival [38, 39]. Initially, the CT excitons separate into more loosely-bound polaron pairs (PPs), the intermediate species that exist at the donor/acceptor interface. Subsequently, PPs separate into “free” electrons and holes that are available for transport. In the blend, the donor acts as electron donor and hole transporter, whereas the fullerene derivative is an electron acceptor and transporter; thus, the photogenerated electrons and holes can be readily collected at the anode and cathode, respectively. The typical device structure of bulk heterojunction (BHJ) OPVs is shown in Figure 1.9. The charge photogeneration process upon photoexcitation in BHJ solar cell devices is shown in Figure 1.10.

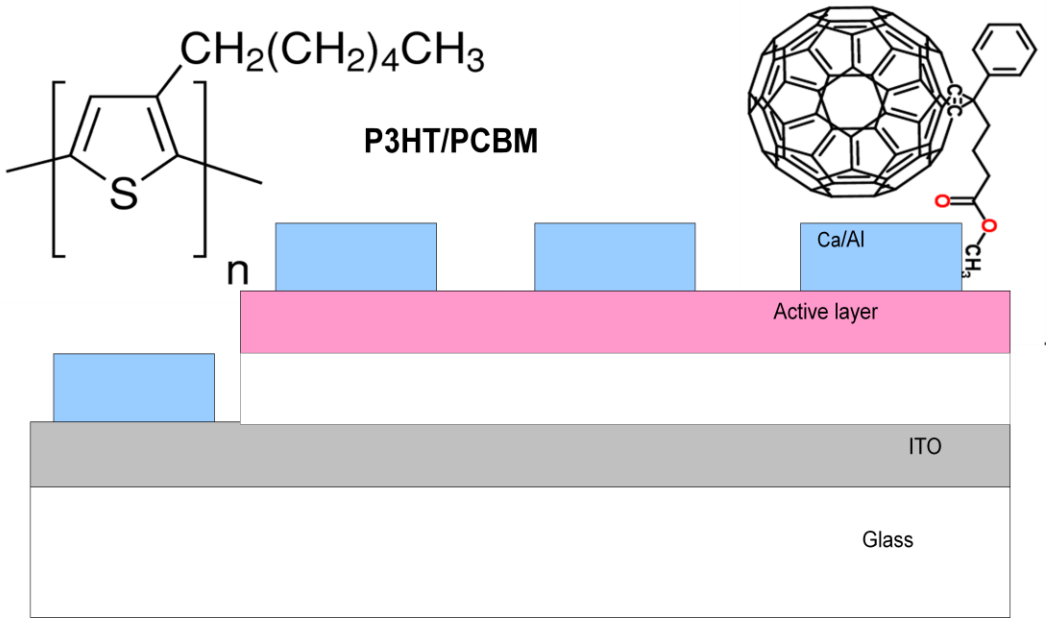

Figure 1.9. Typical device structure of bulk-heterojunction OPV solar cell.

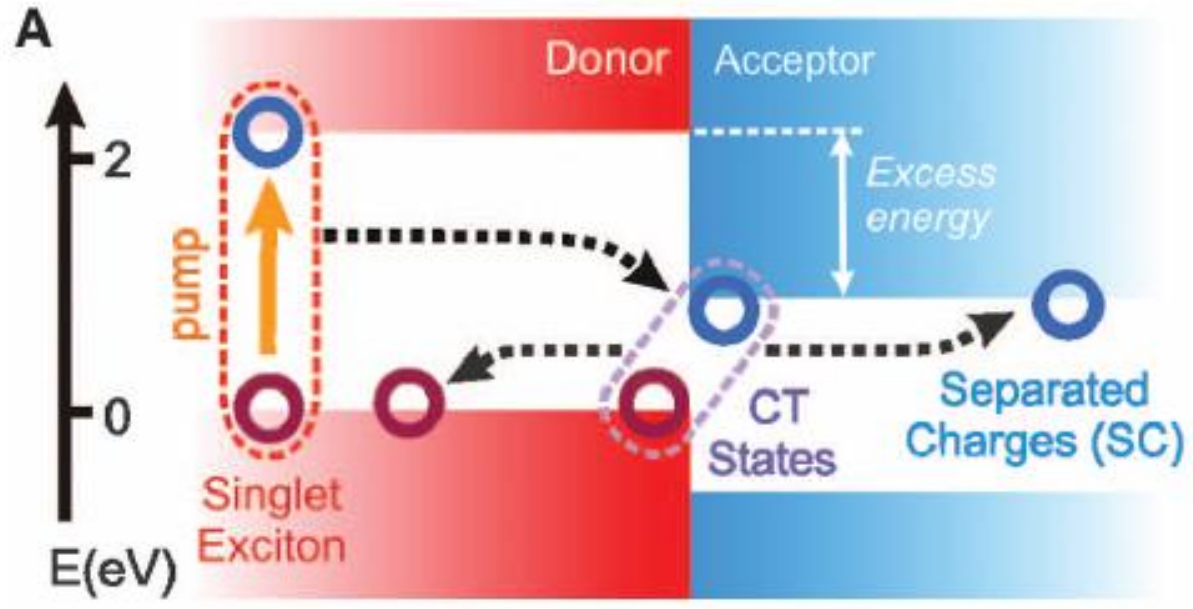

Figure 1.10. Energy level diagram of donor and acceptor in typical OPV, and the related electronic processes. The figure is adapted from Ref [37].

CHAPTER 2

EXPERIMENTAL TECHNIQUES

In this chapter, we describe most of the experimental techniques used in this PhD thesis. In particular, we focus on the fabrication of organic light emitting diodes (OLEDs) and bulk heterojunction organic photovoltaic (OPV) devices; and experiments performed using the magnetic field effect (MFE) in OLEDs, organic films, and OPV devices.

2.1 Materials

The materials used in this thesis are either polymers or small molecules. Polymers are chain-like macromolecules with high molecular weight (>1000g/mol). They are soluble in organic solvents and can be deposited easily. Small molecules have molecular weight less than 1000g/mol and are usually deposited using thermal evaporator in vacuum. Isotopes of Poly (dioctyloxy) phenylenevinylene (DOO-PPV), Poly (2-methoxy-5-(2-ethylhexyl-oxy)-1,4-phenylene-vinylene)) (MEH-PPV), Rubrene, Polyfluorene (PFO), Regio-Regular –Poly-(3-hexylthiophene) (RR P3HT), Regio-Random–Poly-(3-hexylthiophene) (RRa P3HT), Poly-thienothiophene benzodithiophene 7 (PTB7), C_{60} molecule, [6,6]-Phenyl C_{61} butyric acid methyl ester ($PC_{61}BM$), and [6,6]-Phenyl C_{71} butyric acid methyl ester ($PC_{71}BM$) are materials used in this thesis, which are tabulated

in Figures 2.1(a)- (l) along with their chemical structures. Isotopes of DOO-PPV were synthesized by chemist Leonard Wojcik in our lab. RR P3HT was supplied by Plextronics; it has excellent properties compared to other commercial suppliers. MEH-PPV, PFO, C_{60}, $PC_{61}BM$, and $PC_{71}BM$ were purchased from American Dye Source (ADS). RRa P3HT and Rubrene were from Sigma Aldrich and PTB7 was from 1-Material. The synthetic reagents and solvents were procured from Aldrich Chemical as reagent grade and used as received. To prevent oxidation and other possible material contaminations, all handling processes were done in an inert nitrogen (N_2) atmosphere inside a glove box with oxygen level less than 0.7 ppm.

2.2 Organic Light Emitting Diodes Fabrication

The typical OLED device that we have investigated consists of a thin film of organic layer sandwiched between two nonmagnetic electrodes. A glass substrate partially coated with Indium Tin Oxide (ITO) with resistivity 8-12 Ω/cm was purchased from *Delta Technologies*. ITO is used as an anode to inject holes into the organic layer, because of its high work function (4.8-5.1 eV). To detect the light coming out of an OLED, a transparent electrode must be also used. As ITO has high transparency (>85%), it is suitable to be used as a transparent electrode.

Patterning of ITO was done using either photolithography or a tape as an ‘etch mask’. For regular size (1 mm x1 mm) devices, the portion of the substrate to be used as bottom electrode was covered with ‘nail polish’ and the rest was covered with a tape. The substrate was then immersed into a solution of hydrochloric acid (80% by volume) and water (20% by volume) for 10 minutes, for etching the exposed portion of the ITO. After

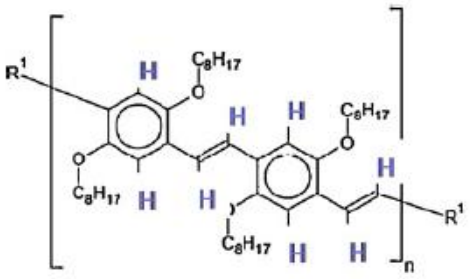

(a) Protonated Poly(dioctyloxy) phenylenevinylene (H-DOO-PPV)

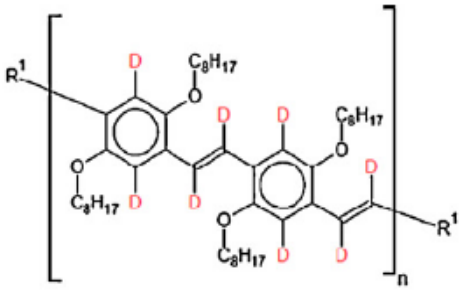

(b) Deuterated Poly(dioctyloxy) phenylenevinylene (D-DOO-PPV)

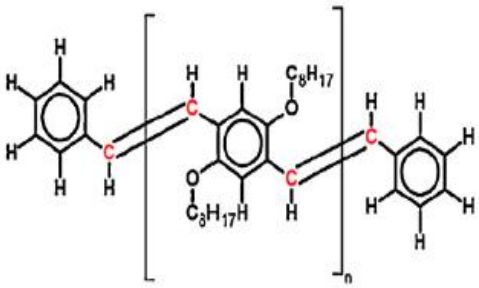

(c) C13-rich Poly(dioctyloxy) phenylenevinylene (C13-DOO-PPV)

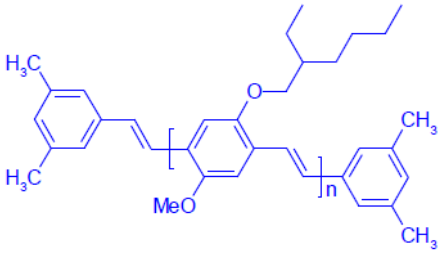

(d) Poly[2-methoxy-5-(2-ethylhexyl-oxy)- 1,4-phenylene-vinylene]] (MEH-PPV)

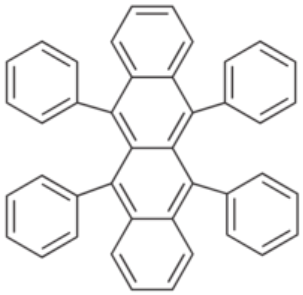

(e) Rubrene

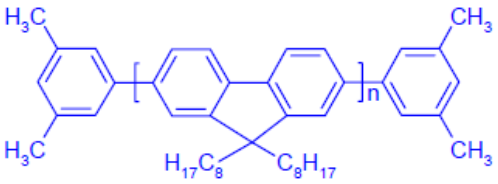

(f) Polyfluorene (PFO)

Figure 2.1. Chemical structures of (a) H-DOO-PPV, (b) D-DOO-PPV, (c) C-13-DOO-PPV, (d) Rubrene, (e) PFO, (f) MEHPPV, (g) RR P3HT, (h) RRa P3HT, (i) PTB7, (j) C_{60} , (k) $PC_{61}BM$, and (l) $PC_{71}BM$.

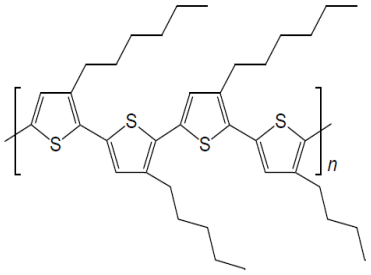

(g) Regio-Regular –Poly-(3-hexylthiophene) RR P3HT

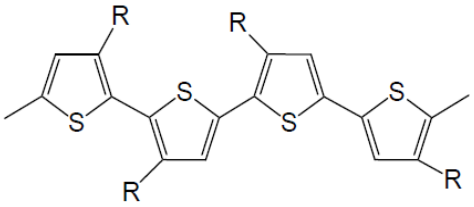

(h) Regio-Random-Poly-(3-hexylthiophene) RRa P3HT

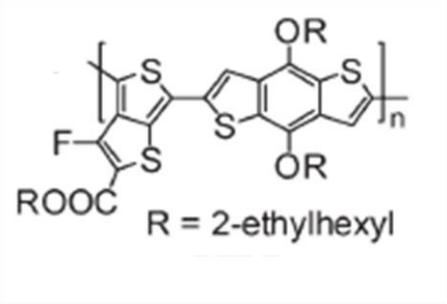

(i) Poly-thienothiophene-benzodithiophene 7 (PTB7)

(j) C_{60} molecule

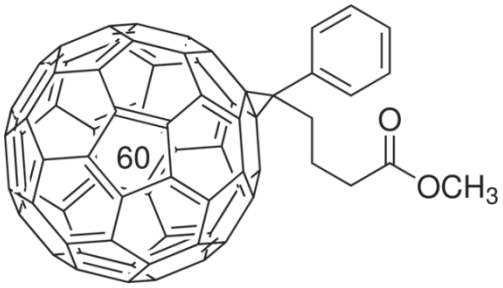

(k) [6,6]-Phenyl C61 butyric acid methyl ester ($PC_{61}BM$)

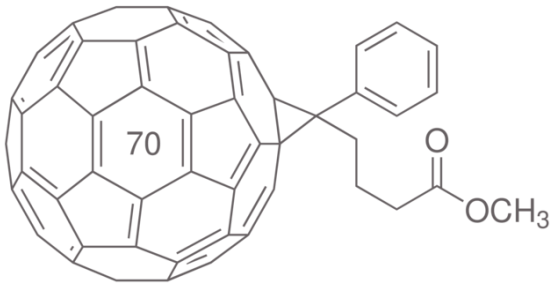

(l) [6,6]-Phenyl C71 butyric acid methyl ester($PC_{71}BM$)

Figure 2.1. Continued.

etching, the 'nail polish' was cleaned with acetone, and the patterned ITO was 'diced' into 12.5 x12.5 mm^2, as shown in Figure 2.2(a)**.** For fabricating miniature devices, the ITO substrate was cleaned and photoresist was applied by spin casting. The photoresist was then dried by heating the substrate at 120 ^oC for 2 minutes. After baking, the sustrate was exposed to intense UV and developed by AZ 352 developer for the desired pattern. Finally, the substrate was etched using dilute hydrochloric acid, and the residual photoresist was removed using acetone.

One percent micro soap cleaning solution, acetone, methanol, and propanol were consecutively used in ultrasonic hot baths for 15 minutes each to remove occasional organic and inorganic dirt from the substrate. Compressed nitrogen gas was blown to dry the substrate in clean room. Subsequently, oxygen plasma cleaning of the substrate was performed to remove any remaining dirt and organic solvents.

Following the above-mentioned cleaning procedures, a thin layer of PEDOT:PSS (70:30) was spin-coated at 5000 rpm for 40 sec. The thickness of this layer was about 50 nm, as indicated by a 'thickness profilometer'. This layer acts as the hole transporter into the organic layer. The spin coated substrate was then transferred into the glove box. In order to remove water molecules, the substrate was heated at 110 ^oC for 30 minutes inside the glove box.

A solution of luminescent π- conjugated polymer was made by dissolving the appropriate chemical powder with suitable organic solvent. Based on the material used for the organic layer, different solvents were used such as toluene, chloroform, chlorobenzene, and 1, 2-dichlorobenzene. The thin organic layer (80-150 nm) was made by spin casting the solution onto the substrate. For small molecules such as Alq_3, C_{60} etc.,

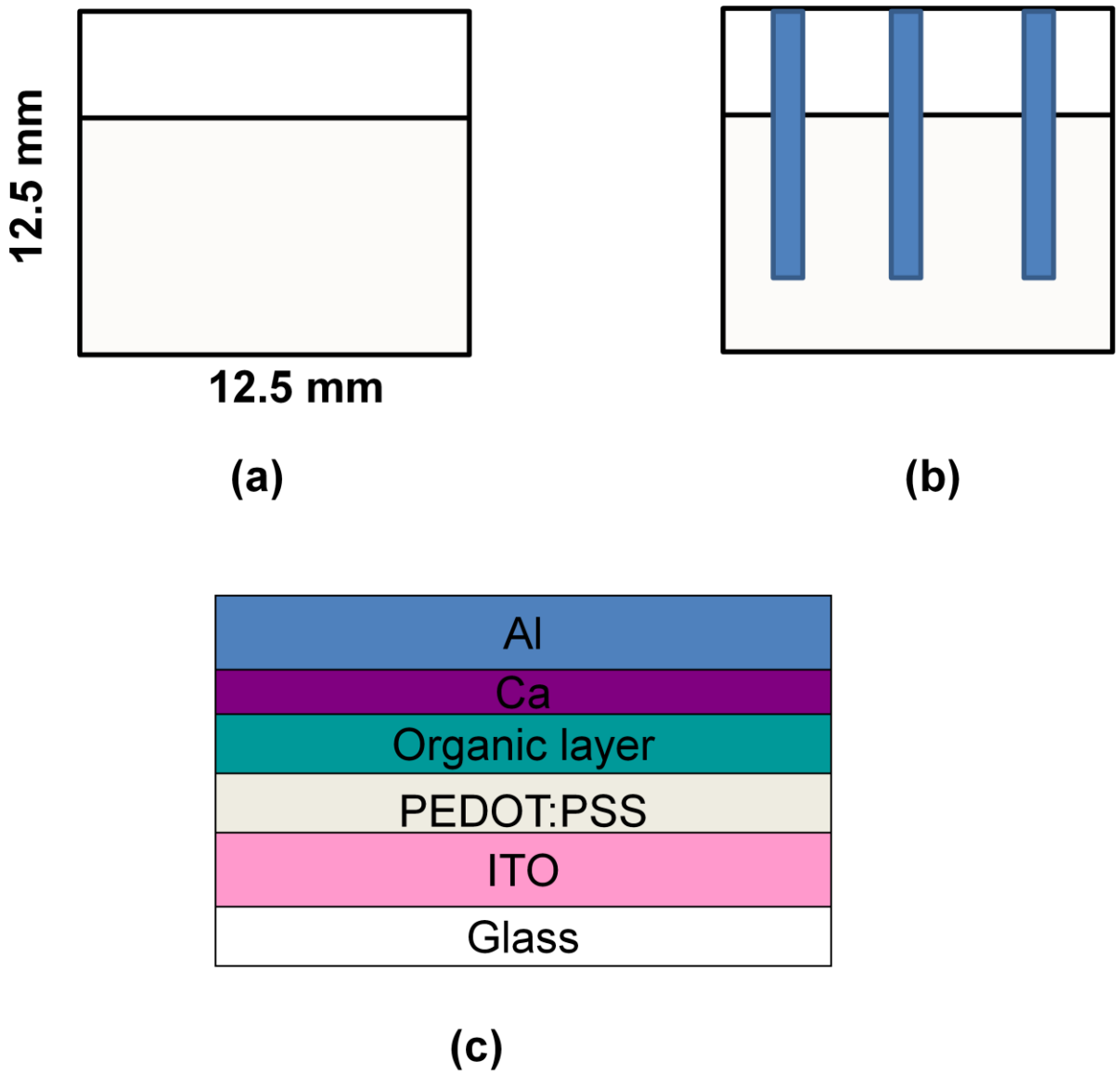

Figure 2.2. ITO pattern on the substrate after etching (a). Top view of completed OLED device (b). The typical OLED device structure (c).

the powder was thermally evaporated to produce thin films using a slow evaporation rate.

To deposit the top electrode, the quoted substrate was put in a thermal evaporator. The evaporator was then pumped down to 2 x 10^{-6} torr before evaporation. Low work function metal calcium was evaporated at the rate of 2-3 A^{o}/s on top of the organic layer, which served as an electron transporter into the organic layer. 100 nm of aluminum was then deposited on top of the calcium layer to serve as a 'capping layer' for protection against oxidation. The film thickness of deposited metals was measured using an Inficon XTM quartz crystal deposition monitor mounted at the same height as the samples in the evaporation chamber. The top view of a typical completed device is shown in Figure 2.2(b). Three kinds of organic diodes were fabricated with the configuration ITO/PEDOT/organic layer/Ca/Al, ITO/PEDOT/ organic layer /Au, and Glass/Al/LiF/organic layer/Ca/Al for bipolar (OLED), for hole unipolar and electron unipolar diodes, respectively. The typical device structure of OLED is shown in Figure 2.2(c).

In order to reduce the penetration of oxygen and water to the device, the completed device was encapsulated using microscope cover glass and UV curable glue purchased from Norland, which was exposed to UV light for 30 seconds.

2.3 Organic Light Emitting Diodes Characterization

To characterize the performance of the fabricated OLEDs, the following measurements were performed on the completed device.

2.3.1 Current-Voltage and Electroluminescence-Voltage Characteristics

The completed device was mounted on the sample holder and the electrical connections for the measurements were done. The device was then placed in a closed cycle Helium cryostat. I-V measurement was performed on the device using Keithley 236 apparatus. A silicon photo-detector connected with the oriel preamplifier and Keithley 2400 system was used to measure the electroluminescence from the bipolar devices. Figure 2.3 shows typical current-voltage (I-V) and electroluminescence-voltage (EL-V) characteristics of a MEH-PPV OLED (ITO/PEDOT/MEH-PPV/Ca/Al).

The charge transport in the organic layer under electric field is mainly due to hopping, which is limited by shallow and deep traps, recombination, morphology, temperature, etc. When the applied bias voltage is smaller than the 'built-in voltage', V_0, then the current flow in the device is linear with the voltage, which may be due to some leakage current superimposed on the injection current. Upon increasing the bias voltage, injected carriers form a space charge layer near the injecting metal/organic interface due to the low carrier mobility. The current flow is then governed by space charge limited current (SCLC) described by Mott-Gurney law [40] for current density, i.e.,

$$J = \frac{9\varepsilon\mu V^2}{8L^3} \tag{2.1}$$

where ε is the electric permittivity, μ is the carrier mobility, and L is the organic layer thickness.

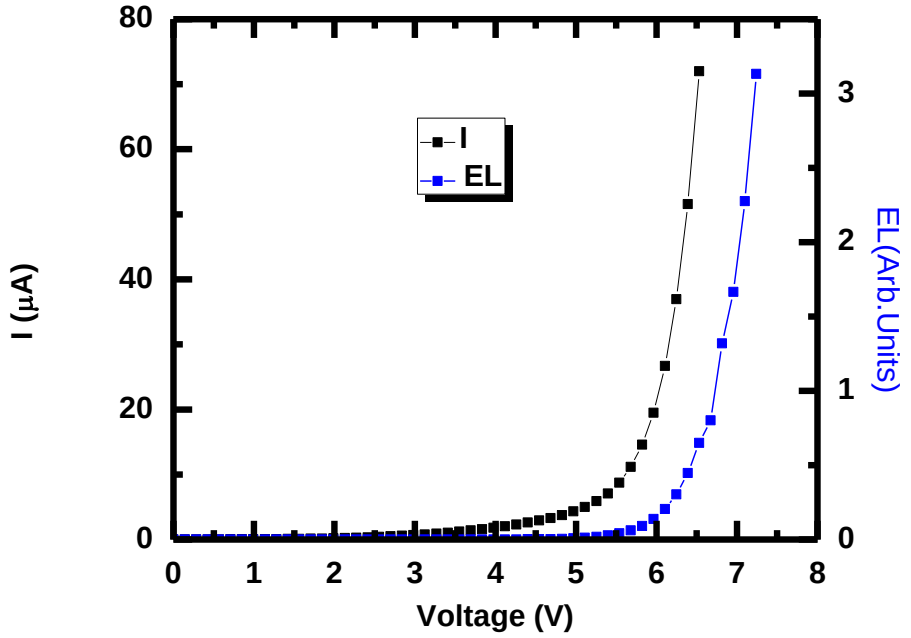

Figure 2.3. Typical I-V and EL-V characteristics of OLED device based on MEHPPV as an active layer at 10 K.

In the bipolar injection regime, needed for electroluminescence emission, the relation of current density is modified as [41],

$$J = \frac{9\varepsilon}{8}\sqrt{\frac{2\pi\mu_e\mu_h(\mu_e+\mu_h)}{\mu_r}}\frac{V^2}{L^3} \qquad (2.2)$$

where $\mu_r = r\,(\mu_e+\mu_h)$ is the recombination mobility, and r<<1 is a constant.

2.3.2. Magnetoconductance and Magneto-electroluminescence

Magnetoconductance (MC) and magneto-electroluminescence (MEL) of OLED devices is typically measured by sweeping the magnetic field at a constant bias voltage

using Keithley 236 apparatus. MC or MEL is defined as the fractional change in the field induced current or electroluminescence, respectively. For performing such measurement, the devices were mounted onto a cryostat placed in between the poles of an electromagnet with the magnetic field perpendicular to the current flow through the device. Magnetic field up to 300 mT was produced using an electromagnet, and measured using the Hall probe Gaussmeter. A temperature controller unit was connected to the cryostat for measuring the MC and MEL temperature dependences. The schematic of the experimental set-up for the measuring organic magnetic field effect (MFE) is shown in Figure 2.4.

The change in current at a constant bias voltage, V for different magnetic field, B was measured using Keithley 236 apparatus. Magnetic field-induced fractional change in current or electroluminescence, $\Delta X/X$ (dubbed MX) is defined by

$$\frac{\Delta X}{X} = \frac{X(B) - X(B=0)}{X(B=0)} \tag{2.3}$$

which is positive or negative depending on the value of X(B) compared to X(0), where X=I or EL. Figure 2.5 shows typical magnetoconductance, MC, and magneto-electroluminescence, MEL, responses of an OLED device.

To characterize the magnetic field dependence of current flow through the device or electroluminescence output, either a Lorentzian,

$$MX(B) = MX_{\infty} \frac{B^2}{B^2 + B_0^{\,2}} \tag{2.4}$$

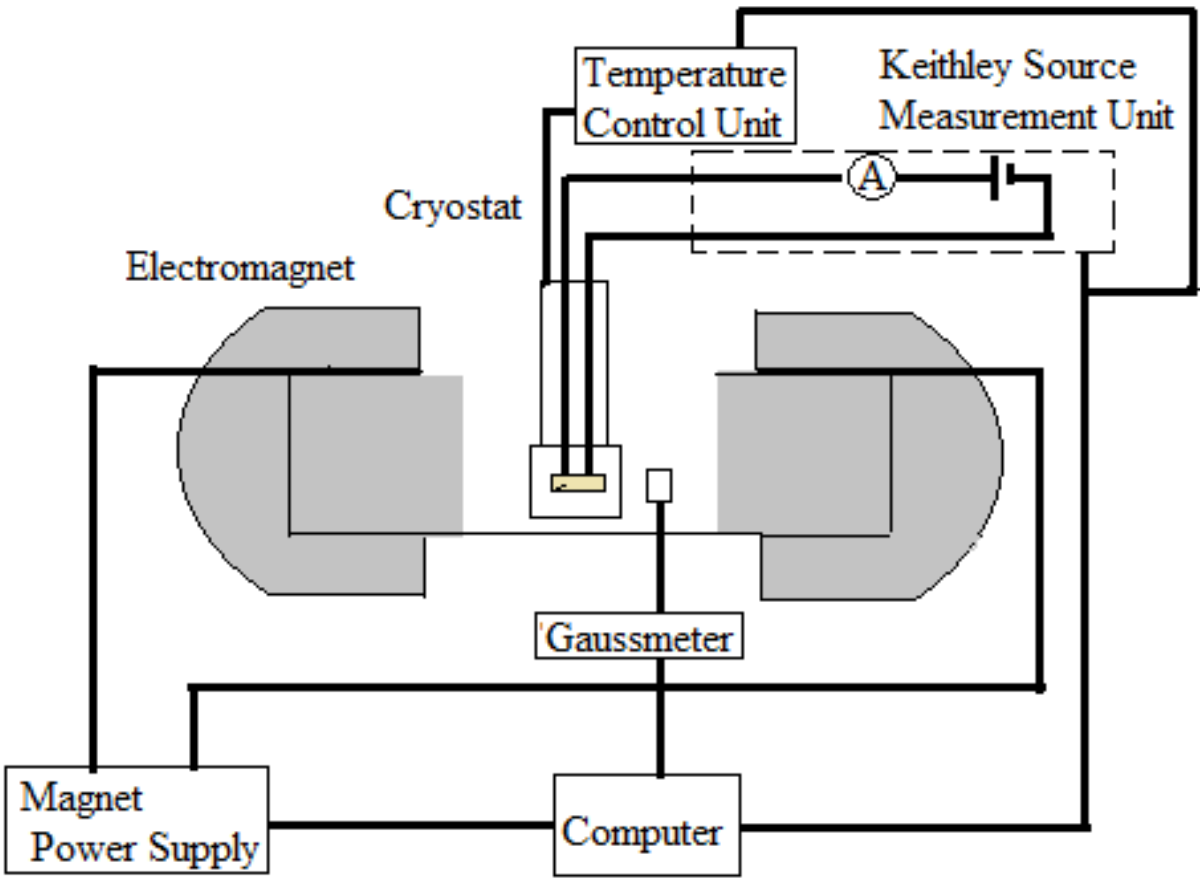

Figure 2.4. The experimental set-up for measuring the organic magnetic field effect in films and devices

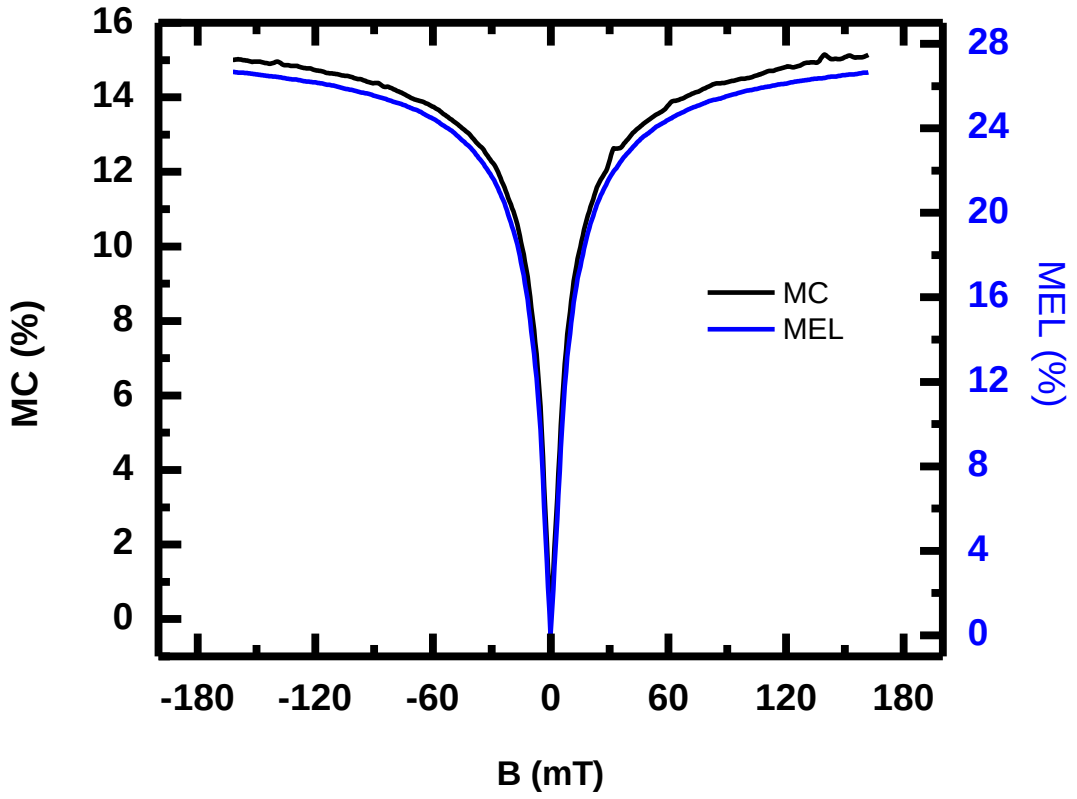

Figure 2.5. Typical MC and MEL responses of an OLED based on MEHPPV as the active organic interlayer, measured at 10 K.

where B_0 is half width at half maximum and MX_∞ is MX at infinite magnetic field, or the non-Lorentzian line shape

$$MX(B) = MX_\infty \frac{B^2}{(|B|+B_0)^2} \tag{2.5}$$

where B_0 is half width at quarter maximum were reported for most of the polymers and small molecules used here. The parameter B_0 is about 3-10 mT for most of the investigated polymers [19, 22, 25, 33, 42]. It was shown in the literature that this parameter is related with a process that involves a spin flip mechanism caused by the hyperfine interaction.

2.4 Organic Photovoltaic Device Fabrication

The fabrication procedure of an organic photovoltaic (OPV) cell is roughly the same as fabrication of an OLED device. The only difference is the active material. The active material used in an OPV cell is a suitable blend of organic donor and acceptor. Depending upon the donor/ accepter system, either the spin casted layer was annealed, or a few percentages of additives were added onto a solution of the blend in order to improve the morphology and hence to facilitate the nanoscale phase separation between the polymer donors and fullerene aggregates acceptors.

2.5 Organic Photovoltaic Device Characterization

2.5.1 Current-Voltage (I-V) Characteristics

To characterize the power conversion efficiency (PCE) of OPV solar cells, the OPV devices were illuminated under a standard AM 1.5 condition shown in Figure 2.6. This illumination condition was generated in our lab using a xenon lamp having a broad spectral range (300-1000 nm). After passing through the AM 1.5 filter, the light has a spectrum close to a standard AM 1.5 spectrum. Using a NREL-certified Si photovoltaic cell, the xenon lamp output was calibrated to get a light intensity of 100 mW/cm^2, appropriate to the sun illumination intensity on the Earth at sea level.

The experimental set-up for the current-voltage (I-V) characteristics of OPV devices is shown in Figure 2.7. The typical I-V characteristics of a PTB7/PC70BM with 3 wt% of 1,8-diiodooctane (dio) device measured using the Keithley 236 apparatus is shown in Figure 2.8. Three parameters are used to characterize the PCE of OPV devices.

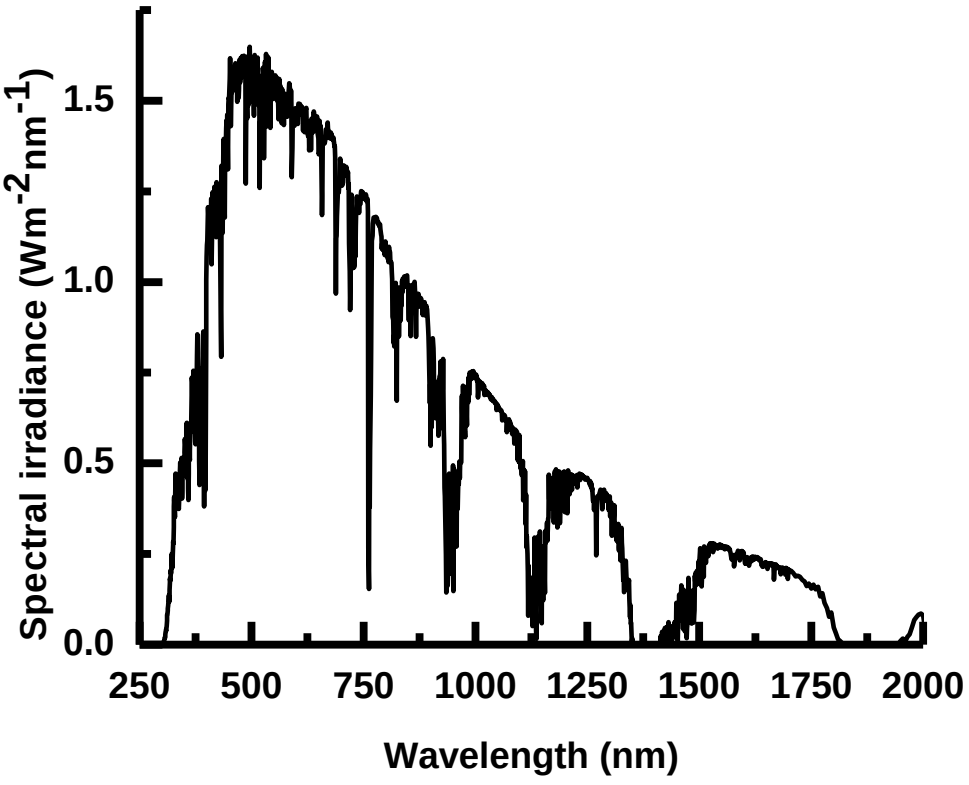

Figure 2.6. Standard 'AM1.5 spectrum', under which the integrated illumination intensity is 100 mW/cm^2

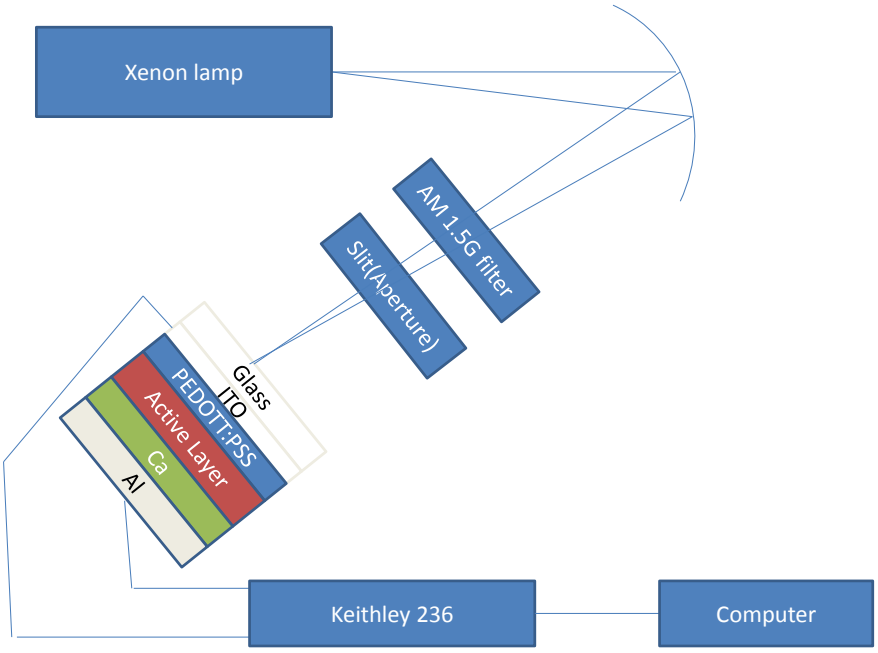

Figure 2.7. The experimental set-up for measuring the I-V response of an OPV cell.

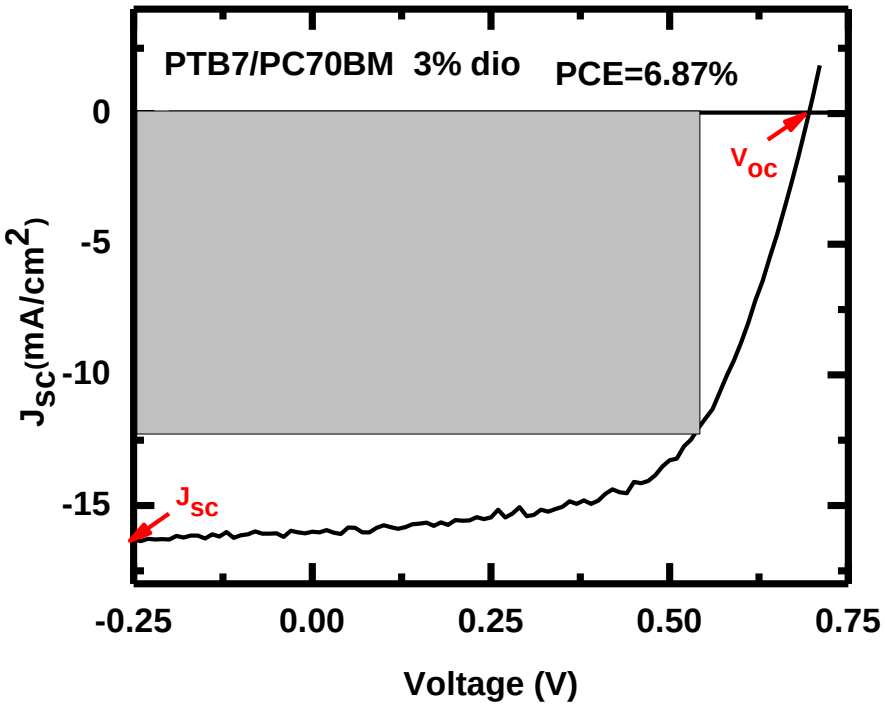

Figure 2.8. Typical I-V characteristics of a PTB7/PC70BM OPV cell with 3 wt% of 1,8-diiodooctane, under 'AM 1.5' sun-like illumination.

These are: short circuit current density (J_{sc}), open circuit voltage (V_{oc}), and fill factor (FF), which is defined by relation,

$$FF = \frac{P_{\max}}{J_{sc}V_{oc}} \tag{2.6}$$

where P_{max} is the largest power output from the device, as shown in Figure 2.6 by the shaded region. The power conversion efficiency (η) of OPV cell is defined as,

$$\eta = FF\,\frac{J_{sc}V_{oc}}{P_{in}} \tag{2.7}$$

where P_{in} is the optical irradiance of incident light from the sun (100 mW/cm^2).

2.5.2. Magneto-photocurrent (MPC) Measurement

In order to measure the magnetic field effect on photocurrent (PC) of OPV devices, the fabricated OPV device was transferred into the cryostat placed in between the pole pieces of an electromagnet. The experimental set-up is the same as that for measuring MC in OLEDs, except that the OPV device was illuminated either with a tungsten lamp or with a laser of suitable wavelength (depending upon the absorption spectrum of polymer). By setting the bias voltage to zero (short circuit condition) using the Keithley 236 apparatus, the field-induced fractional change in photocurrent was measured when sweeping the magnetic field. MPC is defined by the relation:

$$MPC(B) = \frac{PC(B)}{PC(0)} - 1 \tag{2.8}$$

Typical MPC(B) response for an OPV cell based on PTB7/$PC_{70}BM$ with 3 wt% of 1,8-diiodooctane (dio) molecules is shown in Figure 2.9. The MPC response shows the broad nonsaturating response with magnetic field, typical of Δg spin mixing mechanism (see below).

2.6 Material Characterization

2.6.1 Linear Absorption Measurement

The absorption of a medium is quantified by measuring the optical density (OD), which is also called absorbance. In general, the absorption spectrum gives general information about the band gap (material compound) and the electronic excited states of the material of interest. When the π-conjugated polymer absorbs light, it promotes an electron from the ground state S_0 to the excited state S_1 that is dipolar-coupled with the ground state. The transitions from the ground state S_0 to the higher singlet states S_n occur depending on the oscillator strength of particular transition, appropriate parity, and spin angular momentum.

A Cary-17 spectrophotometer from Olis. Co. was used for the absorption measurement in the spectral range 300-2400 nm, which was carried out at ambient conditions. In order to remove the substrate effect and system response, background transmittance T_0 of a glass substrate was measured first as a function of wavelength. The sample was then deposited on the glass substrate and the transmittance through the

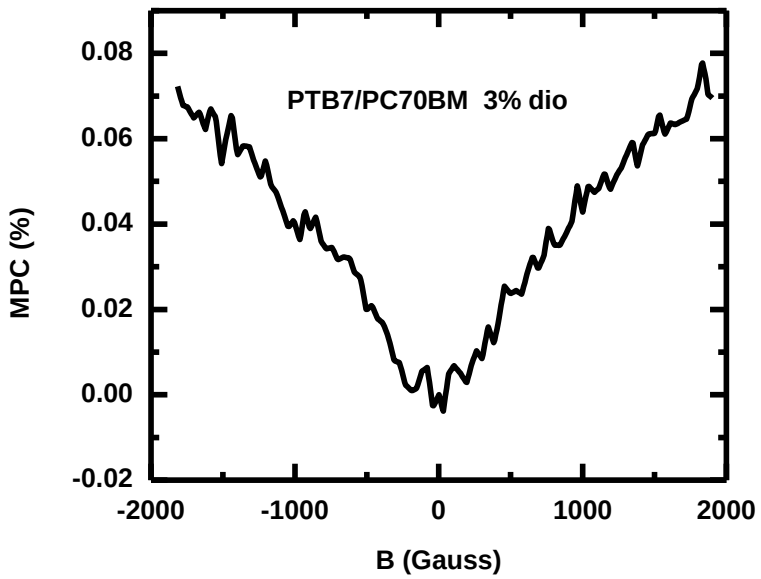

Figure 2.9. MPC(B) response of a PTB7/PC70BM-based OPV cell with 3 wt% of 1,8-diiodooctane, measured at room temperature.

sample, T_1, was measured again. The reflection and scattering from the sample was neglected, assuming their negligible values. The absorbance 'A' was then calculated using the relation $A=\log (T_0/T_1)$. The absorbance is related to the film's thickness'd' and the absorption coefficient (α) according to the Beer-Lambert law $A(\lambda)=OD=\alpha d$. So, the absorption which is measured in the unit of OD is given by the relation,

$$T_1=T_0 \exp(-\alpha d) \qquad (2.9)$$

A typical absorbance spectrum of MEHPPV film is shown in Figure 2.10.

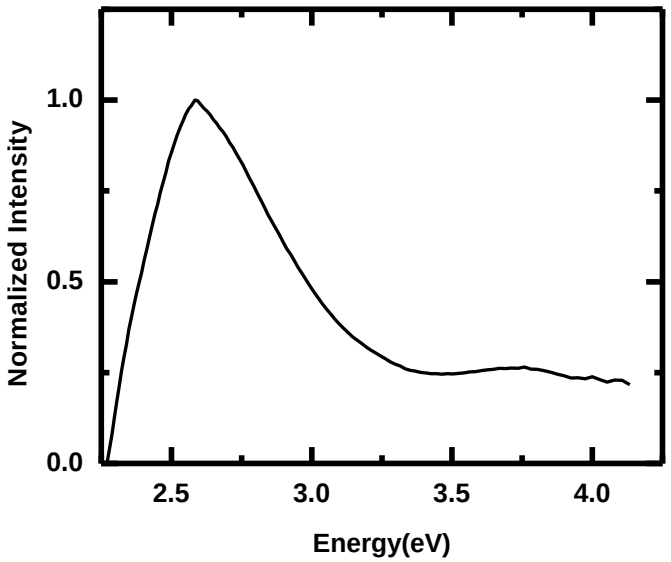

Figure 2.10. Typical optical density spectrum of MEHPPV film.

2.6.2 Photoinduced Absorption Measurement

Continuous wave (CW) photoinduced absorption (PA) studies the change in absorption caused by long-lived photoexcitation species such as triplet excitons and polarons in the film. The difference in the transmission (ΔT) when the sample is illuminated with both the pump and the probe (T_L) and when the sample is illuminated only with the probe (T_D), i.e., $\Delta T=T_L-T_D$ gives the photoinduced absorption of the photoexcited species.

Assuming the change in transmission is associated with a light-induced change in absorption coefficient ($\Delta\alpha$), we have

$$T_L = T_D e^{-\Delta\alpha d} \tag{2.10}$$

$$\frac{T_D + \Delta T}{T_D} = 1 + \frac{\Delta T}{T_D} = e^{-\Delta\alpha d} \tag{2.11}$$

$$\Delta\alpha d = -\ln(1 + \frac{\Delta T}{T_D}) \tag{2.12}$$

When the difference in the transmission is much smaller than the transmission, i.e., $\Delta T << T_D$,

$$\Delta\alpha d \approx -\frac{\Delta T}{T_D} \tag{2.13}$$

We can have two types of signals depending upon the sign of $\Delta\alpha$. If $\Delta\alpha<0$, then it is photoinduced absorption (PA), which is associated with the absorption due to creation of new states; if $\Delta\alpha>0$, it is photobleaching (PB), which is caused when the lower of the two energy states involved in the optical transition (usually the ground state) is depleted by another process.

The experimental set-up for the PA measurement is shown in Figure 2.11. The sample (thin film) was transferred into the He cryostat, and cooled down to cryogenic temperatures using a close-cycle refrigerator. Two light beams were used for the PA measurement. A cw Ar+ laser was used as a pump to excite the material (i.e., to promote electron from ground state to excited state) and another cw beam from an incandescent

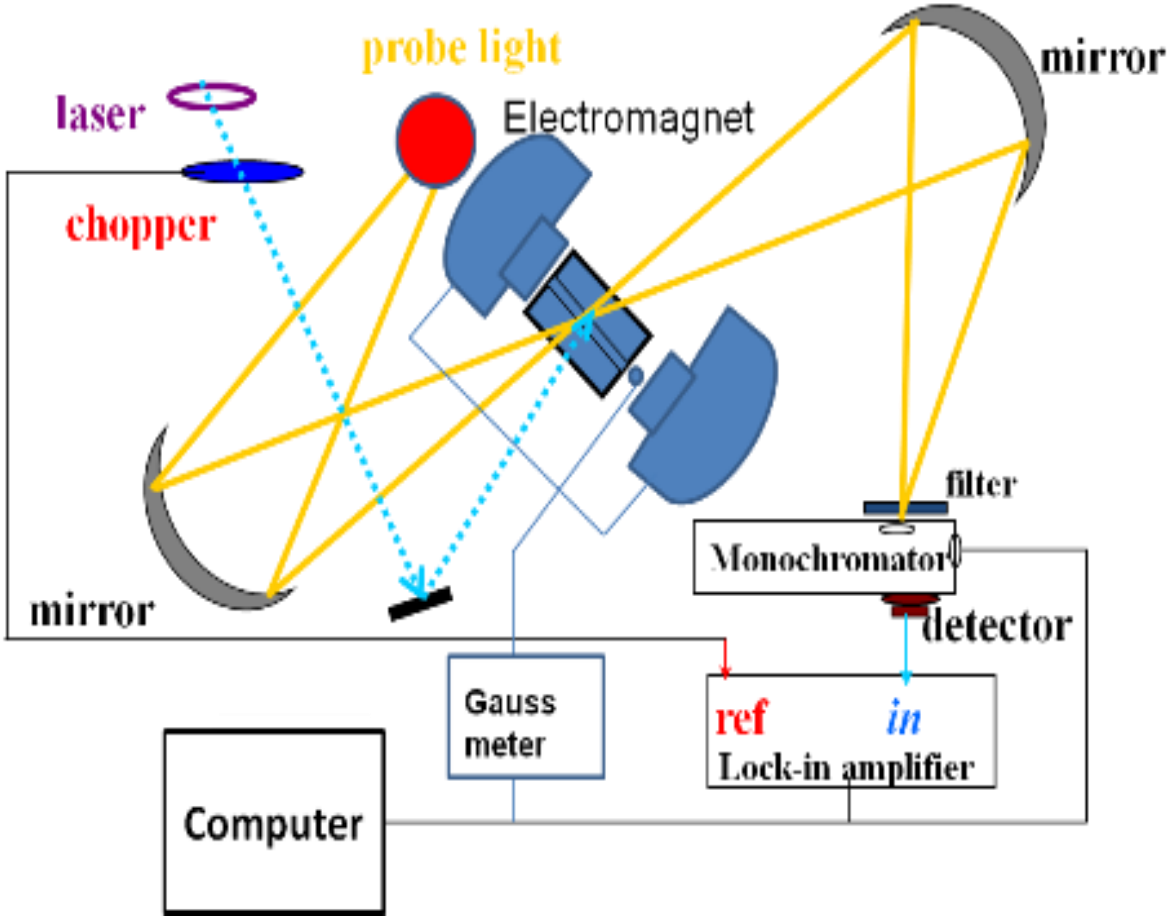

Figure 2.11. The experimental set-up for measuring the PA spectrum.

halogen tungsten lamp or xenon lamp to cover wavelength range from 550 nm to 4.2 μm was used to probe the PA of long-lived photoexcitations. The transmitted light was spectrally resolved by an Acton 300 monochromator and monitored by Si, Ge, or InSb detectors with corresponding amplifier, long pass filter, and grating set, depending on the wavelength probed. Si 10 D photodiode, Ge, and InSb detectors were used to cover the wavelength 550 nm to 1.05 μm, 800 nm to 1.6μm, and 1 μm to 4.2 μm, respectively. The signal was converted from current to voltage and amplified using a preamplifier. The

amplified signal was then fed into a lock-in amplifier SR 830 together with the phase reference of a modulated laser beam which is usually modulated with a frequency that corresponds to the life time of photoexcitations, which was usually set at 300 Hz.

The cw photo-modulation (PM) spectrum measured in UV irradiated MEH-PPV film using above gap (2.5 eV) pump excitation is shown in Figure 2.12. The PM spectrum consists of two broad PA bands; one centered at ~0.4 eV, which is assigned to the lower polaron transition (marked 'P_1'); and the other is asymmetric with a peak at ~1.4 eV (marked 'T+P_2'), which is composed of the polaron P_2 transition centered at ~1.55 eV, and the remnant of the triplet exciton transition.

2.6.3 Magneto-photoinduced Absorption Measurement

The negative fractional change in transmission, also called PA, is given by the relation:

$$PA(E)=(-\Delta T/T)=\Delta\alpha d=N_{SS}\,\sigma(E), \qquad (2.14)$$

where N_{SS} is the species steady state density, $\sigma(E)$ is the photoexcitation optical cross-section, and E is the probe beam photon energy. Therefore, in a magnetic field, B, $PA_X(B)$ is determined by the density $N_{SS}(B)$; which, in turn, is controlled by thephotoexcitationspecies (polaron pair (PP), triplet exciton (TE), or pair of triplet excitons) decay rate coefficient, $\kappa(B)$ [$N_{SS=}G/\kappa$] where G is the generation rate, and X stands for species such as PP, TE, and pairs of TEs. The X species has an excited state transition $X_0 \rightarrow X_1$ (PA_X), which is activated by a weak probe beam. For $B \neq 0$, the X_0

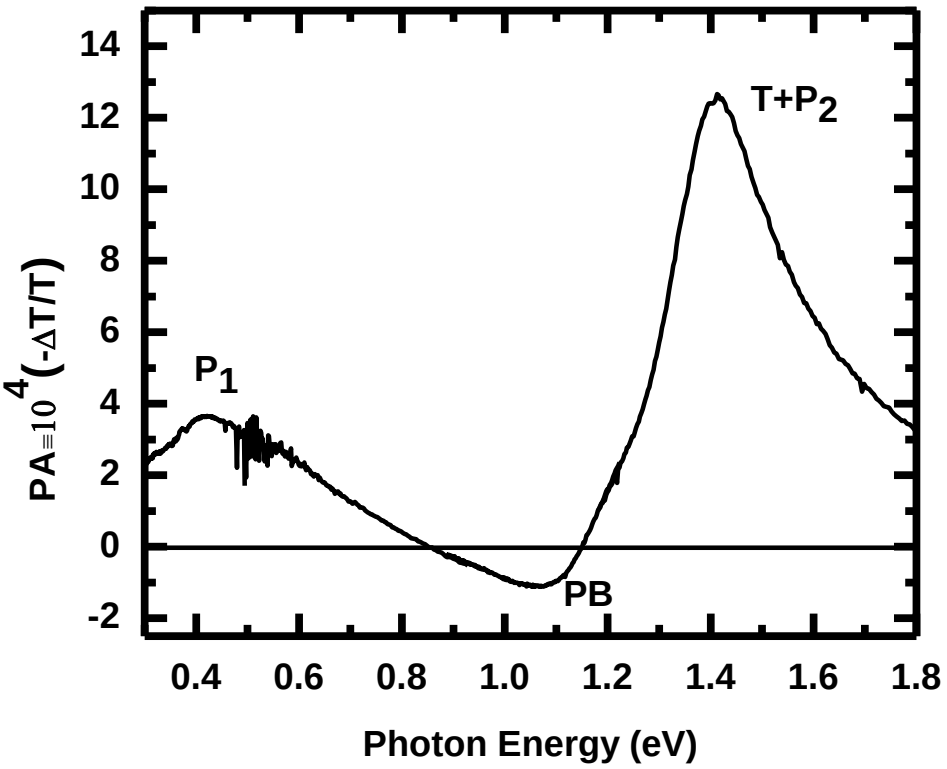

Figure 2.12. The photoinduced absorption spectrum of an irradiated MEH-PPV film. The PA bands P_1 and $T+P_2$ are denoted.

level splits according to the relevant spin multiplicity, L (L=3, 4 and 9, respectively for the S=1 TE; PP composed of two S=½ polarons; and a pair of TEs). Consequently, through specific spin-mixing processes, the spin content of each sublevel, its decay rate κ, and thus N_{SS} and consequently, PA all become B-dependent, i.e.,

$$MPA_X(B) \equiv [PA_X(B)-PA_X(0)]/PA_X(0) \qquad (2.15)$$

In order to measure the magneto-photoinduced absorption (MPA), an electromagnet producing the magnetic field up to 200 mT was placed across the cryostat.

The PA spectrum with and without the magnetic field is measured to obtain the MPA spectrum. To obtain the desired magnetic field response of the PA spectrum in films, the monochromator was fixed at the desired wavelength where either the triplet exciton or the polaron band was assigned, and PA(E) spectrum was measured while sweeping B. Figure 2.13 shows the typical MPA(B) response of an irradiated MEH-PPV film. The MPA response is similar to the MC and MEL response of OLED made from the same active layer (MEH-PPV), which indicates that they share a common origin.

2.6.4. Photoluminscence and Magneto-photoluminscence Measurements

When the polymer film is excited by a continuous wave (cw) laser beam with above-gap photon energy, it generates steady state singlet excitons (SE; $S_0 \rightarrow S_1$). The SE may either recombine radiatively ($S_1 \rightarrow S_0$), giving photoluminscence (PL) emission, or undergo nonradiative processes. A CW Ar+ laser with minimum energy corresponding to the $S_0 \rightarrow S_1$ transition was used for measuring the PL spectrum. Since PL originates from singlet exciton radiative recombination, magneto-photoluminscence (MPL) cannot directly originate from SE (S=0) (which is *B*-independent); but rather is caused indirectly by nonradiative decay channel of singlet excitons collisions with TE or polaron pairs, of which density varies with *B.*

The same experimental set-up used for PA and MPA measurement was used for measuring the MPL response. The PL emitted light was collected using spherical mirrors and was dispersed by using an Acton 300 monochromator for measuring the spectrum. The dispersed light was measured using appropriate solid-state photodetectors such as

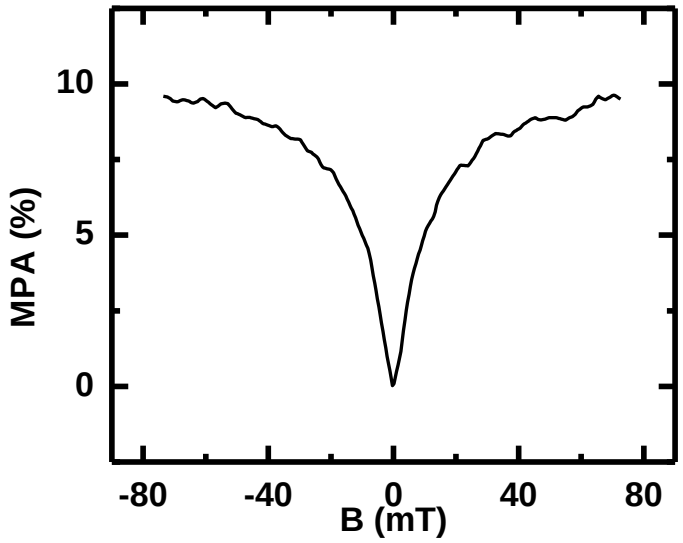

Figure 2.13. Magneto-photoinduced absorption response of irradiated MEHPPV film measured at 50 K.

silicon or germanium photodiodes. In order to measure the MPL response, the monochromator was fixed at a PL band, and PL was measured while sweeping the magnetic field. The PL spetrum of MEHPPV film is shown in Figure 2.14. The transitions involving the creation of vibrational quanta in the ground state are assigned as 0-0, 0-1, and 0-2 in the PL spectrum. Figure 2.15 shows the typical MPL response of MEH-PPV film.

2.6.5. X-ray Diffraction Measurement

X-ray diffraction (XRD) technique is used to identify the crystalline phases, determine, the lattice constant and microcrystalline grain size. We can estimate the inter-planar spacing '*d*' and hence lattice constant according to Bragg's law of diffraction,

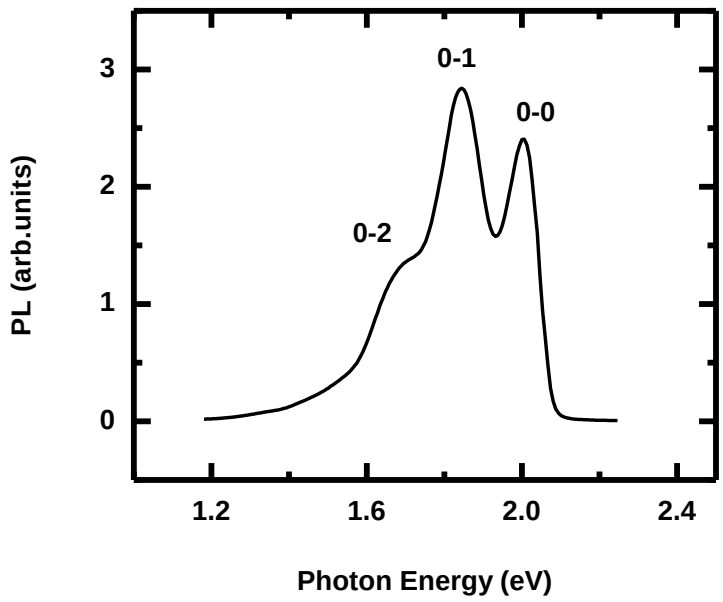

Figure 2.14. Photoluminscence spectrum of Pristine MEHPPV film at 50 K.

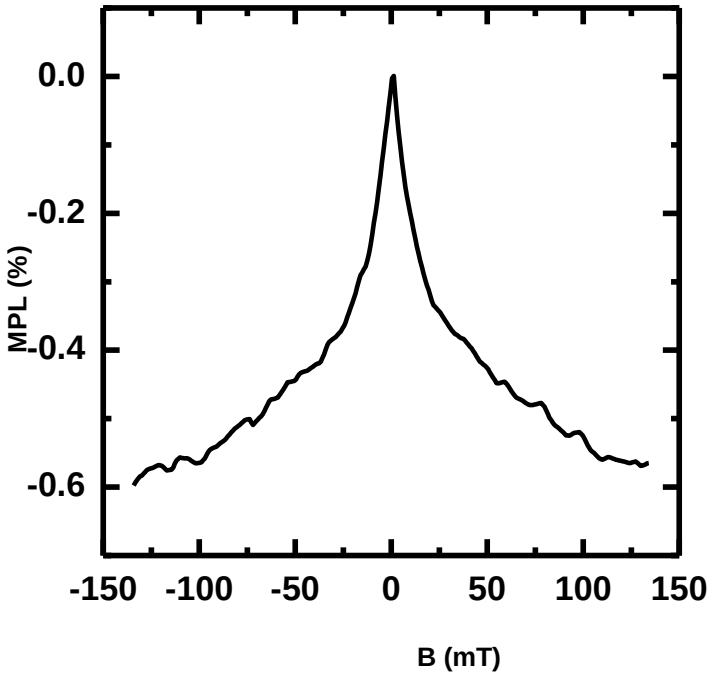

Figure 2.15. Magneto-photoluminscence response of pristine MEHPPV film measured at 50 K.

$$2d\sin\theta = n\lambda \tag{2.16}$$

where 2θ is the scattered angle between the incident and scattered X-ray, n is the diffraction order, and λ (=0.154 nm) is the wavelength of the incident beam.

The grain size '*L*' of the polymer crystallite may be estimated using the Scherrer's relation

$$L \sim \frac{0.9\lambda}{\Delta_{2\theta}\cos\theta} \tag{2.17}$$

where $\Delta_{2\theta}$ is the full width at half maximum (FWHM) of the peak. The peak position and $\Delta_{2\theta}$ values are analyzed using the X'Pert Plus crystallographic analysis software.

The morphology of the semicrystalline polymer films was studied by XRD technique. For the XRD measurements, about 200 nm thick polymer film was made on a glass substrate (2.5mm X 2.5mm area) either with spin-coating or with thermal evaporation. The XRD pattern was then obtained using a Philips powder diffractometer equipped with CuK_α source at 45 kV and 40 mA power setting. The grazing incidence method was used to measure the XRD pattern from thin films.

Figure 2.16 shows the typical grazing incidence XRD patterns from C_{60} films using the CuK_α X-ray line at λ=0.154 nm as a function of the diffraction angle (2θ).

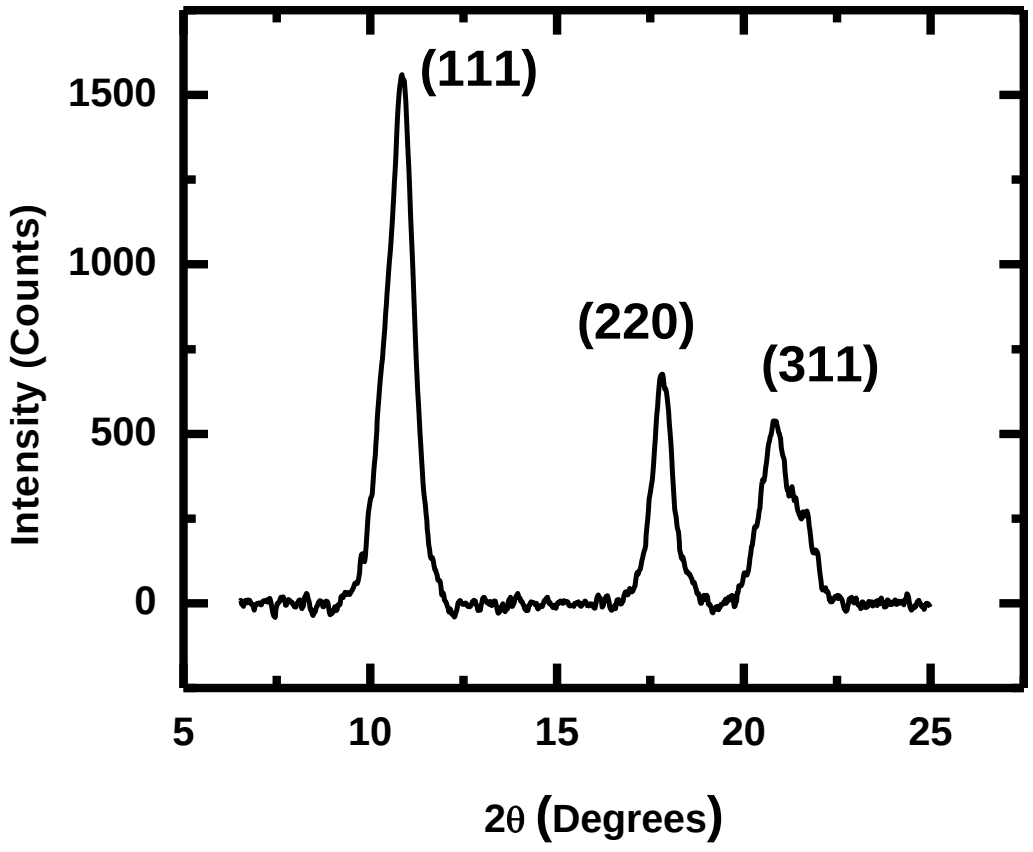

Figure 2.16. X-ray diffraction patterns of a C_{60} film, where the background scattering was removed for clarity. The numbers represents various (hkl) Bragg bands.

CHAPTER 3

MAGNETIC FIELD EFFECT IN ORGANIC DIODES

3.1 Introduction

Magnetoconductance (MC) and magneto-electroluminescence (MEL) in organic light emitting diodes (OLEDs) [19-33] are two aspects of the broader research area of "magnetic field effect" (MFE) in the organics [31], which includes field-induced changes in chemical and bio-chemical reaction yields, magneto-luminescence and magneto-phosphorescence, magneto-photoconductance, etc. Typically, the organic MFE response has been observed at relatively low fields ($|B|$ <100 mT) and various temperatures, and may be as large as ~20% [32]. It has been generally accepted that the organic MFE originates from the field influence on long-lived radical spins in solutions [31], or polarons in organic solids and devices [27, 28]. For obtaining substantial MFE response, the electron spin relaxation rate should be sufficiently small so that magnetic field-induced spin manipulation may occur [31].

Various models have been proposed for explaining the MFE response in devices where the active layers are π-conjugated organic semiconductors (OSEC). Most of these models are based on the hyperfine interaction (HFI) between the injected spin ½ carriers

and the nuclear spins in the OSEC layer [23-28]. The most common model considers the HFI mixing of spin sublevels of bound polaron-pairs (PP), where the level-mixing becomes less effective as B increases [27]. Recently [33], by replacing the protons (H) with deuterons (D) in the π-conjugated polymer interlayer, where the D-polymer has a smaller HFI constant, a_{HFI}, it was unambiguously demonstrated that the HFI indeed plays a crucial role in the MFE of polymer diodes.

3.2 Experimental

The devices used in our measurements were 5 mm^2 diodes, where the OSEC spacers were deposited on a hole transport layer: poly(3,4-ethylenedioxythiophene) [PEDOT]-poly(styrene sulphonate) [PSS]. For the bipolar devices, we capped the bilayer structure with a transparent anode: indium tin oxide [ITO], and a cathode: calcium (protected by aluminum film). The hole-unipolar device was in the form of ITO/PEDOT-PSS/organic layer/Au; whereas the electron-unipolar device was Al/LiF(~2nm)/organic layer/Ca/Al. Very weak or no EL was detected in these unipolar devices. The organic diodes were transferred to a cryostat with variable temperature that was placed in between the two poles of an electromagnet producing magnetic fields up to ~300 mT with a 0.1 mT resolution. By increasing the distance between the two magnetic poles, we improved the resolution down to 0.01 mT; in all cases, B was determined with a calibrated magnetometer. Device I-V characteristics were measured using a Keithley 236 Source-Measure unit. A silicon photo-detector connected with the oriel preamplifier and Keithley 2400 system was used to measure the electroluminescence from the bipolar devices. The devices were driven at constant bias, V, using a Keithley 236 apparatus; and

the current, *I*, and electroluminescence, *EL*, were simultaneously measured while sweeping *B*. Magnetic field-induced fractional change in current or electroluminescence, ΔX/X (dubbed MX), is defined by

$$\frac{\Delta X}{X} = \frac{X(B) - X(B=0)}{X(B=0)}$$

where X=I or EL.

3.3 Experimental Results and Discussion

3.3.1 Magnetoconductance Response in Organic Diodes at Ultra-small Fields

While most research activities in the field of MFE in OLED have been focused on an intermediate magnetic field regime (~100 mT) [19-30], less attention has been given to understand the effect of magnetic fields that are comparable to the earth's magnetic field and much smaller than the hyperfine coupling. The existence of ultra-small magnetic field effect (USMFE) opposite to the normal magnetic field effect was first predicted by Brocklehurst in 1976 [43] and USMFE has been observed for variety of reactions in solutions [31, 44, 45]. After the recognition of magnetic sense in animals and concern over the possible health hazard due to electromagnetic fields, it has been investigated in detail. These observations motivated us to study the USMFE in organic devices.

Here, we include in our study very small fields ($|B|$<1-2 mT) and extend our measurements to a variety of *unipolar* and *bipolar* organic devices. We show that the MC(B) response in fact contains a peculiar sign reversal at ($|B|$<1-2 mT), similar to that reported earlier in the MEL response of polymer OLED [33]. This ultra-small MFE (or USMFE) component manifests itself as MC sign reversal from positive (negative) to negative (positive) in bipolar (unipolar) devices, forming a dip (peak) at B_m that scales with the half-width at half-maximum, ΔB, of the normal MC(B) response. We found, however, that the USMFE in polymers has different width in electron- and hole–unipolar polymer diodes, indicating different hyperfine interaction constant for the electron-polaron and hole-polaron in these materials. We explain the complete MC(B) response using a model Hamiltonian based on "spin pairs" of loosely bound spin ½ polarons with small exchange, having HFI with several strongly coupled nuclear spins. The spin-pairs are composed of either same charges (unipolar devices) or opposite charges (bipolar devices). In this model, the intermixing between the hyperfine-split spin sublevels increases at very small $\boldsymbol{B}$ due to level-crossing at B=0, thereby causing a MC sign reversal.

We have studied MC in organic diodes based on a variety of π-conjugated polymers and small molecule spacers. The polymers include: polyfluorene, two derivatives of poly(phenylene-vinylene) [PPV], namely 2-methoxy-5-(2'-ethylhexyloxy) [MEH-PPV], and three isotope enriched 2-methoxy-5-(2'-dioctyloxy) [DOO-PPV]. The latter include H-DOO-PPV (fully protonated-hydrogen), D-DOO-PPV (deuterated-hydrogen rich), and C13-DOO-PPV (^{13}C-carbon rich). The three isotope rich DOO-PPV polymers have *different* a_{HFI} since skeletal protons (nuclear spin I=½) are replaced by

deuterium (I=1) in D-DOO-PPV (causing *smaller* a_{HFI}); whereas some of the ^{12}C nuclei (I=0, no HFI) are replaced by ^{13}C nuclei (I=½ having substantial HFI), thus increasing the effect of the HFI. The small molecules that we studied include tetracene, pentacene, rubrene, and several fullerenes (only a subset is shown here). We fabricated organic diodes from all of these materials, and subsequently measured the MC response with high field resolution at various bias voltages and temperatures. By shielding the measuring apparatus from the earth magnetic field (B_E≈0.053 mT in Utah) using mu-metal shield, we verified that the USMFE is not caused by B_E.

Figure 3.1 shows the MC(B) response of several bipolar diodes for $|B|$<50 mT at room temperature and $V>V_{BI}$, where V_{BI} is the device built-in potential, at which both positive and negative charges are injected into the active layer [7]. For $|B|$>~2 mT, MC is positive, reaching a saturation level, MC_{max}, at large B. This is the *normal* MC(B) response [19-30] that is characterized by HWHM, ΔB ranging from 2.8 mT for D-DOO-PPV, to 6.2 mT for H-DOO-PPV, to 9.1 mT for ^{13}C-DOO-PPV; as summarized in Figure 3.1(c). The isotope-dependent ΔB (where ΔB increases with a_{HFI}) for the three DOO-PPV polymers shows that the HFI plays a crucial role in determining the MC response in polymeric organic diodes, as reported in [33] for EL(B) response.

However, a surprising MC(B) response is observed at $|B|$<1-2 mT (Figure 3.1(b)): where upon decreasing B, the MC reverses its sign, reaching a minimum, MC_{min} at $B=B_m$, followed by an increase toward zero MC at B=0. We have measured a number of devices for each material and found the results to be reproducible. When the USMFE response is summarized by plotting B_m vs. ΔB (Figure 3.1(c)), it is apparent that B_m increases with ΔB (i.e., larger a_{HFI}).

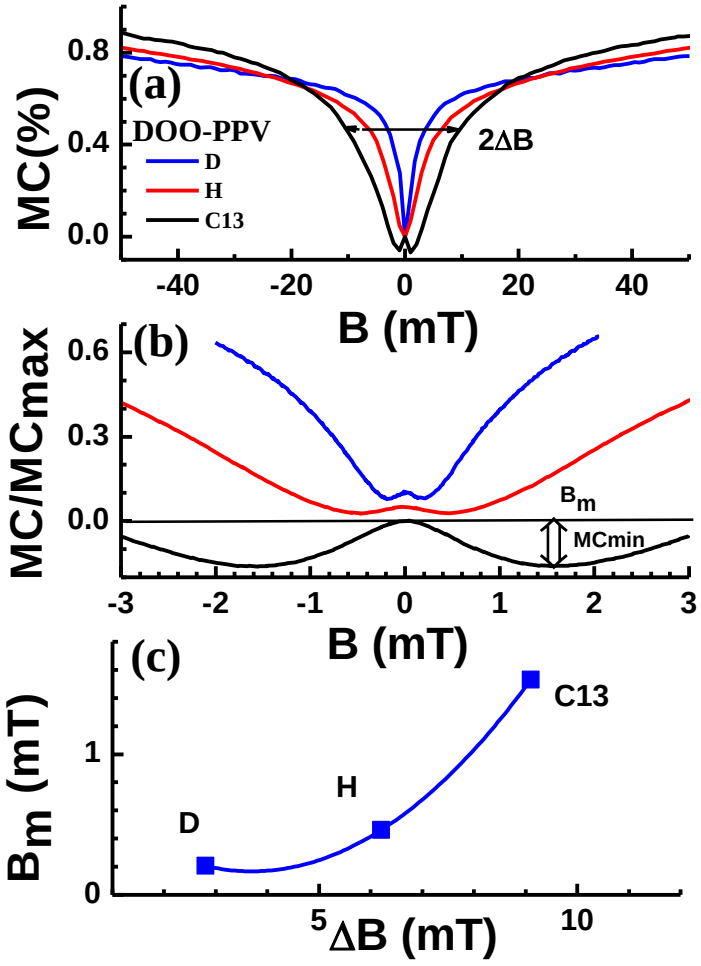

Figure 3.1. Magnetoconductance (MC) response vs. field, *B* in bipolar organic diodes based on: three isotopes of DOO-PPV Panel (a) shows MC(*B*) for |*B*|<50 mT; whereas panel (b) shows the *normalized* MC(*B*) measured with high field resolution, for |*B*|<3 mT (some MC responses are shifted vertically for clarity); MC_{max} is the saturation MC value at large *B*. Δ*B* is the HWHM for the normal MC(*B*) response, as defined in (a); whereas MC_{min} and B_m are for the USMFE response, as defined in (b). Panel (c) summarizes B_m vs. Δ*B* for the MC(*B*) responses in (a) and (b); the straight line is guide to the eye.

The USMFE response component was obtained in most organic devices based on various polymers and small molecules. The normal and ultra-small MC(B) response of three additional devices are shown in Figure 3.2(a) and 3.2(b), respectively. Figure 3.2(c) summarizes B_m vs. ΔB for the MC(B) responses in (a) and (b).

The USMFE component in the MC(B) response depends on both bias voltage and temperature (Figure 3.3 for D-DOOPPV). At 10 K, we found that $|MC_{min}|$ decreases by a factor of 2 as the bias increases from 3.4 to 4.4 V, whereas B_m does not change much. At V=3.4 V, we found that $|MC_{min}|$ increases as the temperature increases from 10 to 300 K, whereas B_m is not affected by the temperature. Importantly, the dependence of MC_{min} with V and T is found to follow the same dependencies as the saturation value, MC_{max}; so the ratio, MC/MC_{max} is *independent* on V and T (Figure 3.3 insets). This indicates that the USMFE is *correlated* with the normal MC response, and therefore is also determined by the HFI in the polaron-pair species. We thus conclude that any viable model which explains the normal MC(B) response needs to also explain the USMFE response component.

The USMFE response is not limited to bipolar devices. In Figure 3.4, we show MC responses of hole-only and electron-only MEH-PPV diodes. The high-field MC in both devices is *negative* (Figure 3.4(a)) [28], and thus the USMFE appears as 'negative-to-positive' sign reversal with *maximum* at B_m~0.8 mT for the electron-only device, and B_m~0.1 mT for the hole-only device (Figure 3.4(b)). Importantly, ΔB is smaller in the hole-only device compared to the electron-only device; this is consistent with smaller a_{HF} for holes than for electrons that was recently measured in a similar polymer [46]. We therefore conclude that B_m increases with ΔB in unipolar devices similar to bipolar

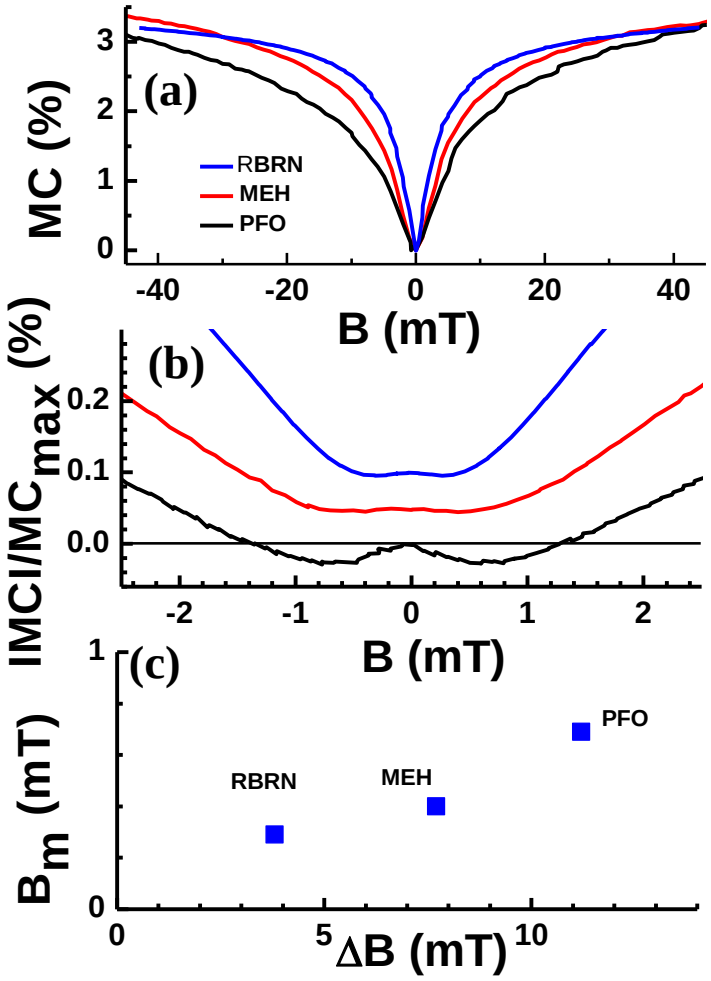

Figure 3.2. Magnetoconductance (MC) response vs. field, *B* in bipolar organic diodes based on MEH-PPV, PFO (MCx3), and rubrene RBRN; (MCx8). Panel (a) shows MC(*B*) for |*B*|<50 mT; whereas panel (b) shows the *normalized* MC(*B*) measured with high-field resolution, for |*B*|<3 mT (some MC responses are shifted vertically for clarity). Panels (c) summarizes B_m vs. ΔB for the MC(*B*) responses in (a) and (b).

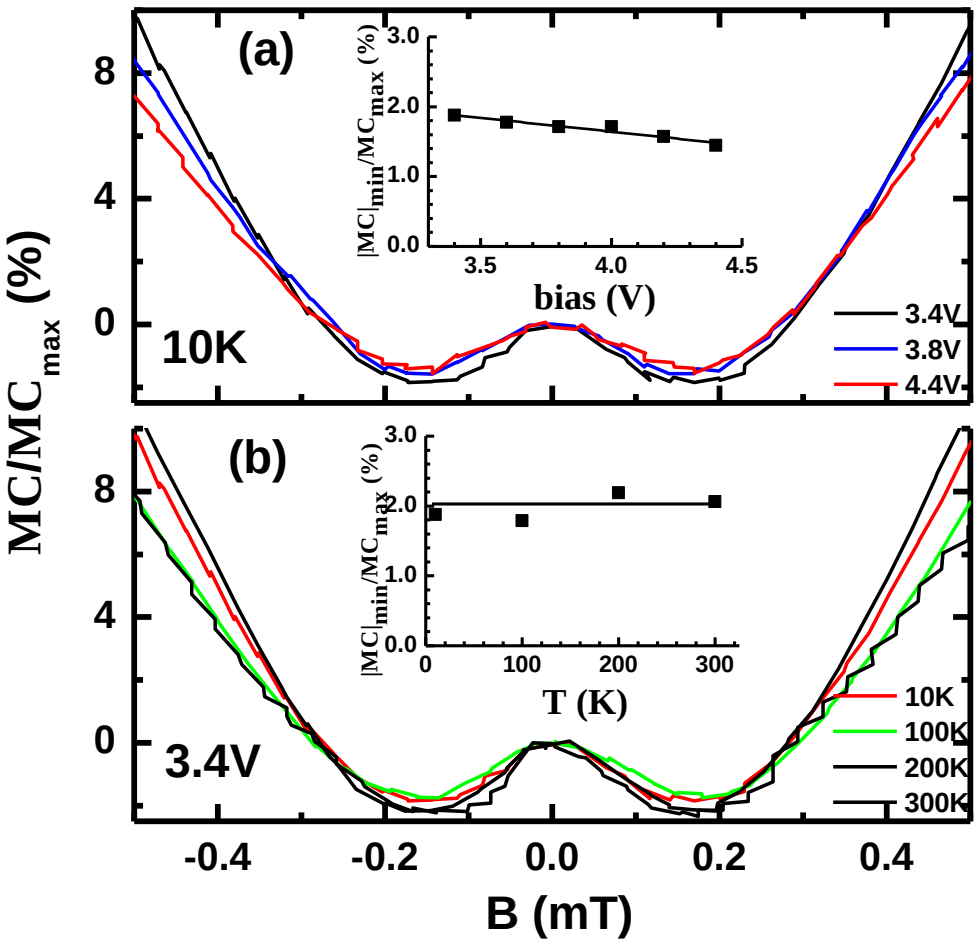

Figure 3.3. Normalized MC(*B*) response of a bipolar diode based on D-DOO-PPV for |*B*|<0.5 mT at (a) various bias voltages at *T*=10 K, and (b) various temperatures at *V*= 3.4 Volt; MC_{max} is defined in Figure 3.1. The insets in (a) and (b), respectively summarize MC_{min}/MC_{max} at various voltages at 10 K, and various temperatures at 3.4 Volt.

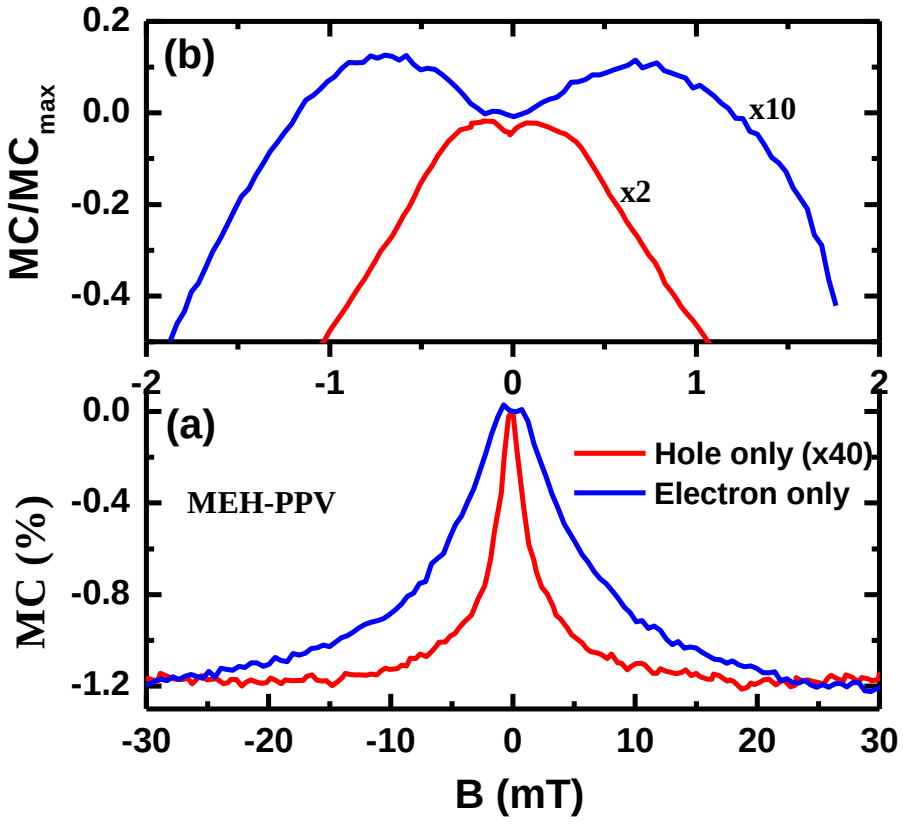

Figure 3.4. Normalized MC(*B*) response for (a) |*B*|<30 mT, and (b) |*B*|<2 mT of hole- and electron-only *unipolar* diodes based on MEH-PPV, measured at room temperature and *V*=3 Volt and 20 Volt, respectively. For clarity, the MC(B) responses are multiplied by a factor in (b).

devices.

We also observed the isotope dependence for H- DOO-PPV and C13-DOO-PPV h-unipolar devices shown in Figure 3.5. The monotonic, high-field MC component in these unipolar devices is also negative (Figure 3.5(a)) [28], and thus the USMFE response here appears as‘negative-to-positive’ sign reversal with a pronounced maximum at B_m. Figure 3.5(b) shows that B_m ~ 0.15mT for the H-DOO-PPV hole-only device, whereas B_m ~ 0.4mT for the C13-DOO-PPV hole-only device.

In the traditional view of organic MC, the injected spin ½ carriers form weakly bound polaron spin pairs, SP, in either singlet $(SP)_S$ or triplet $(SP)_T$ spin configuration. As B increases, the intermixing between the singlet and triplet configurations (S-T intermixing) decreases due to the increased Zeeman contribution, thereby affecting their respective populations; this leads to a *monotonous*, $MC_M(B)$, response [27, 28]. However, if the exchange interaction constant $J\neq0$, then a new $MC_{LC}(B)$ component emerges at $B\approx B_{LC}=J$, where a singlet-triplet level-crossing (LC) occurs giving rise to *excess* spin intermixing between the singlet and triplet SP manifolds. The $MC_{LC}(B)$ component has therefore an *opposite* sign with respect to $MC_M(B)$ response, which results in a strong MC(B) modulation at $B=B_{LC}$ [31]. By explicitly taking into account the HFI between each of the SP constituents and N (≥1) strongly coupled neighboring nuclei, we explain the newly discovered USMFE response as due to a level-crossing response at B=0.

Our model is based on the time evolution of the SP spin sublevels in a magnetic field. For bipolar devices, the SP species is the polaron-pair, whereas for unipolar devices, the SP species is a π-dimer (i.e. biradical, or bipolaron [24, 28]). The SP spin Hamiltonian, $\boldsymbol{H}$, includes exchange interaction (EX), HFI and Zeeman terms: $\boldsymbol{H}$ =

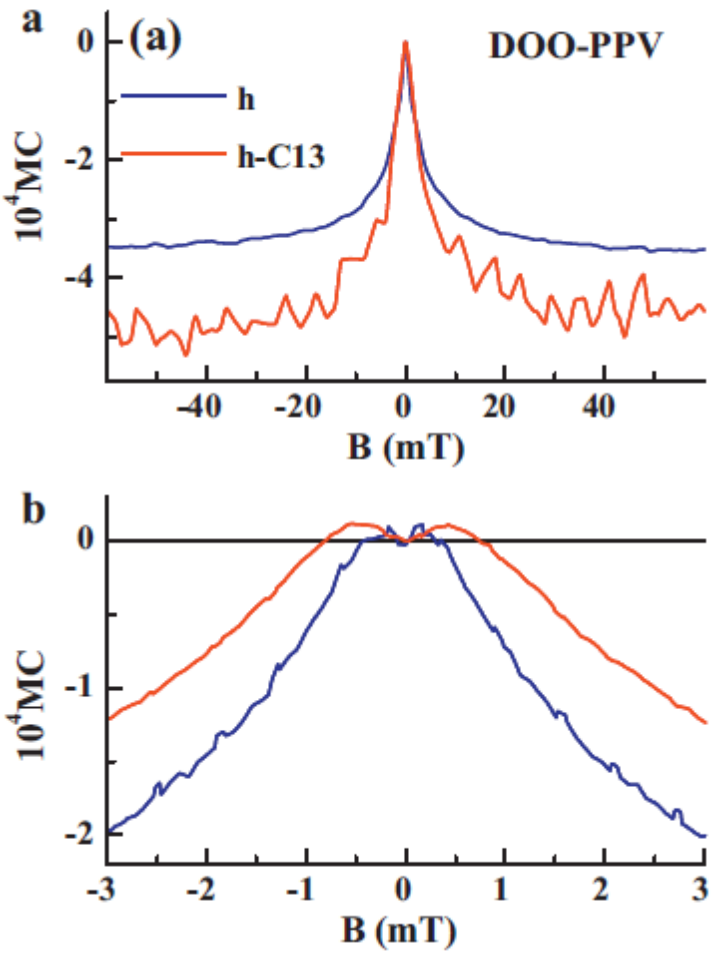

Figure 3.5. Normalized MC(B) response for (a) |B| < 60mT, and (b) |B| < 3mT of hole-only unipolar diodes based on H- and C13-DOO-PPV, measured at room temperature.

$H_{\text{Zeeman}}+H_{\text{HFI}}+H_{\text{ex}}$; where $H_{HF}=\sum_{i=1}^{2}\sum_{j=1}^{Ni}[S_i\cdot\tilde{A}_{ij}\cdot I_j]$ is the HFI term, $\tilde{A}$ is the hyperfine tensor describing the HFI between polaron (i) with spin S_i (=½) and N_i neighboring nuclei, each with spin I_j, having isotropic a_{HFI} constant; $H_{\text{Zeeman}} = g_1\mu_B BS_{1z}+ g_2\mu_B BS_{2z}$ is the electronic Zeeman interaction component; g_i is the g-factor of each of the polarons in the SP specie (we choose here $g_1 = g_2$); μ_B is the Bohr magneton; $H_{ex}=J\mathbf{S}_1\cdot\ \mathbf{S}_2$ is the isotropic exchange interaction; and **B** is along the **z**-axis. All parameters in the

Hamiltonian ***H*** are given in units of magnetic field (mT). An example of the spin energy sublevels using the spin Hamiltonian ***H*** for $N_1=N_2=1$, and I=½ (namely, overall 16 wavefunctions) is shown in Fig. 3.6(a). Note the multiple level-crossings that occur at *B*=0. Other level-crossings appear at larger *B*, but those are between mostly triplet sublevels that hardly change the S-T intermixing rate and consequent $(SP)_S$ and $(SP)_T$ populations.

The steady state $(SP)_S$ and $(SP)_T$ populations are determined by the spin-dependent generation and decay rates. The effective decay rate constant, *k,* is composed of dissociation rate (that contributes to the device current density [47]) and recombination rate (for bipolar diodes); these two processes eliminate the SP species. The SP spin sublevel populations are also influenced by the S-T intermixing coupling. Any change of the S-T intermixing rate, such as produced by increasing **B,** may perturb the overall relative steady state spin sublevel populations; and through the SP dissociation mechanism, it may consequently contribute to MC(*B*) . To obtain sizable MC value, $k < a_{HFI}$. The USMFE response in this model results from the strong coherent S-T inter-conversion of nearly degenerate levels at $B<<a_{HFI}/g\ \mu_B$ where a_{HFI} is the isotropic HFI constant.

The relevant time evolution of the S-T intermixing that determines the steady state SP_S population is obtained in our model via the time dependent density matrix ρ(t). Solving the spin Hamiltonian, ***H,*** for the energies E_n and wavefunctions Ψ_n, we express the time evolution of the singlet population ρ_S(t) as [31, 48]:

$$\rho_S(t) = Tr[\rho(t)P^S] = \frac{4}{M}\sum_{m,n=1}^{M} |P_{mn}^S|^2 \cos\omega_{mn}t \ , \qquad (3.1)$$

where P^S_{mn} are the matrix elements of the $(SP)_S$ projection operator, $\omega_{mn}=(E.1_n-E_m)/\hbar$, and M is the number of spin configurations included in the SP species (for I=½ $M=2^{N+2}$). In the absence of a spin decay mechanism, Equation (3.1) contains many rapidly oscillating terms that do not contribute to the singlet steady state population, and two important terms that do not oscillate in time. These are: $<\rho_S(t=\infty)>=4\Sigma_m|P^S_{mm}|^2/M +4\Sigma_{m\neq n}|P^S_{mn}|^2/M$, where the second summation is restricted to accidental *degenerate levels*, for which $\omega_{mn}(B)=0$. The first (diagonal) term contributes to the "normal" monotonous $MC_M(B)$ response, whereas the second ("level crossing") term contributes to $MC_{LC}(B)$ response that modulates $<\rho_S(t=\infty)>$ *primarily* at $B=0$, where the S-T degeneracy is relatively high (see Fig. 3.6(a)). The combination of the monotonous $MC_M(B)$ and $MC_{LC}(B)$ components at $B\sim0$ explains in principle the USMFE response in organic devices.

When the SP spin species decays, $\rho_S(t)$ in Equation (3.1) needs to be multiplied by a decay function $f(t)$. Under these conditions, the steady state $(SP)_S$ decay yield, $\Phi_S \equiv k\int_0^\infty \rho_S(t) f(t) dt$ is given by:

$$\Phi_S(B) = (4/M)\sum_{m=1}^{M}\sum_{n=1}^{M} |\, P^S_{mn}\,|^2 \; f(\omega_{mn}) \qquad (3.2)$$

where $f(\omega) = k\int_0^\infty \cos\omega t\, f(t) dt$. When SP_S elimination is controlled by an exponentially decaying function $f(t)\propto\exp(-kt)$, we have $f(\omega)=k^2/(k^2+\omega^2)$.

The triplet yield in this model is given by, $\Phi_T(B) =[1-\Phi_S(B)]$ [33]. If the SP singlet and triplet dissociation rates into polarons are equal to each other, then their

relative contribution to the device conductivity would not change with B in spite of their field-induced population change, resulting in null MC(B) response. We account for the dissociation rate difference by expressing MC(B) as the weighted average [33]:

$$MC(B) = \frac{\Phi_S(B) + \delta_{TS}\Phi_T(B)}{\Phi_S(0) + \delta_{TS}\Phi_T(0)} - 1, \tag{3.3}$$

where $\Phi_S(B)$ is given by Equation (3.2) and δ_{TS} is the triplet-singlet "symmetry breaking" parameter that describes the relative S-T contributions to the device conductance via dissociation into free polarons.

Figure 3.6(b) shows the calculated MC(B) response using Equations 3.1-3.3 for an axially symmetric anisotropic HFI with $N_1=N_2=1$ (I=½; M=16), where a_{HFI}(electron)=3a_{HFI} (hole)=3 mT, J=0, δ_{TS}=0.96, and an exponential SP decay $\hbar k / a_{HFI} = 0.001$. The calculated MC($B$) response captures both the obtained experimental USMFE response at small B, as well as an approximate $B^2/(B_0^2+B^2)$ shape at larger B, where $B_0 \approx 1.5a_{HFI} \approx 4.5$ mT. The excellent agreement between theory and experiment, including both B_m and the USMFE shape and relative amplitude, validates the model used.

3.3.2 Magneto-electroluminescence (MEL) Response in Organic Diodes at Ultra-small Fields

Electroluminescence in the OLEDs results from recombination of polaron pairs (PP) in the spin singlet configuration. The electrons and holes that are injected into the

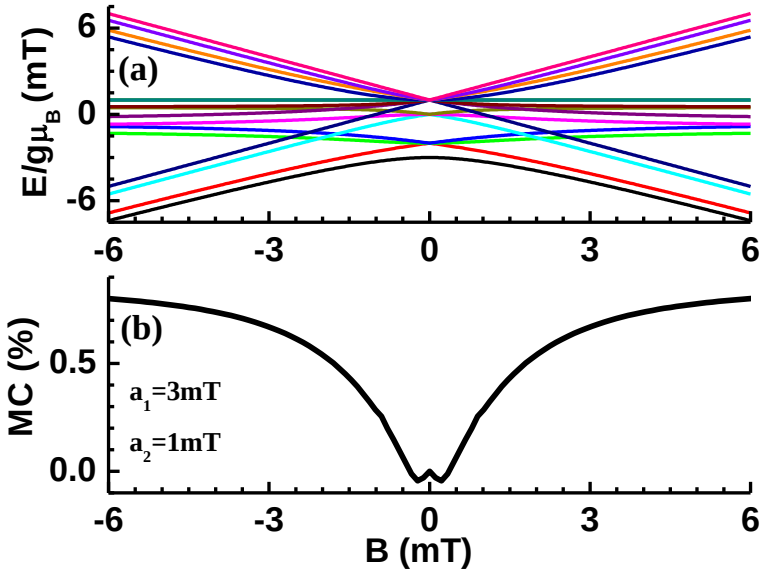

Figure 3.6. Calculated spin energy levels and magnetoconductance. (a) Example of calculated spin energy levels vs. *B* for a spin pair with isotropic HFI; a_1=3, a_2=3 mT, and *J*=0. Note the multiple level-crossing at *B*=0. (b) Calculated MC(*B*) response for a SP with axially symmetric HFI averaged over all magnetic field directions. The isotropic HFI is the same as in (a). The anisotropic HFI component is $a_{zz}=0.15a_i$ for the respective SP constituent.

active layer via the metal electrodes can form loosely bound singlet (PP_S) and triplet polaron pairs (PP_T) depending upon the mutual polarons' spin configuration. Following the PP generation, they may undergo three possible processes. They (i) may combine to form excited state singlet excitons (SE) and triplet excitons (TE), (ii) can dissociate into free charge carriers again, or (iii) can exchange spins via intersystem crossing (ISC). SEs may decay radiatively, resulting in electroluminescence. The long-lived TEs may decay nonradiatively or show delayed fluorescence via the process of triplet-triplet annihilation.

The steady state PP density depends on the PP_S and PP_T "effective rate constant", γ, which is the sum of the formation, dissociation, and recombination rate constants, as

well as triplet-singlet (T-S) mixing via intersystem crossing (ISC). If the effective rates, γ_S for PP_S and γ_T for PP_T, are not identical to each other, then any disturbance of the T-S mixing rate, such as by the application of an external magnetic field, **B**, would perturb the dynamic steady state equilibrium that consequently results in a change of the device electro-luminescence (MEL), as well as the conductance (MC). It has been generally accepted that the organic MEL originates from the field-induced changes in the dynamics of long-lived loosely coupled polaron pairs (PP) in organic solids and devices [27, 32]. In a recent paper [33], it has been experimentally shown that the hyperfine interaction is responsible for the mixing of the spin sublevels of the PP species. This was achieved by replacing protons with deuterons (D) in the π-conjugated polymer chains, where the D-polymer has smaller HFI constant, a_{HFI}. The obtained MEL(B) response was narrower in the D-polymer, in accordance with the reduced HFI constant.

In this section, using high magnetic field resolution, we show USMFE response component in MEL(B) response in most organic devices based on various polymers and small molecules. We measured a number of devices for each material and found the results to be reproducible. Figure 3.7 shows the normal and ultra-small MEL response of OLED devices based on MEHPPV polymer as an active layer. Similar response was observed in MC(B) of devices based on the same active layer. We also measured MEL(B) response of the small molecule rubrene, as shown in Figure 3.8.

The MEL(B) response in both cases is composed of two regions: (i) a "sign-reversal" region at $|B| < 1–2$ mT, where MEL(B) reverses its sign reaching a maximum absolute value $|MEL|_m$ at $B = B_m$, and (ii) a monotonic region at $|B| > \sim 2$mT, where MEL(B) monotonically increases having an approximate Lorentzian line shape with half

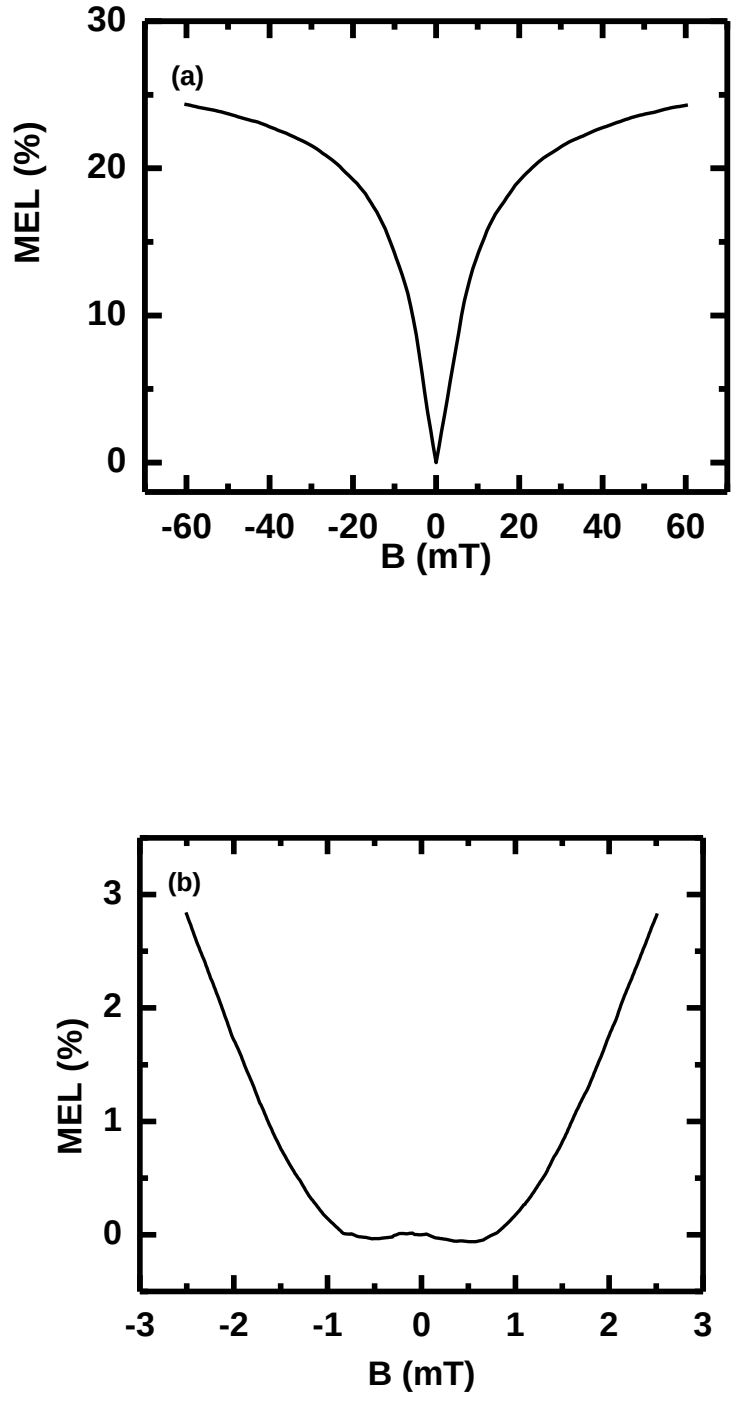

Figure 3.7. Magneto-electroluminescence (MEL) response vs. field, *B* in bipolar organic diodes based on MEHPPV polymer as an active layer. Panel (a) shows MEL(*B*) for $|B|<60$ mT; panel (b) shows the MEL(*B*) measured with high field resolution, for $|B|<3$ mT.

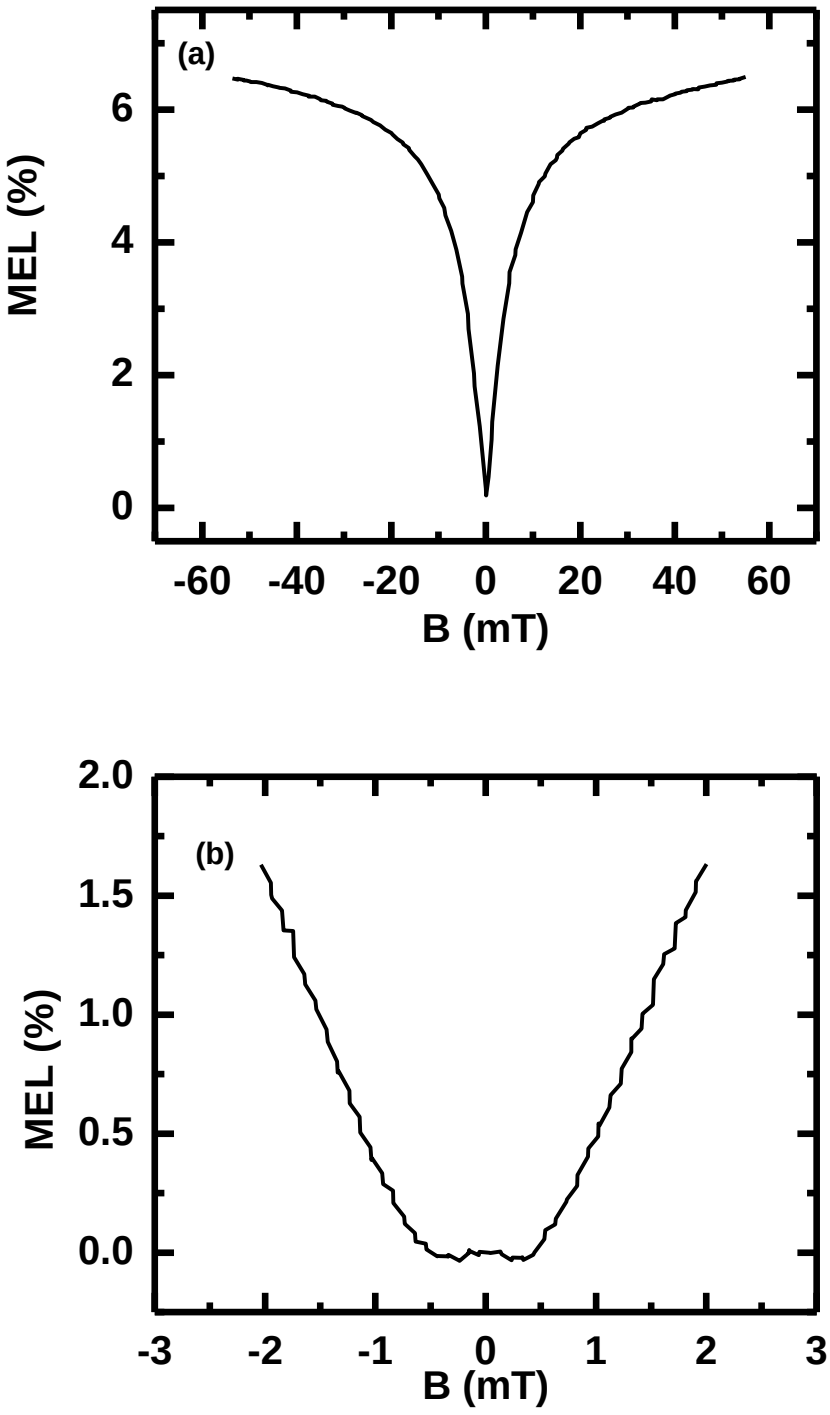

Figure 3.8. Magneto-electroluminescence (MEL) response vs. field, *B* in bipolar organic diodes based on rubrene small molecule as active layer. Panel (a) shows MEL(*B*) for $|B|<60$ mT; panel (b) shows the MEL(*B*) measured with high field resolution, for $|B|<3$ mT.

width at half maximum, ΔB. We explained the entire MEL(B) response, including the "normal" monotonic region, as well as the "sign reversal" region using a simple model Hamiltonian based on PP having HFI with several nuclear spins (same as explained detail in Section 3.3.1). In this model, the intermixing between the hyperfine-split spin sublevels increases at very small B due to level-crossing at B = 0, thereby causing a sign reversal.

3.3.3 Illumination Effect on Magnetoconductance Response of MEHPPV Devices

MEH-PPV films are somewhat unusual in the class of π-conjugated polymers since their photoinduced absorption (PA) spectrum may change according to the environment/mixture used, as previously shown in detail [49]. Films of pristine MEH-PPV that are kept in the dark for a long time show fairly strong PL emission (quantum efficiency of about 25%), and their PA spectrum consists of long-lived triplet excitons; but do not support long-lived photogenerated polarons, probably because of small density of imperfections and impurities in the film. However, if the same films are exposed to prolonged UV illumination, a meta-stable state is formed due to photoinduced native defects in the film, in which long-lived polarons are photogenerated and the photoluminescence (PL) emission is considerably quenched [49].

Here, we make use of this property of MEH-PPV and measured the effect of illumination on MC(B) response in three different types of organic diodes with the configuration of ITO/PEDOT/MEH-PPV/Ca/Al, ITO/PEDOT/MEH-PPV/Au, and ITO/AL/MEH-PPV/Ca/ Al for bipolar, hole unipolar, and electron unipolar diodes,

respectively. Figure 3.9 shows the MC(B) response of these devices based on pristine MEH-PPV polymer. The bipolar diode shows positive MC, whereas negative MC was observed for both e-unipolar and h-unipolar diodes [28, 32]. Figure 3.10 shows the MC(B) response of a pristine and UV irradiated MEH-PPV bipolar device. It is clearly seen that upon UV illumination, there is a significant increase in MC of the organic device. Similar effects were observed in X-ray exposed organic diode based on Alq_3 [50], and electrically conditioned PPV devices [51, 52]. This enhancement in MC can be explained by defect generation within the organic active layer upon irradiation. Figure 3.11 (a) is the effect of the illumination on the MC(B) response in h-unipolar device. In the dark, the MC response of this device is negative. Upon prolonged illumination, however, we obtained a gradual change in the MC(B) magnitude the h-unipolar MEH-PPV device; the MC first decreases then changes sign from negative to positive. A possible mechanism for this effect is that the light-induced metastable polarons [49] in the illuminated polymer initiate more polaron pairs generation having opposite charge in the device upon current injection, and these PP species are responsible for the obtained positive MC with illumination.

Figure 3.11 (b) shows the effect of illumination on the MC response of the e-unipolar device. There is no sign reversal in MC of these unipolar devices upon prolonged illumination. This could be due to the creation of metastable electron defects in the polymer layer upon illumination, so that PP species of different charges are not formed.

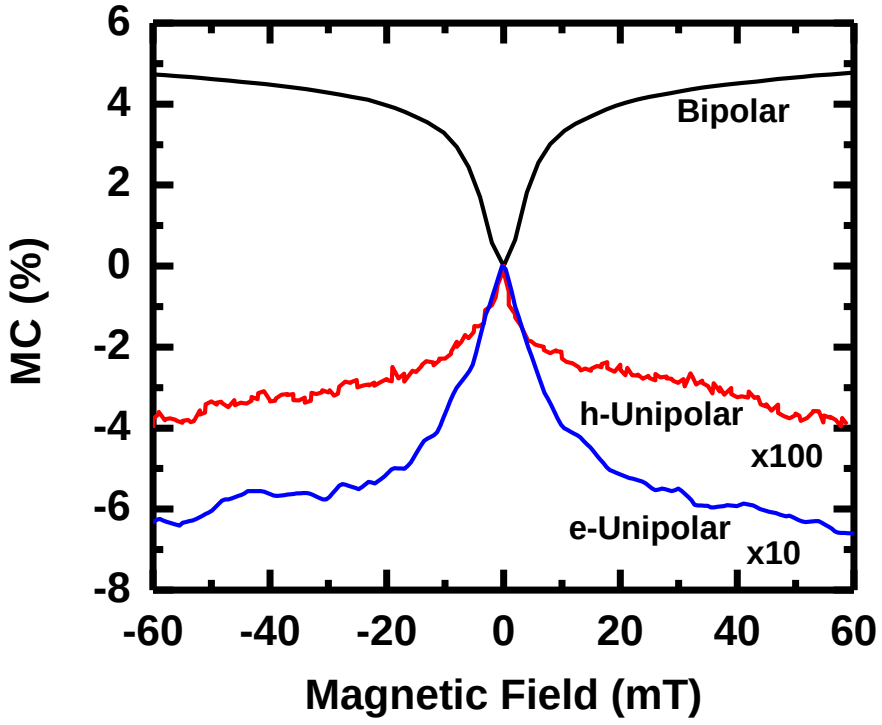

Figure 3.9. Magneto-conductance MC(B) response in bipolar, hole-only, and electron-only unipolar organic diodes based on MEHPPV. The latter responses are multiplied by a factor of 100 and 10, respectively.

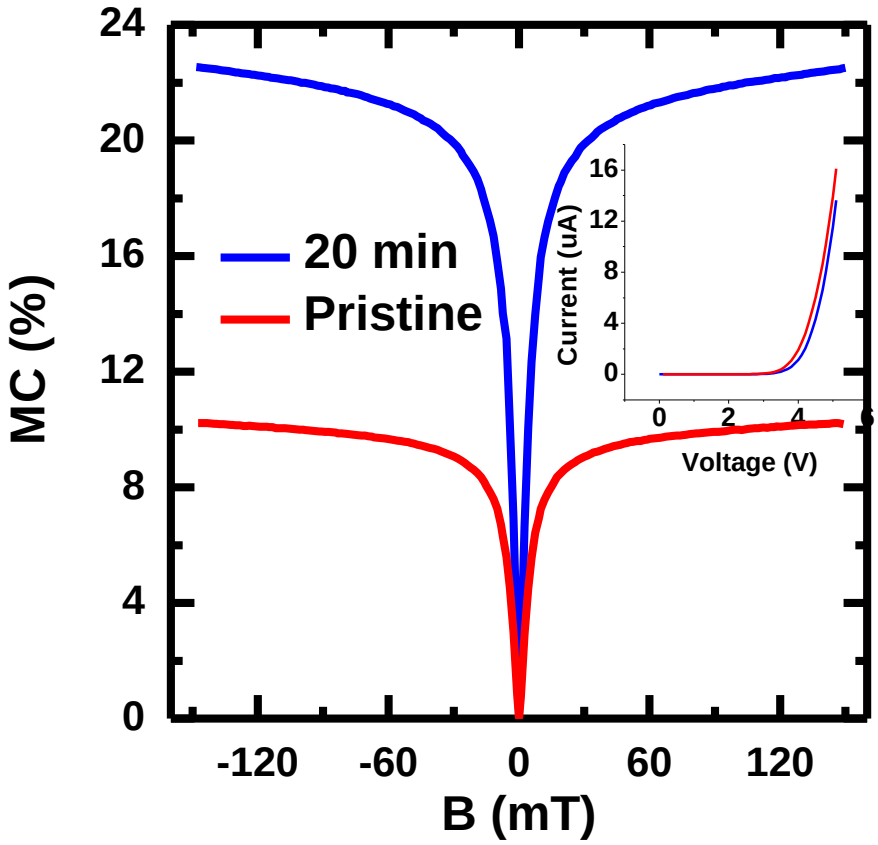

Figure 3.10. Magnetoconductance MC(B) response in pristine and UV irradiated (20 min) MEHPPV OLED, measured at 10 K.

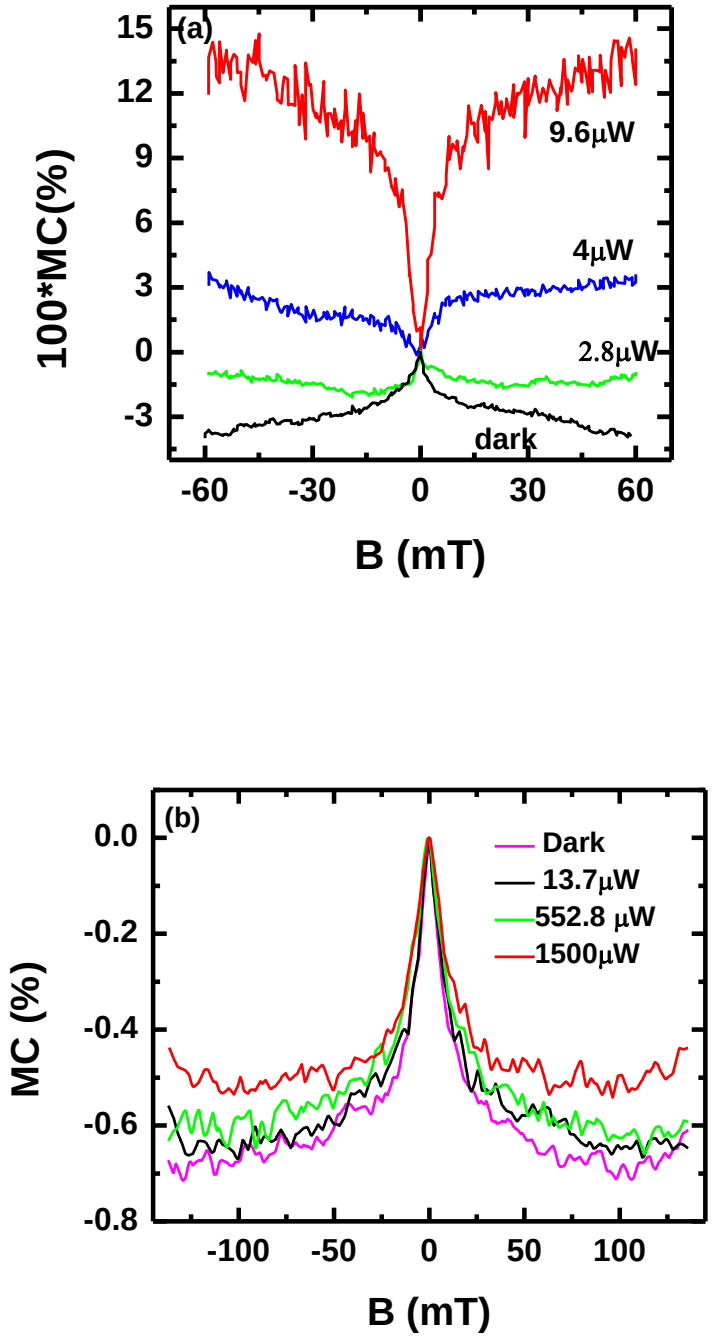

Figure 3.11. MC(B) response of (a) hole-only and (b) electron-only unipolar devices at 10 K, illuminated with 532 nm laser for 30 minutes at different power.

3.4 Conclusion

In summary, we found a novel USMFE response at $B<<a_{HFI}$ in many bipolar and unipolar organic diodes, which demonstrates that MC(B) and MEL(B) response is much richer than anticipated before. The USMFE component scales with the more regular MC(B) response, and is thus also due to the HFI influence of the SP pairs. Our simple model explicitly includes in the SP Hamiltonian the most strongly interacting nuclear spins, and is capable of reproducing the entire MFE(B) response, including the new USMFE component. Our findings show that, via the USMFE component, relatively small B is capable of substantially altering both electrical and electro-optical response in organic diodes, as well as *chemical, and biological reactions* discussed elsewhere[31], and thus should be seriously considered. In fact, a chemical USMFE has been proposed to be at the heart of the 'avian magnetic compass' in migratory birds. In this respect, our work shows that the USMFE appears in MFE response of many more organic compounds that has been thought before. We also found that prolonged illumination of the organic layer dramatically changes the performance of the organic devices. We found enhancement in MC of bipolar device, and sign reversal in h-unipolar device upon illumination. Positive MC observed in irradiated unipolar device supports the polaron-pair mechanism.

CHAPTER 4

MAGNETIC FIELD EFFECT IN ORGANIC FILMS

4.1 Magnetic Field Effect on Excited State Spectroscopies of π-Conjugated Polymer Films

4.1.1 Introduction

The intensive studies of magnetic field effect, such as magnetoconductance (MC) and magneto-electroluminescence (MEL) in organic light emitting diodes [19-33], was boosted in 2004 as the first prototype organic spin valve was demonstrated revealing the existence of relatively long spin coherence length in the organics [7]. Various mechanisms responsible for the MC and MEL in organic diodes have emerged from these studies. Some models emphasized the influence of magnetic field on carrier mobility in the device [24, 27, 53, 54], while other models emphasized the influence of the magnetic field on the carrier density, brought about by spin-dependent microscopic processes among polaron-pairs (PP) or triplet excitons (TE) [22, 33, 55]. A variety of spin-mixing mechanisms have been proposed, including the hyperfine interaction (HFI) between polarons and the skeleton protons in π-conjugated polymers [42, 33]; the difference, Δg, in the electron and hole g-factors in polymer/fullerene blends [31]; a number of mechanisms that involve TE [22, 55]; and the spin-orbit coupling in small molecules that

in the electron and hole *g*-factors in polymer/fullerene blends [31]; a number of mechanisms that involve TE [22, 55]; and the spin-orbit coupling in small molecules that contain heavy atoms [56]. Thus, the magnetic field effect in organic diodes has proven to be an especially rich and interesting research field.

Here, we report a novel magnetic field effect of spectrally resolved photoinduced absorption (PA) and photoluminescence (PL) [dubbed hereafter MPA and MPL, respectively] in π-conjugated polymer *films* (as opposed to the previously studied organic diodes [57]), and apply it to study a number of spin-dependent processes. This 'spectroscopic-sensitive' magnetic field effect technique differs from the previously studied 'transport-related' MC and MEL in devices in two important respects. (i) Since PA and PL measure directly the density of the photoexcitations (such as PP or TE), then MPA and MPL can be directly related to the photoexcitation spin density. Consequently, by directly comparing the MPA and MPL responses in films to those of MC and MEL in organic diodes based on the same organic active layer, we are able to relate the magnetic field effect in organic diodes to the spin *densities* of the excitations formed in the device. (ii) Being a spectroscopic technique, we can use the MPA as a new tool to discern various long-lived photoexcitations in organic semiconductor films. In addition, we deduce the main spin-dependent species and/or spin-mixing mechanism that determine the MPA (MPL) response in three different forms of a π-conjugated polymer, including spin-mixing in PP species, triplet-triplet annihilation, spin-mixing among the triplet spin sublevel, and Δg mechanism of PP in polymer/fullerene blends.

We studied MPA and MPL responses in a prototype π-conjugated polymer, namely MEH-PPV, which is a derivative of poly(phenylene vinylene). The three different

forms that we studied are: pristine film; film exposed to prolonged UV illumination; and electron donor in MEH-PPV/PCBM blend having weight ratio 1:1. The chemical structures of MEHPPV and PCBM are shown in Figure 2.1 [(d), and (k), respectively (Chapter-2)]. A schematic diagram of the philosophy underlying the MPA technique is presented in Figure 4.1. For obtaining PA, the film is excited by a continuous wave (cw) laser beam with above-gap photon energy that generates steady state singlet excitons (SE; $S_0 \rightarrow S_1$). The SE may either radiatively recombine ($S_1 \rightarrow S_0$); or convert into long-lived TE via intersystem crossing; or separate into positive and negative charge polarons, some of which may form long-lived PP. These various secondary reactions are symbolized by $S_1 \rightarrow X_0$, where X stands for species such as PP, TE, and pairs of TEs. The X species has an excited state transition $X_0 \rightarrow X_1$ (PA_X), which is activated by a weak probe beam. PA is defined as the negative fractional change in transmission, *T*: $PA(E)=(-\Delta T/T)=N_{SS}\beta(E)$, where N_{SS} is the species *steady state density*, β (E) is the photoexcitation optical cross-section, and *E* is the probe beam photon energy. Therefore, in a magnetic field, *B*, $PA_X(B)$ is determined by the density $N_{SS}(B)$; which, in turn is controlled by the X species decay rate coefficient, κ(B) [$N_{ss}=G/\kappa$] For $B\neq0$, the X_0 level splits according to the relevant spin multiplicity, *L (L*=3, 4, and 9, respectively, for the S=1 TE; PP composed of two S=½ polarons; and a pair of TEs). Consequently, through specific spin-mixing processes, the spin content of each sublevel, its decay rate κ, and thus N_{SS} and consequently PA all become *B*-dependent, and consequently $MPA_X(B)\equiv[PA_X(B)-PA_X(0)]/PA_X(0)$ is formed. In contrast, since it originates from singlet exciton radiative recombination, MPL(*B*) cannot directly originate from SE (S=0) (which is *B*-independent); but rather is caused indirectly, for example via SE collision with TE.

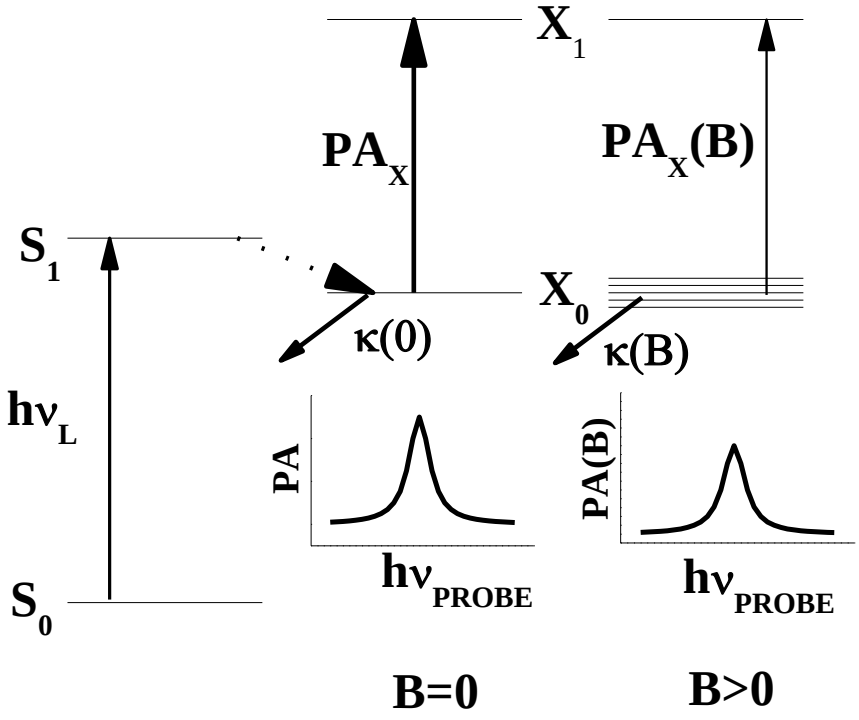

Figure 4.1. Schematic illustration of the magnetic field dependent pump-probe PA processes. (a) The pump beam with above gap photon energy $h\upsilon_L$ excites the polymer MEH-PPV to the singlet exciton (SE) level ($S_0 \rightarrow S_1$). The SE relaxes via intersystem crossing to a triplet exciton (TE) or ionizes into separate charges forming polaron pair, PP ($S_1 \rightarrow X_0$). The steady state density of the X species is controlled by the spin-dependent decay coefficient, κ. The incandescent probe beam monitors the photoinduced absorption, PA ($X_0 \rightarrow X_1$, PA_X), which is proportional to the X_0 steady state density. In a magnetic field $B>0$, X_0 splits according to its spin multiplicity, and the decay rate of each spin sub-level becomes field dependent, resulting in a B-dependent density and PA_X (thus forming MPA_X).

The work is arranged as follows. The experimental technique is described in Section 4.1.2. In Section 4.1.3 we describe our experimental results on the three forms of MEH-PPV, including comparative studies of films and devices. In pristine MEH-PPV films, we assign the MPA as due to the TTA mechanism, while the MPL is assigned to TE-polaron scattering. In irradiated MEH-PPV films, we propose that the PP mechanism with hyperfine interaction-mediated spin mixing is responsible for the obtained MPA. The same mechanism combined with a mechanism related to the different g-values of positive and negative polarons ('Δg mechanism') play a dominant role in the MEH-PPV/PCBM blend film. In Section 4.1.4 we describe an all-purpose quantum mechanical model which may explain the magnetic field effect obtained in the three MEH-PPV polymer forms. The model is based on the time evolution of the photogenerated species spin-sublevels in a magnetic field in the presence of spin-dependent decay mechanism. This model is viable for both MPA measurements in films as well as MC and MEL in devices made of the same polymers. Using this model, we show that the magnetic field dependent excitation density may account for the measured magnetic effect in the MEH-PPV system, including MPA, MPL, MC, and MEL.

4.1.2 Experimental

For the MC and MEL measurements, we fabricated ~5 mm^2 diodes, where the organic spacers were deposited on a hole transport layer: poly(3,4-ethylenedioxythiophene) [PEDOT]-poly(styrene sulphonate) [PSS]. We capped the bilayer structure with a transparent anode: indium tin oxide [ITO], and a cathode: calcium (protected by aluminum film). The devices were driven at constant bias, *V*. For the PL

and PA measurements, we used a standard photomodulation set-up described in Section 2.6.2. For excitation, we used a cw Ar^+ laser pump beam at $\hbar\omega_L$=2.54 eV that was modulated at frequency *f*; and an incandescent tungsten/halogen lamp as the probe. The PA signal, $\Delta T/T$ is the fractional change, ΔT in transmission, *T*, which is negative for PA, and positive for photobleaching (PB). The PA signal was measured using a lock-in amplifier referenced at *f*, a monochromator, and various combinations of gratings, filters, and solid-state photodetectors spanning the spectral range $0.3<\hbar\omega(\text{probe})<2.3$ eV. This set-up was also used for measuring the PL spectrum. The device (or film) was placed in a cryostat in between the two poles of an external magnetic field up to 300 mT. For obtaining the desired magnetic field response, the measured quantity, such as PA and PL in films, and EL and current in diodes, was measured while sweeping *B*.

MEH-PPV films are somewhat unusual in the class of π-conjugated polymers since their PA spectrum may change according to the environment/mixture used, as previously shown in detail [49]. Films of pristine MEH-PPV that are kept in the dark for a long time show fairly strong PL emission (quantum efficiency of about 25%), and their PA spectrum consists of long-lived triplet excitons, namely PA_T (Figure 4.2 (a)); but do not support long-lived photogenerated polarons, probably because of small density of imperfections and impurities in the film. However, if the same films are exposed to prolonged UV illumination, a meta-stable state is formed due to photoinduced native defects in the film, in which the PA spectrum also contains substantial long-lived photogenerated polarons having two characteristic PA bands (PA_P) that are formed on the expense of both PL and PA_T [49]. The process is reversible when subjected to elevated temperatures in the dark. Furthermore, when the MEH-PPV donor-like polymer is mixed

with a fullerene acceptor-like molecule forming bulk heterojunction morphology, then the photogenerated excitons ionize to form positive polarons on the polymer and negative polarons on the fullerene molecule [6]. We took advantage of these MEH-PPV film properties to obtain MPA of various photoexcitation species using the same polymer film; namely, before and after prolonged UV illumination, and in blend with fullerene molecules, namely [6,6]-phenyl-C_{61}-butyric acid methyl ester (PCBM).

4.1.3 Experimental Results

4.1.3.1 Pristine MEH-PPV Films

In Figure 4.2 (a), we show the PA spectra of pristine MEH-PPV film at B=0 and 100 mT, respectively. The spectrum consists of a broad PA band centered at ~1.37 eV (marked T) that is assigned to TE transition (PA_T) [49]; no other PA bands were obtained down to 0.2 eV, attesting to the good quality of the polymer used here. The B=100 mT spectrum is identical in shape to that of B=0, except that is slightly weaker. The difference, ΔPA spectrum is similar to PA_T, demonstrating that it relates to the TE density. As seen in Figure 4.2 (b), the magnetic field response, $MPA_T(B) \equiv \Delta PA/PA_T$, varies strongly with the laser excitation intensity, I_L, and thus with N_{SS} (which is proportional to I_L). N_{SS} is also inversely proportional to the sublevel TE effective recombination rate constant, $\kappa=\sum\kappa_\alpha$ $(\alpha=1,..,L)$, which are B-dependent. At small I_L, $MPA_T(B)$ monotonically decreases, but it gradually transforms into a more complex response at large I_L where two components are resolved; a low-field MPA component that decreases with B, and a high-field component that increases with B. We thus conclude that $MPA_T(B)$ is dominated by two different spin-mixing mechanisms related

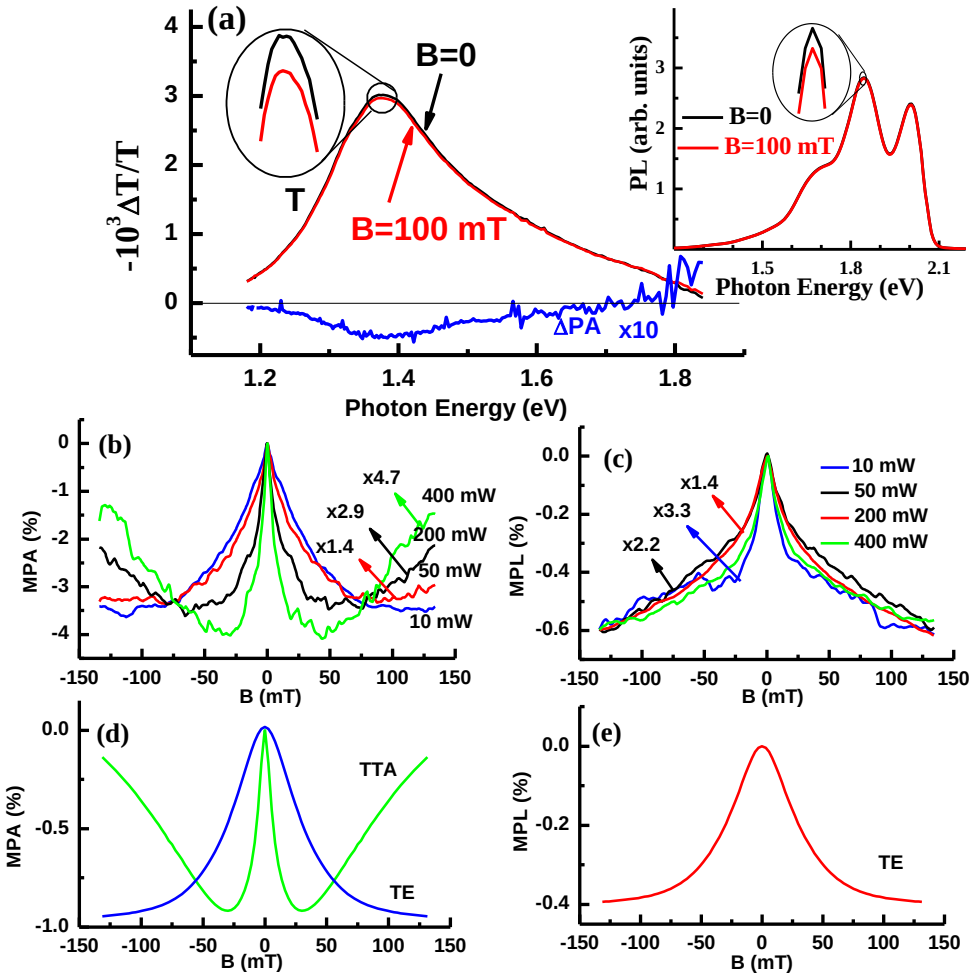

Figure 4.2. Excited state spectra (PA and PL) and magnetic field effects in pristine MEH-PPV films. (a) The triplet PA band, PA_T at B=0 and 100 mT (black and red lines, respectively), respectively, generated using a laser excitation at $h\upsilon_L$=2.54 eV @ I_L=200 mW/cm^2, and their difference spectrum ΔPA_T=[PA_T(100mT)-PA_T(0)] (blue line). The region near the peak is magnified (within a circle). Right inset: PL spectrum at B=0 (black line) and 100 mT (red line), respectively. The lines in the circles show the data on a higher resolution scale. (b) $MPA_T(B)$ response measured at 1.37 eV probe, for various laser excitation intensities (normalized). (c) MPL(B) response measured at 2.05 eV probe for various laser excitation intensities (normalized). (d) Model calculations of $MPA_T(B)$ response using the TE mechanism (blue line, corresponds to the 10 mW data in (b)) and TTA mechanism (green line, corresponds to the 400 mW data in (b)) mechanisms; see text. (e) Model calculation of MPL(B) response using the model of singlet exciton quenching by TE (SE-TE collision, see text).

with TE species; one mechanism that dominates at low $I_{L,}$ which may be a 'single-TE' process; and the other mechanism that increases at large I_L, and therefore most likely involves 'triplet-triplet annihilation' (TTA) process.

The same pristine MEH-PPV film also shows MPL response. Figure 4.2 (a) inset displays the PL spectrum at *B*=0 and 100 mT, respectively, that consists of several vibronic replicas, with 0-0 transition at 2.05 eV. The difference, ΔPL spectrum follows the PL spectrum, and is thus assigned to the $S_1 \rightarrow S_0$ transition (Figure 4.1). Unlike $MPA_T(B)$, however, Figure 4.2 (c) shows that MPL(*B*) does not change with I_L; it monotonically decreases with *B*, similar to the low intensity $MPA_T(B)$, i.e., the low-field component. Since singlet excitons alone cannot depend on the magnetic field, we therefore assign this MPL(*B*) response as due to SE *nonradiative decay* that is activated by 'collisions' with TE species, of which density $N_{SS}(B)$ also determines the $MPA_T(B)$ response at low I_L.

4.1.3.2 Irradiated MEH-PPV Films and Devices

Entirely different characteristic PA and MPA properties were measured in the same MEH-PPV film after prolonged UV irradiation (~150 minutes using a Xenon lamp at 50 K), which supports photogenerated polaron species [49]. Figure 4.3 (a) shows the PA spectrum of irradiated MEH-PPV film at *B*=0 and 100 mT, respectively, at similar excitation intensities as used above for the pristine film. The spectrum in this case consists of two broad PA bands; one centered at ~0.4 eV, which is assigned to the lower polaron transition (marked 'P_1'); and the other is asymmetric with a peak at ~1.4 eV (marked '$T+P_2$'), which is composed of the polaron P_2 transition centered at ~1.55 eV,

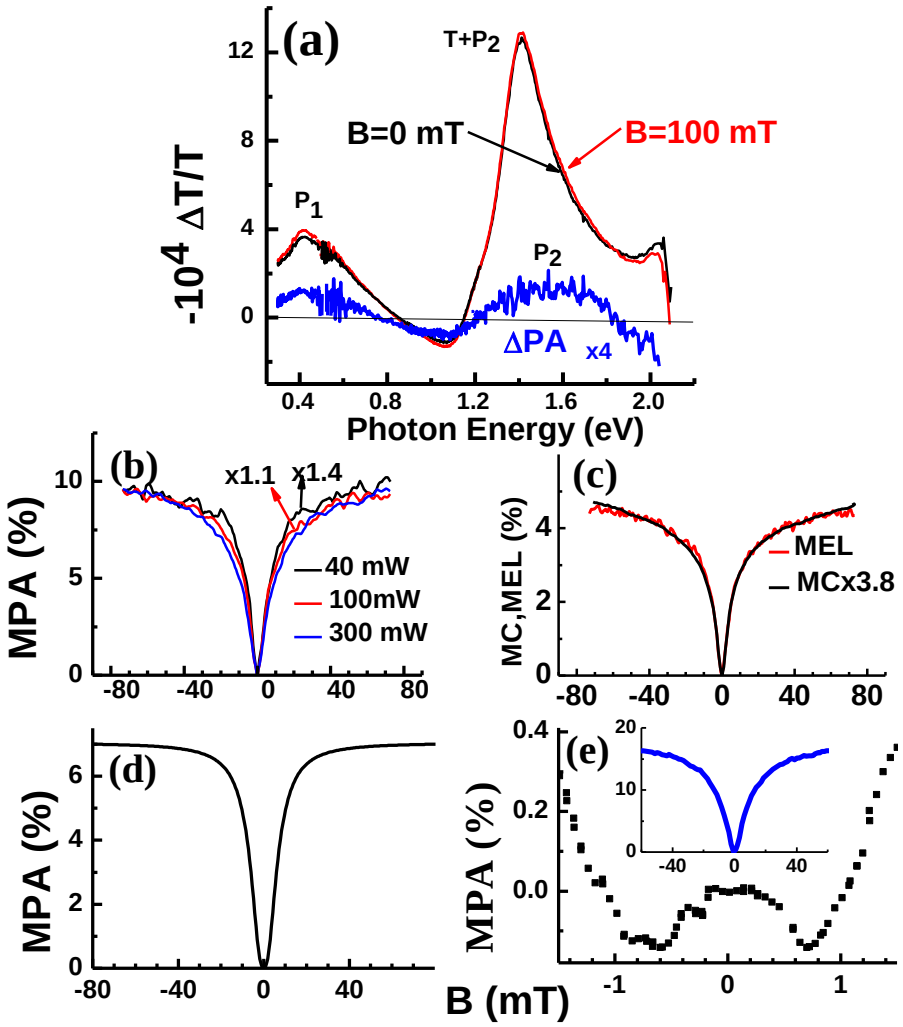

Figure 4.3. Excited state spectra and magnetic field effects in UV irradiated MEH-PPV film and in organic light emitting diode. (a) PA spectrum at I_L=100 mW/cm^2 for *B*=0 (black line) and *B*=100 mT (red line), respectively, and their difference spectrum, ΔPA=[PA(100mT)-PA(0)] (blue line) in MEH-PPV film. (b) MPA(*B*) response measured at 1.4 eV probe for various laser excitation intensities (normalized). (c) MEL(*B*) and MC(*B*) responses in MEH-PPV diode. (d) Model calculations of MPA_{PP}(*B*) response in MEH films using the PP mechanism (see text). (e) MPA(*B*) response at 1.1 eV probe up to *B*=1.5 mT (filled squares) and *B*=60 mT (blue line, inset).

and the remnant of the TE transition, PA_T [49]. The spectrally resolved difference ΔPA (Figure 4.3 (a)) shows that MPA in this MEH-PPV form is correlated only with the two polaron PA bands, P_1 and P_2, but not with that of PA_T. This is one of the MPA technique advantages; *its ability to spectrally resolve the dominant species and spin-dependent process*. We assign ΔPA spectrum here to magnetic field dependence of the PP's density, namely ΔPA_{PP}. Unlike the negative ΔPA_T of the pristine sample (Figure 4.2 (a)), we found $\Delta PA_{PP}>0$ in the irradiated sample, which suggests that a different spin-mixing mechanism is dominant in the present case. The positive, monotonically increasing $MPA_{PP}(B)$ (Figure 4.3 (b)) is naturally explained by the PP mechanism, in which the spin-mixing is governed by the HFI [33] (see below).

For comparison, we also show MC(B) and MEL(B) (Figure 4.3 (c)) obtained in MEH-PPV diodes. The MC and MEL responses are identical to each other; and, in addition, *are very similar to the* $MPA_{PP}(B)$ response shown in Figure 4.3 (b)). This indicates that all three magnetic field effects share a common origin. Since MPA(B) does not involve carrier transport, we conclude that MC(B) and MEL(B) obtained in the devices *need not involve transport*. All three responses can be explained equally well by the microscopic PP model presented below, that involves magnetic field dependence of the species' spin sublevel character and their *density*, rather than transport related mechanism through the organic interlayer in the device.

A salient feature of the low field (B<1.2 mT) $MPA_{PP}(B)$ response is shown in Figure 4.3 (e). Interestingly, this response (dubbed here ultra-small MPA, or USMPA) was measured at 1.1 eV probe photon energy, where the PA spectrum actually shows photo-bleaching (PB, Figure 4.3 (a)). The 1.1 eV MPA is shown on a larger B-scale in

Figure 4.3 (e) inset; it has, in fact the same response as MPA at 1.4 eV. The USMPA response decreases at B<0.6 mT before increasing again to form the monotonic response seen at larger fields. Similar nonmonotonic response was previously observed in both MC(B) and MEL(B) in organic diodes [42, 58], and was explained as due to level-crossing at B=0 that involves spin sublevels formed by the polaron-proton HFI in the polymer chains. Thus, the same explanation is viable also for the USMPA component here. We note that the USMPA is not related to transport in an organic device; in addition, it occurs at field values close to the *earth magnetic field* (≈0.05 mT). We thus infer that the USMPA in polymers (and other organic molecules [42]) could, in principle, be used by a variety of living creatures on earth that may take advantage of the earth magnetic field to augment their activity; such as navigation for example, as shown previously [59].

4.1.3.3 Films and Devices of MEH-PPV/PCBM Blends

Yet, a third type of MPA response is viable in films of MEH-PPV/PCBM blend. Upon laser excitation of the polymer (PCBM does not absorb in the visible spectral range), the singlet excitons quickly dissociate into hole-polarons on the MEH-PPV chains and electron-polarons on the PCBM molecules [6]. This weakens the PL intensity of the MEH-PPV chains, and completely eliminates the triplet PA_T band from the PA spectrum [60]. Thus, the PA spectrum in this case (Figure 4.4 (a)) consists of PA of positive polarons on the MEH-PPV chains (P_1 at ~0.4 eV, and P_2 at ~1.37 eV, respectively), as well as PA band of negative polarons on the PCBM (C_{61}^- at ~1.2 eV). Importantly, the positive and negative polarons have different gyro-magnetic g-values [61], with

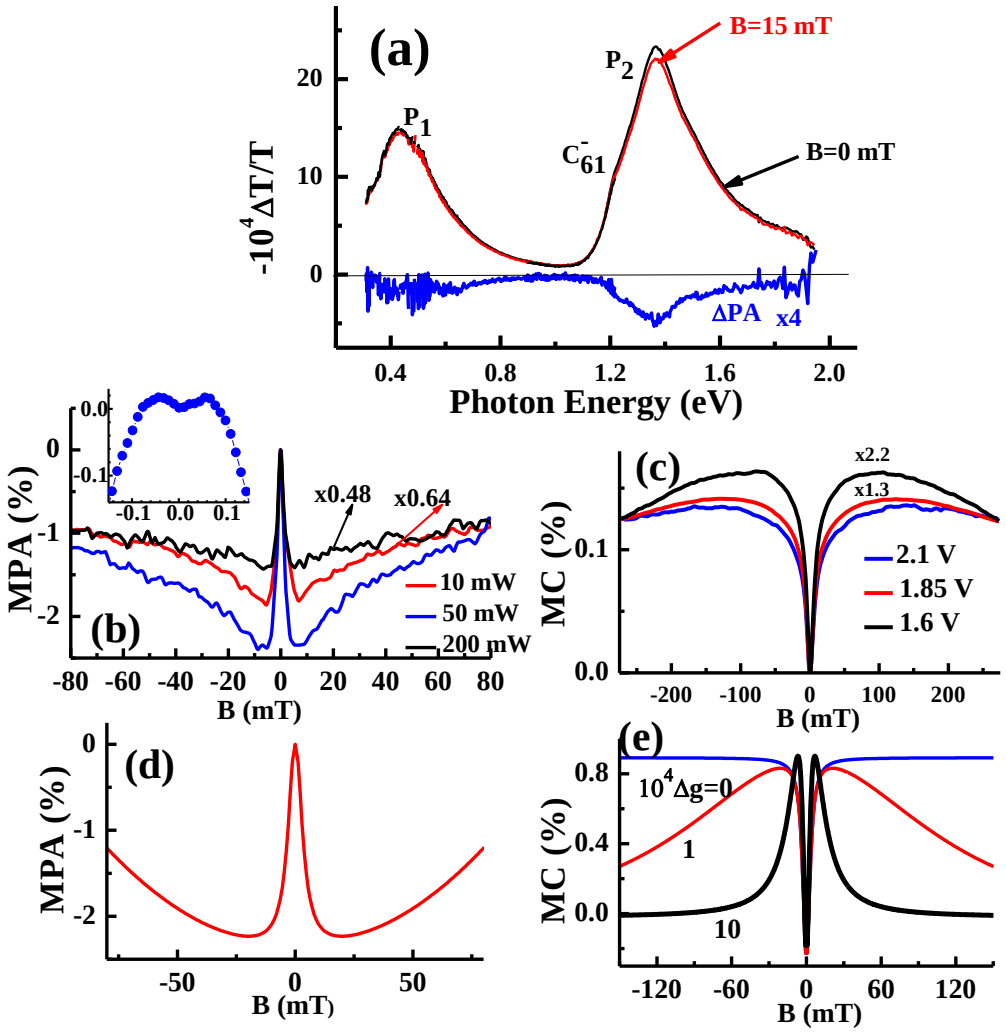

Figure 4.4. Excited state spectra and magnetic field effects in MEH-PPV/PCBM film and diode. (a) PA spectrum of MEH-PPV film at I_L=mW/cm^2 for *B*=0 (black line) and *B*=15 mT (red line), respectively, and their difference spectrum, ΔPA=PA(15mT)-PA(0) (blue line). (b) MPA(*B*) response measured at 1.37 eV probe for various laser excitation intensities (normalized). Inset: high-resolution data, showing USMPA peaks at |B|~0.1 mT. These data were measured upon shielding from the earth magnetic field and any stray field. (c) MC(*B*) response in a diode at various bias voltages, V. (d) and (e) Model calculations of MPA_{PP}(*B*) and MC(B) response, respectively, using the 'Δg + HFI' mechanism (see text, Section 4.1.4)

$\Delta g \equiv [g(\text{MEH-PPV}) - g(\text{PCBM})] \approx 3 \times 10^{-3}$; this happens since the P^+ and P^- species are separated in the blend onto two different environments (polymer and fullerene matrices, respectively).

ΔPA spectrum in the blend (Figure 4.4 (a)) is negative, and is assigned to PP transition of both positive and negative polarons. $MPA_{PP}(B)$ response in this case (Figure 4.4 (b) has two components: a low-field component that sharply decreases with *B*, followed by a high-field component that slowly increases with *B*, forming an apparent minimum at $B<\sim10$ mT. For comparison, we also show MC(*B*) response (Figure 4.4 (c) of a photovoltaic device based on the same blend, where again two MC(*B*) components are visible [28]; except that the MC response is opposite in sign compared to that of MPA. The stunning similarity obtained between MPA_{PP} (*B*) and MC(*B*) shows that they share the same underlying mechanism. Because of the finite Δg of the positive and negative polarons in the blend, both MPA_{PP}(B) and MC(B) (Figs. 4.4 (b) and 4.4 (c)) can be accounted for by the PP model that includes the HFI (low-field component) and Δg mechanism (high-field component) as explained in Section 4.1.4. Similar to the irradiated MEH-PPV films (Figure 4.3 (e), a modulated MPA response near $B\sim0$ is also seen in the blend, as shown in Figure 4.4 (b) inset; but it occurs at much lower fields, i.e., $B<0.1$ mT.

4.1.4 Discussion

In the following, we introduce a general model for explaining the magnetic field responses in all three forms of MEH-PPV films. In our previous publications [33, 42, 58, 62], we showed that using a relatively simple model spin-Hamiltonian that includes PP spins subjected to HFI in a magnetic field, all of the important features of MC(*B*) and

MEL(*B*) responses in organic diodes could be explained. Here, we generalize the model to include the 'Δg mechanism', and the effect of TE and TTA on MPA(*B*) and MPL(*B*) responses.

We consider a system that includes N identical species each with spin *S* having overall multiplicity *L*. For a system with a pair of polarons, N=2, *S*=½ and $L=(2S+1)^N=4$; for a single TE, N=1, *S*=1 and *L*=3; and for a pair of TEs , N=2, *S*=1, *L*=9. According to the angular momentum addition rules, the combined pair system is composed of spin multiplets having spin *J*=2*S*, 2*S*-1,..,0. Thus, the PP system is composed of triplet and singlet, respectively; whereas the pair of TEs is composed of quintet, triplet, and singlet, respectively. When the HFI is taken into account, assuming each species *i* interacts with N_i nuclei, each with spin I_{ji} $(j=1,..,N_i)$, the total configuration space is of dimension $M=\Pi_{i=1}^{N}(2S_i+1)\Pi_{j=1}^{N_i}(2I_{ji}+1)$, where $S_i=S$ is the species spin. For example, for a PP system where each polaron of *S*=½ interacts with a single proton *I*=½ nucleus, *M*=16.

Realizing the unique role of species decay in all magnetic field measurements [55, 48, 63], we describe the system by a spin Hamiltonian that includes a non-Hermitian relaxation term [48, 64], H_R,

$$H=H_Z+H_{HF}+H_R\ , \tag{4.1}$$

where H_R describes the decay pathways of the spin multiplet

$$H_R=-i\frac{\hbar}{2}\sum_{\alpha=1}^{L}\kappa_\alpha P^\alpha\ , \tag{4.2}$$

where P^a ($\sum P^\alpha = \tilde{1}$) and κ_α are the relevant spin projection operators and decay rates, respectively. We emphasize that a finite magnetic field response can be obtained only when κ_α are spin-dependent (see Equation (4.5) below). In Equation (4.1) the Zeeman term is $H_Z = \mu_B \sum_{n=1}^{N} g_n \vec{S}_n \cdot \vec{B}$, where the summation is over all species assuming isotropic g-factor; and $H_{HF} = \sum_{i=1}^{N} \sum_{j=1}^{Ni} [S_i \cdot \tilde{A}_{ij} \cdot I_{ji}]$ is the HFI term. We assume for simplicity an isotropic HFI and that each polaron (or TE) interacts with a single nucleus of spin I (= ½), and we ignore the exchange interaction [33]. The time evolution of the density operator is now expressed as [64],

$$\sigma(t) = \exp(-iHt/\hbar)\sigma(0)\exp(iH^\dagger t/\hbar)\,, \tag{4.3}$$

where $H^\dagger$ is the Hermitian conjugate of H (note that $H^\dagger \neq H$), and the t=0 density matrix $\sigma(0)$ is determined by the generation process. The time-dependent probability for the system in the α^{th} spin state may now be written as

$$\rho_\alpha(t) = Tr(P^\alpha \sigma(t)) = \frac{L}{M} \sum_{n,m=1}^{M} P^\alpha_{n,m} \sigma_{m,n}(0) \cos(\omega_{mn} t) \exp(-\gamma_{mn} t)\,, \tag{4.4}$$

where $E_n = \hbar(\omega_n - i\gamma_n)$ (here n=1,…M; and ω_n, γ_n are real quantities) are the complex eigen-values of the non-Hermitian H, and $\omega_{nm} = \omega_n - \omega_m$; $\gamma_{nm} = \gamma_n + \gamma_m$. We emphasize that when the decay rates κ_α are spin-dependent, γ_{nm} in Equation (4.4) are not uniform and the decay of $\rho_\alpha(t)$ becomes spin-dependent; this assures a finite magnetic field effect. The

measured field response (e.g., MPA, MC, etc.) may be readily calculated using Equation (4.4). In any of these processes, the X species undergoes a specific reaction; e.g., $X_0 \rightarrow X_1$ (Figure 4.1) for MPA or dissociation into free polarons in the case of MC. Let R_α be the reaction rate constant, then the total yield of the reaction is

$$\Phi_X = \sum_{\alpha=1}^{L} \int_0^\infty R_\alpha \rho_\alpha(t) dt = \frac{L}{M} \sum_{\alpha=1}^{L} R_\alpha \sum_{n,m=1}^{M} P_{nm}^\alpha \sigma_{mn}(0) \frac{\gamma_{nm}}{\gamma_{nm}^2 + \omega_{nm}^2} . \tag{4.5}$$

Equation (4.5) is a general expression from which any of the magnetic field effects considered above can be calculated via

$$MX(B) = \frac{\Phi_X(B) - \Phi_X(0)}{\Phi_X(0)}, \tag{4.6}$$

where in Equation (4.6), X designates the magnetic field effect: X=PA, PL, C, or EL for MPA, MPL, MC, or MEL, respectively. For example, in the case of PA, assuming that the optical cross section is spin independent, $R_\alpha \equiv R$ in Equation (4.5), and $\Phi_{PA} = R\sum_\alpha \int \rho_\alpha(t) dt = (2RL/M)\sum_n \sigma_{nn}(0)/\gamma_n \propto N_{SS}$. Consequently MPA*(B)=[*N_{SS}*(B)-*N_{SS}*(0)]/*N_{SS}*(0),* i.e., the MPA response is determined by the magnetic field dependent steady state polaron (or TE) population. These populations become magnetic field dependent due to the spin-dependent decay rates κ_α. Likewise, in the case of MC, the reaction rates R_α designate the spin-dependent dissociation rate coefficient d_α, the dissociation yield is $\Phi_d = \Phi_R$ (with $R_\alpha = d_\alpha$ in Equation (4.5)). In each case, the species

involved, as well as the recombination and intersystem crossing pathways, are different, producing a unique response.

In the following, we discuss five different magnetic field processes and compare the model with the obtained experimental results.

(a) **MPA due to TE mechanism**. In pristine MEH-PPV films at low I_L (Figure 4.2 (b), I_L=10 mW), the photoexcited TE density is low, and this leads to very low density of TE pairs. Consequently, the TE density in this case is determined by a recombination process in which the spin sublevel recombination constants κ_α (α=±1,0) are different from each other. The principal TE zero-field splitting (ZFS) parameters, were obtained in MEH-PPV by the PA-detected magnetic resonance technique; they are $D/g\mu_B \approx 63$ mT and $E/g\mu_B \approx 9$mT [65]. Using these ZFS parameters, we calculated the energy levels and wavefunctions of a TE in a magnetic field applied in a general direction. We further calculated the powder pattern of $MPA_T(B)$ as shown in Figure 4.2 (d) (TE) for $\kappa_1=\kappa_{-1}= 0.25\kappa_0=1.3\text{x}10^7 s^{-1}$. We note that: (a) this model also explains MPL(*B*), because TE-SE scattering that controls the exciton PL intensity (Figure 4.1), is directly proportional to the TE density; and (b) this mechanism is unique in that it involves just one type of photoexcitation (as opposed to PP or pair of TE), which has not been considered before. The spin selectivity here arises from the spin-dependent decay constants κ_α.

(b) **MPA due to TTA mechanism**. When pristine MEH-PPV films are subjected to high laser excitation intensity (Figure 4.2 (b), I_L=400 mW), the TE density is sufficiently high that the TTA process becomes dominant. Consequently, triplet

N_{SS} is determined by the individual decay rates of the TE-TE collision byproducts, namely quintet, triplet, and singlet states [55]. First, we calculated the energy levels and wavefunctions of a pair of randomly oriented TEs in a magnetic field of a general direction. Subsequently, using Equation (4.5), the powder pattern response $MPA_{TTA}(B)$ was calculated as shown in Figure 4.2 (d) (TTA) for $\kappa_Q=\kappa_T=\kappa_S/30=10^6 s^{-1}$.

(c) **MPA due to PP mechanism**. In UV irradiated MEH-PPV films, the PA is dominated by polarons, and thus, MPA originates from photogenerated PP species (Figure 4.3 (b)). The calculated $MPA_{PP}(B)$ response using the PP mechanism governed by the HFI is shown in Figure 4.3 (d). For the calculation, we used PP(triplet) to PP(singlet) recombination ratio, $\kappa_T/\kappa_S=0.96$ and isotropic HFI $a/g\mu_B$=3mT.

In the MEH-PPV/PCBM blend, the photoexcited positive and negative polarons have different g-factors [61]. Using the same parameters as above, and $\Delta g=3x10^{-3}$ (Ref [64]) we calculated the $MPA_{PP}(B)$ response as shown in Figure 4.4 (d).

(d) **USMPA.** Some of the photoinduced PP dissociate to free polarons; thus, the free polaron density becomes *B*-dependent, leading to free-polaron PA(*B*). As was have shown previously [33] (and can also be calculated directly from Equation (4.5)), the dissociated polaron density shows ultra-small magnetic field effect in agreement Figure 4.3 (e).

(e) **MC.** In Figure 4.3 (d) and Figure 4.4 (e), respectively, we show MC(*B*) response calculated using Equation (4.5) (assuming PP dissociation into free polarons)

with: (i) HFI: $a/g\mu_B$=3mT and Δg=0, and (ii) same HFI with varying Δg, for the same parameters as in (c) above.

In all of these cases, the agreement between the experimental data and calculated responses is a strong indication that the models used capture the main features of the experimental findings. Our model is very general, and may be applicable also when the exchange interaction, spin orbit coupling, and a diffusion process are included. Our work shows that all specific forms of the organic magnetic field effect are based on the *same principles*, namely magnetic field manipulation of the spin density of the excited species, regardless of whether they are formed via photon absorption (MPA and MPL in films) or carrier injection (MC and MEL in devices).

4.1.5 Conclusion

We have introduced a novel 'spectroscopic-sensitive' magnetic field effect technique which spectrally resolve photo-induced absorption and photoluminescence in π-conjugated polymer *films* and apply it to study a number of spin-dependent processes. By directly comparing the new MPA and MPL responses in films to those of MC and MEL in organic diodes based on the same organic active layer, we are able to relate the magnetic field effect in organic diodes to the spin *densities* of the excitations formed in the device, regardless of whether they are formed by photon absorption or carrier injection from the electrodes. We deduced the main spin-dependent species and/or spin-mixing mechanism that determine the MPA (MPL) response in three different forms of a π-conjugated polymer, namely MEH-PPV. These include spin-mixing in PP species, triplet-triplet annihilation, spin-mixing among the triplet spin sublevel, and *Δg*

mechanism of PP in polymer/fullerene blends. We have introduced an all-purpose quantum mechanical model which is able to explain the obtained magnetic field response in the MEH-PPV system. This model is viable for both MPA response obtained in films as well as for MC and MEL responses obtained in devices made of the same organic interlayer as in the films. Applying this model to our results, we show that the magnetic field-dependent excitation density may account for all field responses measured in the MEH-PPV system, including MPA, MPL, MC, and MEL.

4.2 Magnetic Field Effect Spectroscopy of C_{60}-Based Films and Devices

4.2.1 Introduction

The magnetic field effect (MFE), e.g., magnetoresistance in low mobility organic semiconductor devices, has been interpreted as due to spin sensitive processes among pairs of spin bearing excitations [19, 21, 24, 27, 66, 67]. In many organic semiconductors that contain carbon and hydrogen atoms but lack heavy atoms, the major spin mixing mechanism has been shown [33, 68] to be the hyperfine interaction (HFI) between the protons (nuclear spin I_H=½, nuclear g-factor g_H=5.585) and the polaron electronic spin (S=½, g-factor ≈2.00), with typical HFI coupling constant, a_H≈0.3 μeV (Ref. [69]). In contrast, the buckeyball C_{60} molecule is composed of 60 carbon atoms, of which 98.9% are the natural abundant ^{12}C isotope having spinless nucleus, and thus zero HFI; and ~1.1% ^{13}C isotope (I_{C13}=½, g_{C13}=1.405) with estimated HFI constant a_{C13}≈0.1 μeV (Ref[69]). Therefore, the HFI constant averaged over the 60 carbon atoms of natural C_{60} molecule should be a_{C60}≈1 neV (or $a_{C60}/g\mu_B$≈10 μT), which is too small to play any

significant role in the MFE, especially not in magneto-transport. Consequently, spin sensitive mechanisms other than the HFI become important for the MFE in fullerene films and devices. These mechanisms may involve [31] radical pairs, or equivalently polaron pairs (PP); or triplet excitons (TE). Among the spin-½ PP mixing mechanisms we mention: (i) the Δg mechanism [70] that originates from the difference, Δg in the g-factor between negative (P^-) and positive (P^+) polarons; (ii) the $P^{-}P^{+}$ spin exchange mechanism that causes a singlet-triplet level crossing at a finite magnetic field, B_{LC} whose magnitude is directly related to the strength of the exchange interaction [71]; (iii) the spin-orbit interaction associated with hybridized carbon wave functions. In addition the TE-related mechanisms include TE that undergo triplet-triplet annihilation [55]; or spin sublevel sensitive recombination which affects the magnetic field dependence of TE-polaron collision [68] as well as the TE density [72]

In this work, we explored the MFE spectroscopy at steady state conditions such as magneto-photoinduced absorption (MPA) and magneto-photoluminescence (MPL) in both annealed and pristine C_{60} thin films; as well as magneto-conductance (MC) in diodes based on C_{60} interlayer. We found that C_{60} films show substantive MFE in spite of their miniature HFI strength. Specifically, we found that the MFE(*B*) response is composed of a narrow (~10 mT) and broad (>100 mT) components, whose relative magnitude depends on the pump excitation intensity for MPA in films, or current density (determined by the bias voltage) for MC in devices. We show that the narrow MFE(*B*) component that dominates the MPA at low excitation intensity and MC at small voltage, originates from spin-dependent recombination of the TE in C_{60}. In this case, the MFE(*B*) width is of the order of the TE zero field splitting (ZFS) parameters [73], *D* and *E*. The

ZFS parameters for the TE in C_{60} films were estimated [74] to be rather small: D=1.4 μeV ($D/g\mu_B$=12 mT) and E~0; and this explains the MFE(B) narrow width. The broad MFE(B) component, however, which is the main response at high pump intensities for MPA or large voltage for MC, is attributed to the '□g mechanism' of PP [31] influenced by the finite pair lifetime.

4.2.2 Experimental

For the MC investigations, we fabricated organic diodes with 5 mm^2 area based on C_{60} interlayer with film thickness of order 100 nm, but without the traditional hole transport layer. For comparison, we also fabricated similar devices based on ^{13}C isotope-rich C_{60} which possesses ~25 times larger HFI than natural C_{60} films (having only 1.1% ^{13}C). The organic diode was composed of an indium tin oxide [ITO] anode, and a thin calcium cathode capped with an aluminum overlayer for protection; the device structure was thus ITO/C_{60}/Ca/Al. The C_{60}-based diodes were transferred to a cryostat with variable temperature control that was placed in between the pole pieces of an electromagnet that produced magnetic field, B up to 250 mT (with 0.01 mT resolution); or to another electromagnet for B up to 1 T (with ~1 mT resolution). In all cases, the field strength B was determined by a calibrated magnetometer. The devices were driven at constant voltage, V using a Keithley 236 apparatus; and the current, I, was measured while sweeping B. MC is defined by the relation MC(B)=[I(B)-I(0)]/I(0). Two kinds of C_{60}-based devices were studied, where the evaporated fullerene interlayer film was either annealed or used in its pristine form ('as is').

The MPA method is same as described in Section 4.1.1; here, we briefly summarize it for completion. Steady state photomodulation (PM) is a 'pump-probe' technique using continuous wave (cw) light sources, of which spectrum usually contains few photoinduced absorption (PA) bands that belong to various long-lived photoexcitations. For the 'pump' we used a cw Ar^+ laser with above-gap photon energy; whereas the 'probe' was derived from an incandescent tungsten lamp and a monochromator. The PM spectrum was measured from C_{60} films that were evaporated on sapphire substrates at room temperature. PA is defined as the negative fractional change in transmission, T: $PA(E)=(-\Delta T/T)=N_{SS}d\beta$ (E), where N_{SS} is the species *steady state density*, d is the film thickness and β (E) is the excited state absorption optical cross-section at the probe photon energy, E. The steady state PM spectrum of C_{60} is known [74, 75] to be composed of optical transitions between low energy (X_0) and high energy (X_1) excited states that belong either to the S=1 triplet exciton (TE) manifold or S=½ charge polaron manifold. Upon the application of a magnetic field, PA(B) response is determined by the steady state photoexcitation density $N_{SS}(B)$, which in turn is controlled by the decay rate coefficient, $\kappa(B)$. For $B\neq0$, the X_0 level splits according to the relevant spin multiplicity, L; L=3 for S=1 TE, or L=4 for PP species composed of two S=½ polarons. Consequently, through specific spin-mixing processes at field B, the spin content of each sublevel, its decay rate κ, N_{SS} and thus PA, all become B-dependent forming a magneto-PA response defined as: $MPA(B)\equiv[PA(B)-PA(0)]/PA(0)$.

The C_{60} powder was purchased from American Dye Source. The chemical structure of C60 is shown in inset of Figure 4.5 (b). C_{60} powder was thermally evaporated to produce thin films using a slow evaporation rate of about 0.5 A^o/s. Two kinds of

evaporated films were studied here, namely ‘annealed’ and ‘pristine’. The ‘pristine’ films were used as deposited, whereas the ‘annealed’ films were put in an oven at 200°C for ~1 hour. For the PM measurements, we evaporated 100 nm of C_{60} on sapphire substrates. The morphology of the C_{60} films was studied by X-ray diffraction (XRD) and Transmission Electron Microscopy (TEM) at room temperature. For the XRD measurements, a 200 nm thick C_{60} film was grown on a glass substrate (2.5mm X 2.5mm area). The XRD pattern was obtained using a Philips powder diffractometer equipped with CuK_{α} source at 45 kV & 40 mA. We used the grazing incidence method that is appropriate for measuring XRD pattern from thin films. For the TEM measurements and analysis, a 100 nm thick C_{60} film was grown on a thin copper grid, and the ‘ImageJ’ software was used to analyze the TEM images.

4.2.3 Experimental Results

The XRD patterns and TEM pictures of the different C_{60} films are shown in Figure 4.5. Figures 4.5 (c) and 4.5 (d) are the TEM images of the respective annealed and pristine C_{60} films. The TEM image clearly shows the formation of domains having higher C_{60} density than that of the surrounding matrix, which we identify as nano-crystalline grains. From the size distribution histogram of the pristine film obtained from the TEM image (Figure 4.5 (f)), we estimate an average grain size, D_g ~25 nm. We found, however that the grain number density *increases* in the ‘annealed’ film, and the grain size substantially decreases (Figure 4.5 (e)). This is in agreement with the following XRD data.

Figure 4.5 (a) shows the grazing incidence XRD patterns from an annealed and

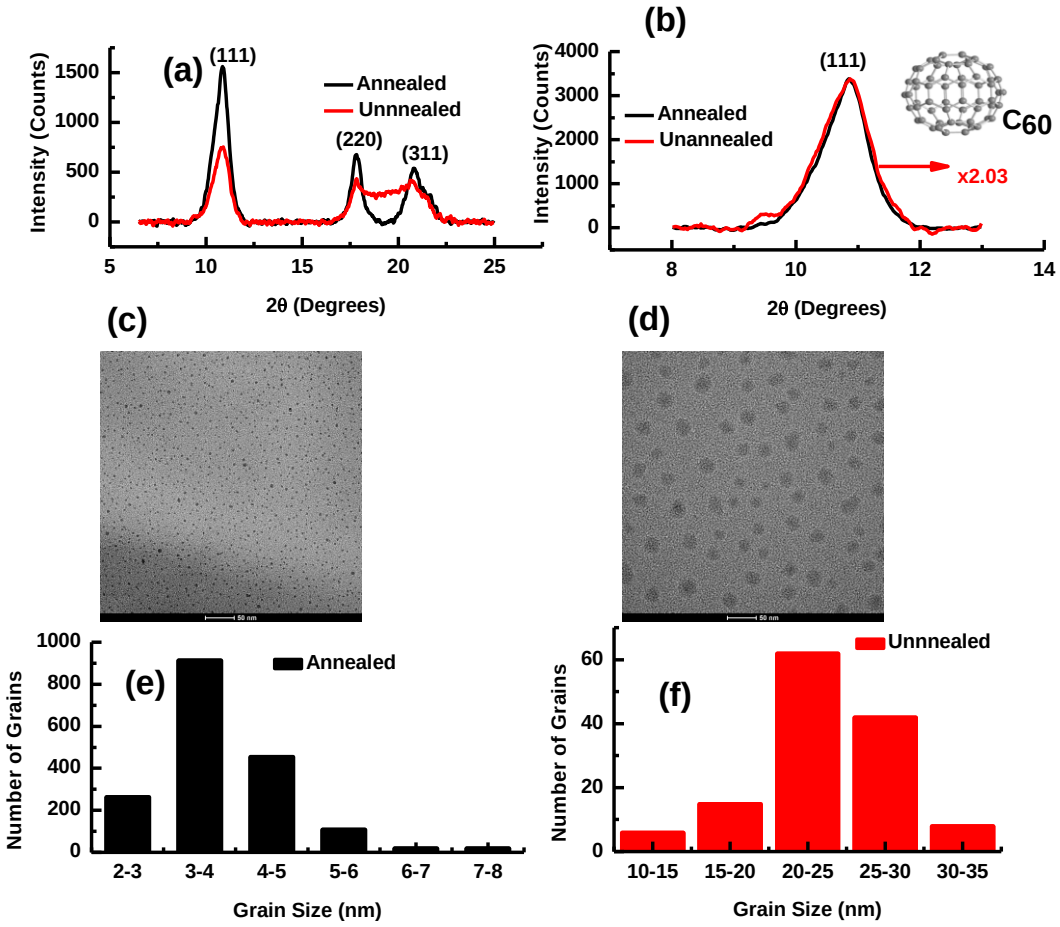

Figure 4.5 The X-ray diffraction pattern of annealed and pristine C_{60} films in the range (a) $2\theta = 6\text{-}25^0$, (b) $2\theta = 8\text{-}13^0$; the miller indices are denoted on the Bragg scattering bands. The inset in (b) shows the chemical structure of C_{60}. TEM images of annealed (c) and pristine (d) C_{60} films; the grey grains are C_{60} microcrystallites. The scale bar is 50 nm. Also shown are the grain size distributions extracted from the TEM images for the annealed (e) and pristine (f) C_{60} films.

pristine C_{60} films using the CuK_{α} X-ray line at λ=0.154 nm. Three Bragg scattering bands are clearly seen. C_{60} is known to crystallize in a fcc Bravais lattice (BL) structure, with lattice constant, a~1.42 nm [76]; we therefore assigned the obtained Bragg scattering band at 2θ=10.8° to the (111) line, whereas the other two bands at larger 2θ are identified as (220) and (311). We note that the scattering strength of the (111) band is higher in the annealed film compared to the pristine film; but their width in the two films is similar. We estimated the average nano-crystalline grain size, D_g ~10 nm from the full width at half maximum (FWHM), $\Delta_{2\theta}$ of the (111) Bragg band, using the Scherrer relation. This is much smaller than D_g extracted from the TEM image of the pristine film, and therefore the Bragg scattering width is determined by other factors, such as coherence length, for example. In agreement with this assumption, we found that the 'coherence length' of the grains is not affected by the annealing process, since the FWHM of the (111) band is robust (Figure 4.5 (b)). Interestingly, the total 'scattering intensity', defined as the area under the three Bragg bands, remained roughly unchanged upon annealing (Figure 4.5 (a)), consistent with the unchanged number of scattering particles (atoms) in the grains.

In Figure 4.6 (a), we show the PM spectrum of an annealed C_{60} film at B=0 (black line) using a laser excitation intensity I_L=0.2 W/cm^2 at 50K. The PM spectrum consists of two broad PA bands, E_1 and E_2 that are centered at E~1.1 eV and ~1.8 eV, respectively, and a low energy shoulder at E~0.8 eV. We speculate that the E_1 and E_2 bands consist of overlapping triplet bands (at ~1.1 and ~1.8 eV, respectively) and polaron bands (at ~1 and ~1.9 eV, respectively) that were in fact separated before using the technique of PA-detected magnetic resonance, PADMR [74]. In addition, the PM spectrum of the pristine C_{60} film, shown in Figure 4.6 (b) (black line), is very similar to that of the annealed C_{60},

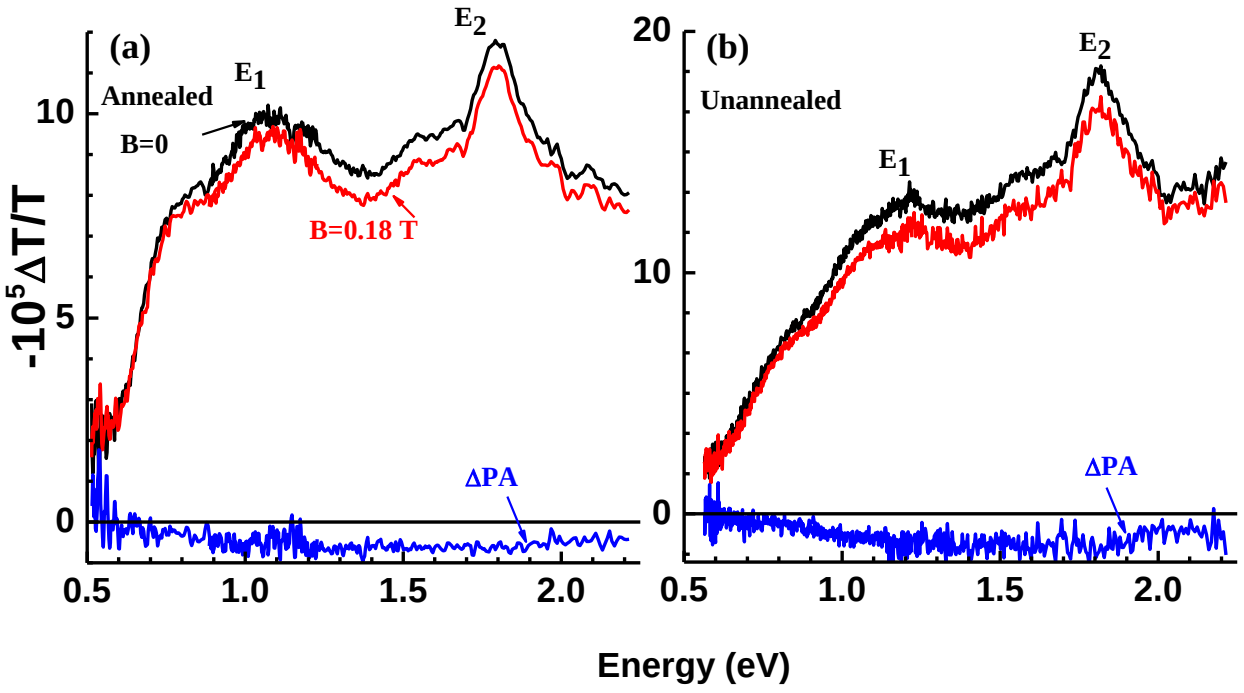

Figure 4.6. Photomodulation spectra of annealed (a) and pristine (b) C_{60} films at T=50 K and I_L=0.2W/cm^2 for *B*=0 (black lines) and *B*=180 mT (red lines). The blue negative lines are the difference spectra ΔPA=PA(*B*=180 mT)-PA(0)

except that the PA bands are broader. The red lines in Figures 4.6 (a) and 4.6 (b) show the PA spectrum at *B*=180 mT. At these I_L and *B* values, the difference spectrum, $\Delta PA(B_1,B_2,E)=PA(B_2,E)-PA(B_1,E)$, where B_2=180 mT and B_1=0, is negative, as shown in Figures 4.6(a) and 4.6(b) (blue line). However, $\Delta PA(E)$ is very sensitive to B_2, B_1, and I_L, as shown below. In Figure 4.7 (a), the magnetic field response, MPA(*B*)≡$\Delta PA/PA$ of the annealed C_{60} film measured at E=1.8 eV is shown for various excitations, I_L. At small I_L,

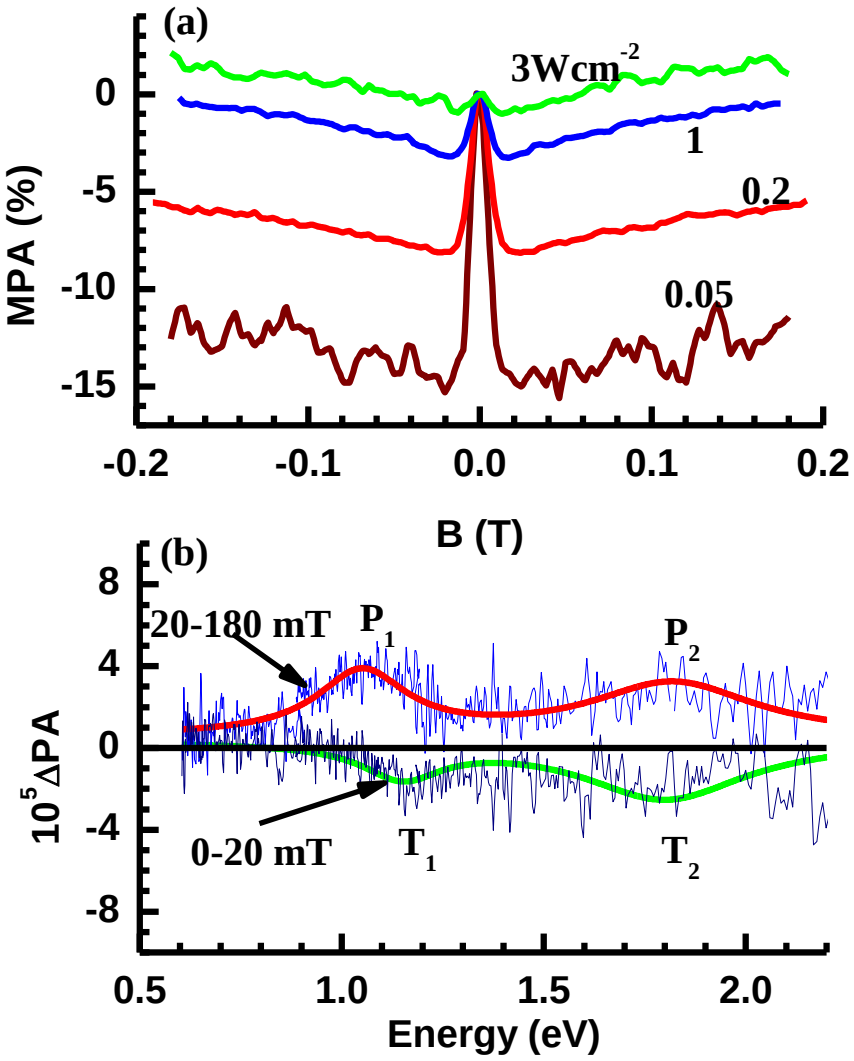

Figure 4.7. MPA and ΔPA response (a) MPA(*B*) response of an annealed C_{60} film at various pump excitation intensities, measured at photon energy E=1.8 eV and T=50 K. (b) The spectra $\Delta PA(B_1,B_2,E)$ for B_1=0, B_2=20 mT (black line, lower curves), and B_1=20 mT, B_2=180 mT (blue line, upper curves) for I_L=1.5 W/cm^2. The smooth green and red lines through the data are to guide the eye, and show the TE- and polaron-related MPA bands, respectively.

MPA(*B*) is dominated by a relatively narrow negative component with full width at half maximum (FWHM) ~12 mT. At higher fields, another MPA component may be resolved. This MPA component is much broader, and increases monotonically with *B* up to *B*=0.2 T, which is the highest field employed here. Also, as I_L increases, the narrow component decreases from ~16% at 0.05 W/cm^2 to less than 1% at 3 W/cm^2, whereas the broader component remains nearly unchanged. We thus conclude that MPA(*B*) is dominated by two different spin-mixing mechanisms, perhaps related with two different photoexcitation species: one mechanism is responsible for the narrow component that decreases at large I_L; and the other mechanism that is characterized by a much broader MPA(*B*) response, is nearly insensitive to changes in I_L.

In order to further study the two MPA components, we show in Figure 4.7 (b) the MPA spectra of an annealed C_{60} film at laser excitation intensity I_L=1.5 W/cm^2, namely $\Delta PA(B_1,B_2,E)$ for two cases: (i) B_1=0, B_2=20 mT (negative MPA spectrum), which is sensitive mainly to the narrow MPA component; and (ii) B_1=20 mT, B_2=180 mT (positive MPA spectrum), which unravels the broad MPA component. The two MPA spectra manifest important differences: (a) The low-energy MPA band in case (i) (T_1 at ~1.15 eV) is higher in energy than the low-energy MPA band in case (ii) (P_1 at ~1.05 eV); (b) T_1 is weaker than T_2 in case (i), whereas P_1 is stronger than P_2 in case (ii). The two sets of MPA bands are in agreement with the two sets of PA bands obtained in PA vs. modulation frequency and PADMR spectra measured by Dick et al. [74], who identified the two PA spectra sets as due to polarons (P_1 and P_2) and triplet excitons (T_1 and T_2), respectively. Consequently, based on the agreement between the previous PADMR and

MPA spectra, here we assign the narrow MPA component as due to TE, whereas the broad MPA component originates from PP species.

This interpretation is strengthened when the PM and MPA spectra in the annealed and pristine films are compared (Figures 4.6 (a) and 4.6 (b)). The low energy PA shoulder in the pristine film is weaker at E< 0.8 eV than that in the annealed film. Since this energy region is dominated by the polaron P_1 band, we conclude that the polaron photogeneration efficiency is enhanced upon annealing. As shown in the X-ray and TEM data of the annealed and pristine films (Figure 4.5), there are more microcrystalline grains in the annealed film, and this may facilitate polaron photogeneration at the grain boundaries. Indeed, we found that the broad MPA component that is related with photogenerated polarons is weaker in the pristine film (not shown here), in agreement with the weaker PA shoulder at low energy.

In Figures 4.8 (a) and 4.8 (b), the MC(*B*) response of an annealed C_{60} diode is shown for various voltages. Similar as for the MPA(*B*) response of C_{60} films, the MC(*B*) diode response is also composed of a narrow and broad components of which relative magnitude changes with the applied bias voltage, V_b (or alternatively, current density). The narrow component dominates the response at V_b up to ~1.5 V (Figure 4.8 (a)), and decreases with increasing V_b; whereas the broad component increases with V_b, and at high voltages (V_b>2 V Figure 4.8 (a)) it completely dominates the MC(*B*) response. This broad MC component further increases with *B* up to at least *B*=1 T (Figure 4.8 (b)); thus, it does not saturate up to the highest field employed here. We therefore conclude that the same two mechanisms which dominate the MPA(*B*) response in films are also responsible for the MCB) response in the diodes. The relative contribution of each

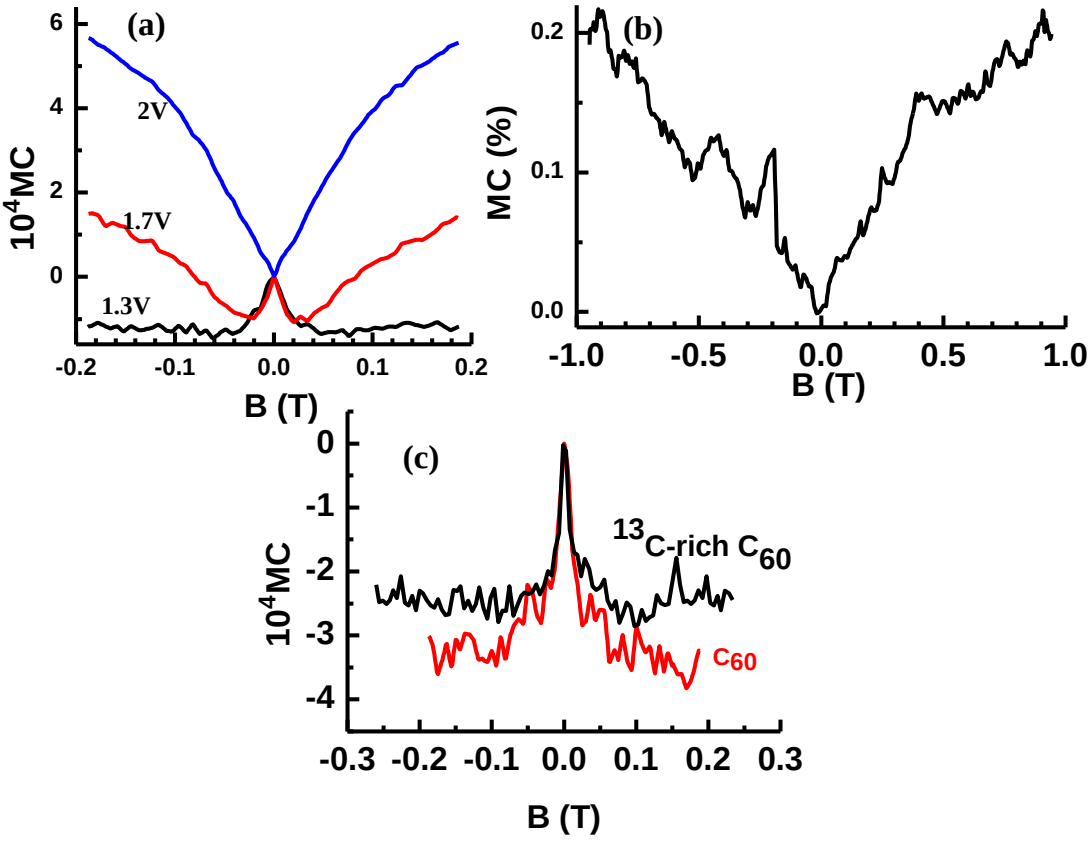

Figure 4.8. MC(*B*) response of an annealed C_{60} diode for various bias voltages measured at T=10 K. (a) high resolution for |B|<0.2 T; (b) low resolution for |B|<1 T. (c) MC(*B*) response of devices based on ^{13}C-rich C_{60} (black line) compared with that of devices based on regular C_{60} (red line) for |B|<40 mT.

mechanism responsible for the two MC components varies with the bias voltage and also with the film morphology.

The HFI plays a very important role in both MPA and MC responses in organic films and devices, respectively [33, 42, 72]. However, as pointed out above, naturally abundant C_{60} contains only 1.1% of the nuclear spin bearing ^{13}C isotope. Therefore, in order to examine the role of the HFI on the MC response of C_{60} diodes, we measured the

MC(*B*) response of a device made of ^{13}C-rich (~25%) C_{60} interlayer; this is shown in Figure 4.8 (c). It is seen that the narrow MC component has the same width as in the naturally abundant C_{60} device. We thus conclude that the narrow MC component in naturally abundant C_{60} cannot originate from a spin-mixing process controlled by the HFI. In addition, since the HFI constant of ^{13}C is of order ~1 mT (Ref. [69]), the unsaturated broad component also does not originate from the HFI.

We also studied the MPL response in C_{60} films. The PL spectrum at 50 K is shown in Figure 4.9 (a); it was interpreted as due to radiative transitions of singlet excitons in C_{60}. The PL emission spectrum is composed of a 0-0 line at 1.7 eV, followed by two phonon replica ~180 meV apart, which is the frequency of the C=C stretching vibration in C_{60}. However, since the singlet excitons in C_{60} are practically nonluminescent, the PL is very weak. To increase the system sensitivity, we consequently measured the MPL(*B*) response of the entire PL band (Figure 4.9 (b)). We note that the MPL(*B*) response is also composed of narrow and broad components, typical of the MFE(*B*) in C_{60}; however, the narrow MPL(*B*) component is not easily discerned here.

4.2.4 Discussion

The MFE(*B*) response in C_{60} including MPA, MPL, and MC is characterized by a narrow, Lorentzian like, negative component having FWHM~12 mT (Figures 4.7 (a), 4.8(a) and 4.9 (b)) that saturates at *B*~20 mT (denoted hereafter MFE_N), and a broad component that increases with *B* with no visible saturation up to *B*~1 T (denoted hereafter MFE_W). The obtained FWHM of the $MFE_N(B)$ component is close to the ZFS parameter, $D/g\mu_B$ for TE in C_{60} [77, 78]. Also, from the MPA spectroscopy, we infer that the MFE_N

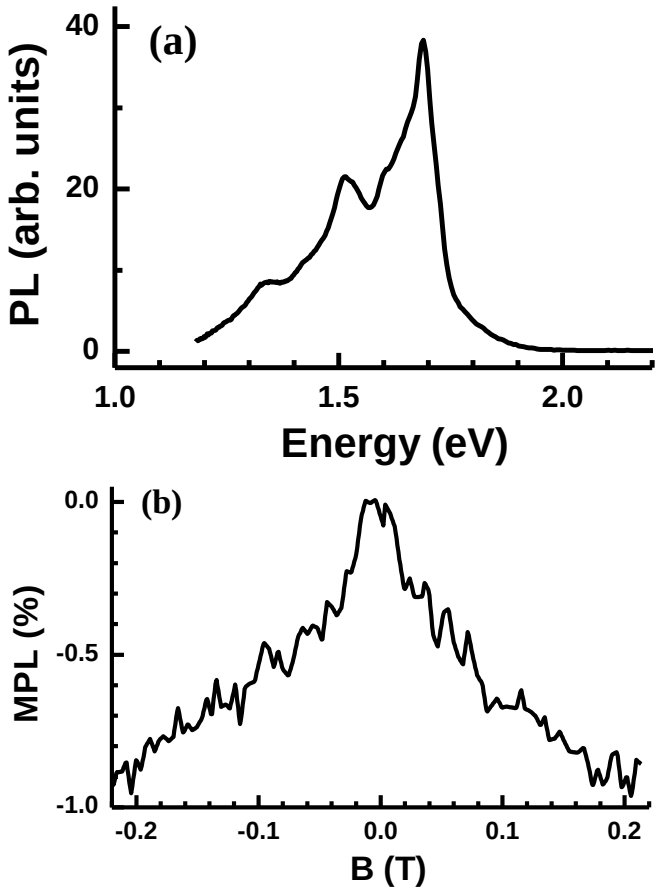

Figure 4.9. PL spectrum (a) and MPL(*B*) response (b) of annealed C_{60} film at T=50 K.

component is indeed related to TE in the C_{60} film. It is thus tempting to interpret the MFE_N component as due to spin-mixing mechanism that involves TE in C_{60}. In contrast, spin-mixing mechanisms such as the HFI, spin-orbit coupling, or scattering mechanisms related to TE are too weak in C_{60} to account for the unsaturated MFE_W component. Also, from our MPA spectroscopy, we conclude that this component is related with charge polarons in the C_{60} film. We therefore propose that the MFE_W component originates from the minute difference of the g-factor between the coupled positive and negative polarons in C_{60}; the so called "Δg mechanism" [70]. In the following, we discuss the appropriate

model for the two MPA(*B*) response components, and conclude that the same mechanisms are also responsible for the MC(*B*) and MPL(*B*) responses.

4.2.4.1 Magneto-photoinduced Absorption: Narrow Component

For the MPA_N component, we envision a mechanism that involves TE as follows. PA is proportional to the steady state photoexcitation density, N_{SS}. At *B*=0, the TE lowest energy state, X_0 is split according to the values of the ZFS energies *D* and *E*. At large *B*, the three TE spin sublevels are dominated by the Zeeman interaction, $g\mu_B Bm$, where m=0,±1. Therefore, as *B* increases from zero, the $S_z=m\hbar$ character of each spin sublevel varies, since the Zeeman interaction becomes increasingly stronger with *B* compared to the dipolar interaction that leads to ZFS. Our main assumption here is that X_0 decay rate depends on the spin sublevel character, m [70], which depend on B; with decay rates, $\kappa_+ \approx \kappa_- < \kappa_0$ for m=1,-1 and 0, respectively. Consequently, as *B* increases, the steady state TE density varies because the S_z content of each sublevel changes with *B*.

The general form of a TE Hamiltonian at *B*=0 is written as [73] $H_T = \vec{S} \cdot \tilde{\tau} \cdot \vec{S}$, where S=1, and the triplet tensor $\tilde{\tau}$ is a symmetric traceless tensor of rank 2. In the triplet principal reference frame, $\tilde{\tau}$ diagonal elements are given by the ZFS parameters *D* and *E*. In the laboratory reference frame in which the magnetic field **B**||z makes polar angles (θ, φ) with the principal reference frame, the five independent elements of $\tilde{\tau}$ become angle dependent [79].

In a magnetic field *B*, the spin Hamiltonian reads $H_0 = H_T + H_Z$, where $H_Z=g\mu_B B S_z$ is the Zeeman term. The decay process, however, is not contained in the spin

Hamiltonian, H_0, because the latter is a Hermitian operator that conserves energy. A convenient way to include the spin dependent decay kinetics is to add to H_0 a non-Hermitian decay (relaxation) term [48, 64]: $H_R = -\frac{i\hbar}{2}\sum_{\alpha=1}^{3}\kappa_\alpha P^\alpha$, where P^α ($\sum P^\alpha = \tilde{1}$) is the triplet sublevel projection operator, and κ_α is the spin sublevel decay rate. Consequently, the total Hamiltonian is written as:

$$H = \vec{S}\cdot\tilde{\tau}\cdot\vec{S} + g\mu_B B S_z - \frac{i\hbar}{2}\sum_{\alpha=1}^{3}\kappa_\alpha P^\alpha \tag{4.7}$$

We note that H is non-Hermitian having complex eigen-values, $E_n = \hbar(\omega_n - i\gamma_n)$ ($\gamma_n \geq 0$, n=1,2,3). Obviously, both ω_n and γ_n are magnetic field-dependent. $\gamma_n(B)$ in Equation (4.7) represents the decay rate of spin sublevel n in a magnetic field B. The TE steady state density, N_{SS} becomes magnetic field dependent via the relation $N_{SS}(B) = \sum g_n / \gamma_n$, where g_n is the generation rate into level n. Since PA ~ N_{SS}, it too becomes B-dependent. Assuming uniform B independent photogeneration rates, we can calculate MPA(B) as

$$MPA(B) = <[\sum \gamma_n^{-1}(B) / \sum \gamma_n^{-1}(0)] - 1>, \tag{4.8}$$

where the bracket <…> denotes angle averaging ("powder pattern") in the disordered film. In Figure 4.10 (a), we show an example of fitting the calculated MPA(B) (blue line) to the experimental MPA(B) response (taken from Figure 4.6 (a), black line). A good fit

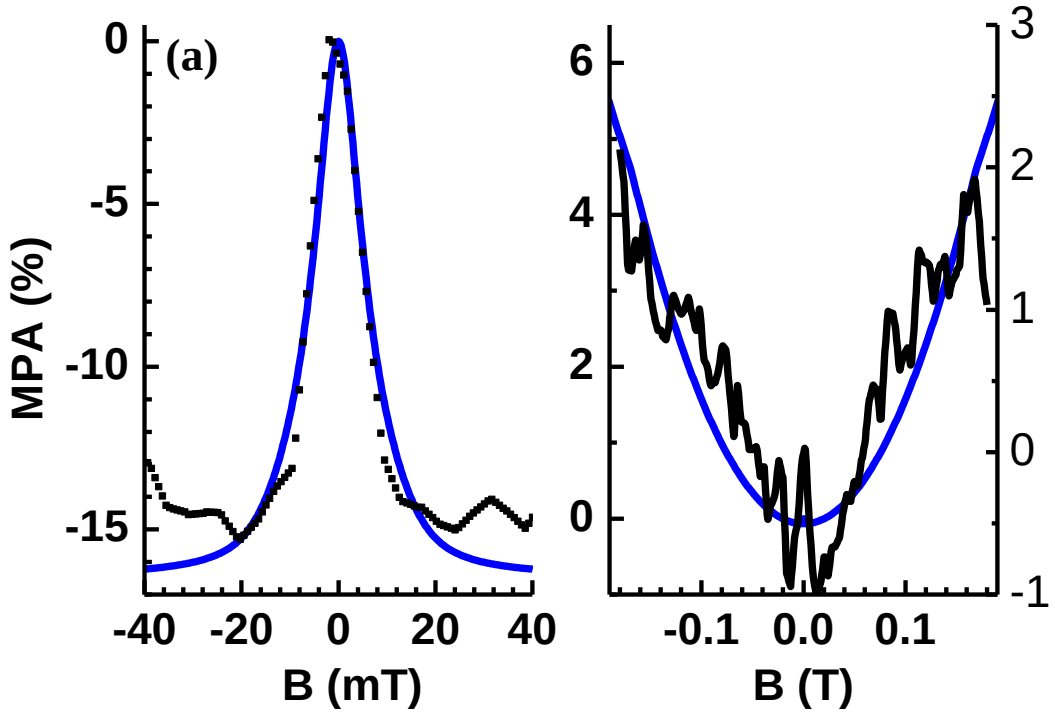

Figure 4.10. Model fitting for MPA(*B*) of C_{60}. (a) Low field, |B|<40 mT. The blue line is calculated based on the TE mechanism (see text); the black points are measured MPA(*B*) taken from Figure 4.7 (a). (b) Intermediate field, |B|<0.2 T. Blue line: calculated using the 'Δg mechanism' (see text); black line: measured MPA(*B*), respectively.

between the calculated and experimental PA(*B*) responses is obtained using *D*=2.3 μeV (or $D/g\mu_B$=20 mT), *E*~0 and the decay rates $\kappa_{\pm 1} = 0.35\kappa_0 = 3 \cdot 10^6 s^{-1}$. *D* obtained from the fit is in reasonable agreement with the triplet exciton ZFS parameter $D/g\mu_B$ obtained in C_{60} from PADMR [77, 78] (~ 12 mT).

4.2.4.2 Magneto-photoinduced Absorption; Δg Mechanism

In addition to the TE bands, the PM spectrum of C_{60} films also contains two polaron PA bands at E~1 eV (within the E_1 band in Figure 4.6) and E=1.9 eV (Ref. [74,

75], within the E_2 band in Figure 4.6). The g-factor was obtained from light-induced electron spin resonance and doping measurements. It was concluded that the g-factor for the negatively charged C_{60}^- polaron is g_1=1.9992 (Ref. [80, 81]), whereas that of the positively charged polaron is g_2~2.0021 (Ref. [82]). Therefore, when P^+ and P^- form a loosely bound PP, they may contribute to the MPA(*B*) response by spin-mixing via the 'Δg mechanism'; the other potential spin-mixing mechanisms such as the HFI, SOC and exchange interaction are all negligibly small in C_{60}. The PP may be formed in singlet, PP_S, or triplet, PP_T spin configuration. Because of the difference, Δg, the P^+ and P^- spin precession frequencies in *B* are different; as a result, the spin states PP_S and PP_{T0} interconvert [71, 83]. The Δg mechanism is especially effective in C_{60} because of the weak HFI. Consequently, the $PP_S \leftrightarrow PP_T$ interconversion increases with *B*; and this, in turn causes a monotonic increase in the MFE(*B*) response.

The Hamiltonian for the PP spin sublevels is now written as the sum of two different Zeeman terms, and a decay term:

$$H_{PP} = g_1\mu_B S_1 B + g_2\mu_B S_2 B - \frac{i\hbar}{2}\sum \kappa_\alpha P^\alpha \qquad (4.9)$$

where S_1, S_2 are the P^+ and P^- spin =½ operators, α designates either singlet (S) or triplet (T) state, and P^α and κ_α are the state projection operator and decay rate, respectively. Following the same procedure as in Section 4.2.4.1, the MPA(*B*) response is given by Equation (4.8); where angle averaging is not needed here. In Figure 4.10 (b), we show an example of a good fit between the calculated MPA(*B*) compared with the experimental MPA(*B*) response for the broad component, MFE_W (taken from Figure 4.6 (a)). The

calculation was obtained using $\Delta g=7.5\cdot10^{-4}$ and $\kappa_T = 0.8\kappa_S = 2\cdot10^6 s^{-1}$; both values are reasonable for the PP species in C_{60} films.

4.2.4.3 Magnetoconductance and Magneto-photoluminescence

Similar to the MPA(*B*) response, the MC(*B*) and MPL(*B*) responses also show narrow and broad components that originate from the TE and Δg mechanisms, respectively. We argue that polaron-triplet collisions, where the steady-state TE density is governed by the MPA(*B*) narrow response, give rise to the MC(*B*) narrow component. Similarly, the MPL narrow component can be explained by the TE model outlined above, since the PL is affected by the nonradiative decay channel of singlet excitons collisions with TE, of which density varies with *B*. Furthermore, collisions of the singlet excitons with PP's may explain the broad MPL(*B*) component that originates from the 'Δg mechanism' that affects the PP density. Dissociation of PP give rise to MC(*B*) [33, 72, 79] thus the PP 'Δg mechanism' yields may form the broad MC(*B*) component similar to that in MPA(*B*). The detailed interplay between the TE and Δg mechanisms may be different in the MPA and MC or MPL processes; therefore, the line shapes of the latter MFE(*B*) responses show similar characteristics, but they are not necessarily identical to that of MPA(*B*).

4.2.5 Conclusion

In this work, we studied various MFE's in annealed and pristine C_{60} films and C_{60}-based diodes. We found that C_{60} films and devices show substantial MFE in spite of the negligibly small HFI. We show that the MFE(*B*) response contains a narrow

(FWHM~12 mT) and broad components that originate from TE and PP species, respectively. We demonstrated that the steady state density of TE and PP excitations at field *B* can explain not only the MPA(*B*) response in films, which is directly proportional to N_{SS}, but also the MC(*B*) response in diodes, and MPL(*B*) response in films. We introduced a spin-dependent recombination mechanism to explain the narrow MFE component based on TE, and calculated the broad MFE component based on the 'Δg mechanism'. The latter mechanism gives rise to an unsaturated increasing MPA(*B*) and MC(*B*) responses and decreasing MPL(*B*) response up to at least ~1 T. Our results show that the MFE in the organics has a much broader scope than that thought before based on the HFI alone.

CHAPTER 5

ORGANIC PHOTOVOLTAIC DEVICES

5.1 Efficiency Enhancement in Organic Bulk Heterojunction Photovoltaic Devices

5.1.1 Introduction

Solar energy has been identified as the leading renewable energy source to meet the challenge of increasing demand for energy. Organic photovoltaics (OPV), as an emerging sector in the photovoltaic industry, have been seeing a rapid development in recent years. The recent record shows that the best OPV cell (employing a tandem structure) has broken the 10% efficiency threshold for commercial applications [84].

In a typical bulk heterojunction (BHJ) architecture, the most widely used structure in an OPV device, a solvent-cast layer of π-conjugated polymer and fullerene-derivative blend is sandwiched between a cathode and anode. The most common polymer/fullerene blend with high η-value comprises an organic donor (D) such as P3HT or PTB7 and a fullerene derivative as an accepter (A), of which chemical structures are shown in Figure 2.1. The donor polymer in the blend absorbs in the UV-visible part of the solar spectrum that compensates the optical transparency of the fullerene molecules in the same energy range. Upon photoexcitation of the donor, excitons (tightly bound intrachain electron-

hole pairs) are initially photogenerated; their dissociation is facilitated by the energy level differences between the Lowest Unoccupied Molecular Orbital (LUMO) level of the donor polymer and the Highest Occupied Molecular Orbital (HOMO) level of the acceptor fullerene. To reach the D-A interfaces, the excitons first diffuse towards the polymer domain boundary within ~10 ps [36, 37], where upon arrival, they form charge transfer excitons [38, 39]. The charge-transfer excitons then separate into more loosely-bound polaron pairs (PP), which are the intermediate species at the D-A interfaces having relatively long lifetime (namely, few microseconds [85]). Subsequently, the PP may separate into "free" electron and hole polarons that are available for transport, and can be readily collected at the anode and cathode, respectively.

The major challenge that the OPV faces at the present time is its low η compared with other photovoltaic devices, with the recombination of PP at D-A interfaces being a major limiting factor [37, 86]. In addition to optimizing parameters such as material mass ratio, active layer thickness, and annealing temperature, numerous other approaches have been taken to enhance the efficiency by improving the device morphology [5, 87, 88, 89], engineering new polymer/fullerene materials with various HOMO(D)-LUMO(A) offset [90, 91], manipulating electrode property [92], employing tandem cell architecture [84, 93], and enhancing optical absorption [94]. A number of these approaches involve introducing nanoparticles dopants (or additives) into the active layer and/or fabrication process [5, 92, 95].

In the present work, we demonstrate a new method to improve OPV efficiency by doping the device active layer with spin 1/2 radicals to reduce PP recombination at the polymer/fullerene interfaces. We demonstrate that the spin 1/2 radical additives facilitate

the intersystem crossing of PP from singlet to triplet spin configuration, thereby enhancing PP separation into free charges in the device; this process is unraveled via magneto-photocurrent (MPC) of the doped devices. We demonstrate that the spin 1/2 radicals may spin flip the acceptor electron spin via an exchange mechanism that requires resonant conditions. We believe that this method may work with other D–A blends if appropriate radicals in resonance are found, in concert with other existing methods to yield even higher OPV device efficiencies. Here, we optimized the D-A weight ratio to have the best performance on this blend system and then studied the role of spin ½ radical on the optimized device.

We also studied the effect of additives on the performance of solar cells based on the low band gap polymer, PTB7. As morphology of an active layer plays an important role in OPV performance, here, we show how morphology improvement enhances the power conversion efficiency (PCE) of OPV cells.

5.1.2 Experimental

The bulk heterojunction OPV devices investigated in this study were composed of an indium tin oxide (ITO) anode modified by a spin-cast polyethylenedioxythiophene/ polystyrene sulphonate (PEDOT/PSS) layer; an active material layer spin-cast from blend of polymer donor, and fullerene acceptor (and spin ½ radical Galvinoxyl or 1-8 diiodooctane (dio) additive when applicable); and capped with Ca/Al cathode. The ITO-coated glass substrates were cleaned by ultrasonic treatment (in detergent, deionized water, acetone, methanol, and propanol sequentially) and oxygen plasma treatment. The PEDOT/PSS layer was spin-cast at 5000 RPM for 40 seconds in ambient condition and

transferred into a nitrogen-filled glovebox (O_2 <1 p.p.m.) to bake at 110 ºC for 30 minutes. The blend that yielded best device performance (η=4%) comprised P3HT, PCBM, and galvinoxyl. It was prepared in the following way: P3HT (16 mg/ml) and PCBM were dissolved at 1.2:1 weight ratio in 1,2-dichlorobenzene (ODCB). The blend was heated at 50 ºC for 30 minutes and stirred overnight before mixing with galvinoxyl (3 wt%, defined as percentage of total P3HT/PCBM weight) and stirring for one additional hour Blends of other P3HT/PCBM mass ratios were prepared by only changing mass ratio while keeping the total P3HT/PCBM mass unchanged. The active layer was obtained by spin-casting the blend at 400 RPM for 6 minutes and annealing at 150 ºC for 30 minutes. A similar recipe was followed for PTB7/PC_{71}BM blend system. 10 mg of PTB7 and 15 mg of PC_{71}BM in weight ratio (1:1.5) were dissolved in 1ml of ODCB and the solution was prepared the solution for the device which exhibits the best performance with addition of 3 wt% dio. The solution was spin casted at 800 RPM and dried in vacuum at room temperature for at least 10 hours before the evaporation of the top electrode. The device fabrication was completed by thermally evaporating a 20 nm thick film of Ca followed by a 100 nm thick film of Al. Finally, the completed device was encapsulated under a cover glass using UV-curable optical adhesive (Norland, NOA 61).

Device I-V characteristics were measured using a Keithley 236 Source-Measure unit. The light intensity of the solar simulator, composed of a xenon lamp and an AM1.5G filter, was calibrated to 100 mW/cm^2 using a precalibrated silicon PV cell. When measuring MPC, the OPV devices were transferred to a cryostat that was placed in between the two poles of an electromagnet producing magnetic field, B up to ~200 mT.

The devices were illuminated with a tungsten lamp and measured at zero bias using a Keithley 236 apparatus, while sweeping the external magnetic field. The MPC is defined as MPC(B) = [PC(B)/PC(0) - 1].

5.1.3 Experimental Results and Discussion

5.1.3.1 Spin Enhanced Organic Bulk Heterojunction Photovoltaic Devices

Figure 5.1 shows the J-V characteristics of the OPV devices of a P3HT/PCBM system at different weight percentage of PCBM under the same spin coating and 1.5 AM illumination condition. It is clearly seen in the figure that performance of OPV devices first increases and becomes maximum at 1.2:1 weight ratio (i.e., at 45 wt% of PCBM) and then decreases with increase in the PCBM concentration. Here, 1.2:1 is an optimum P3HT: PCBM weight ratio [96] at which maximum exciton dissociation and efficient charge carrier extraction occurs in the device made from this blend.

The spin 1/2 radical that enhances OPV performance in this kind of devices is galvinoxyl (2,6-di-*t*-butyl-α-(3,5-di-*t*-butyl-4-oxo-2,5-cyclohexadien-1-ylidene)-*p*-tolyloxy), a π-conjugated molecule with C2 symmetry (Figure 5.2 inset). The bulky *t*-butyl groups on the molecule stabilize the radical by keeping other molecules apart, thus preventing further radical–radical spin interaction in the solid state. The unpaired electron is delocalized over the entire molecule and thus, its molecular structure may be regarded as resonance hybrid of two configurations having a localized unpaired spin-polarized electron on different oxygens [97].

First, we investigated the effect of galvinoxyl doping in the active layer of

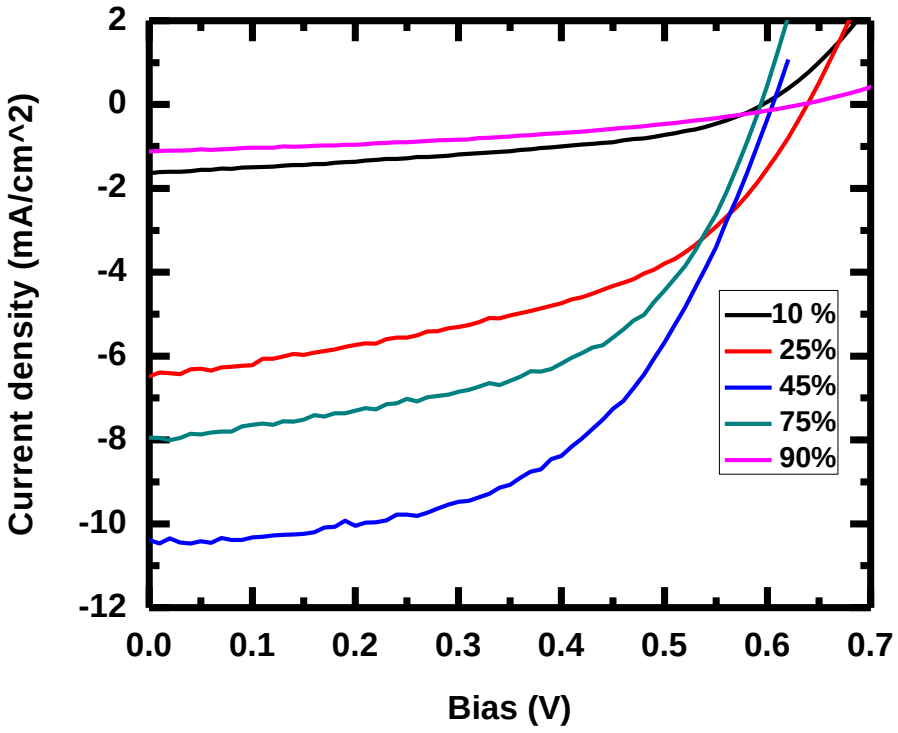

Figure 5.1. J-V characteristics of P3HT:PCBM OPV devices at different percentages of PCBM under AM 1.5 illumination.

'standard' P3HT/PCBM device with 1.2:1 weight ratio. We note that our standard P3HT/PCBM devices were fabricated using a well-optimized recipe, and the obtained η-value is ~ 3.4%, close to the published value by Plextronics [98]. Figure 5.2 shows that by doping 3 wt% of galvinoxyl, η increases from 3.4% (short circuit current: J_{sc}=10.4 mA/cm^2, open circuit voltage: V_{oc}=0.6 V, fill factor: FF=0.56) to 4.0% (J_{sc}=11.3 mA/cm^2, V_{oc}=0.6 V, FF=0.62), exhibiting an 18% enhancement in the power conversion efficiency. The 18% increase in η is significantly larger than the standard deviation in η-values of the standard reference devices (±3%); thus, doping with galvinoxyl

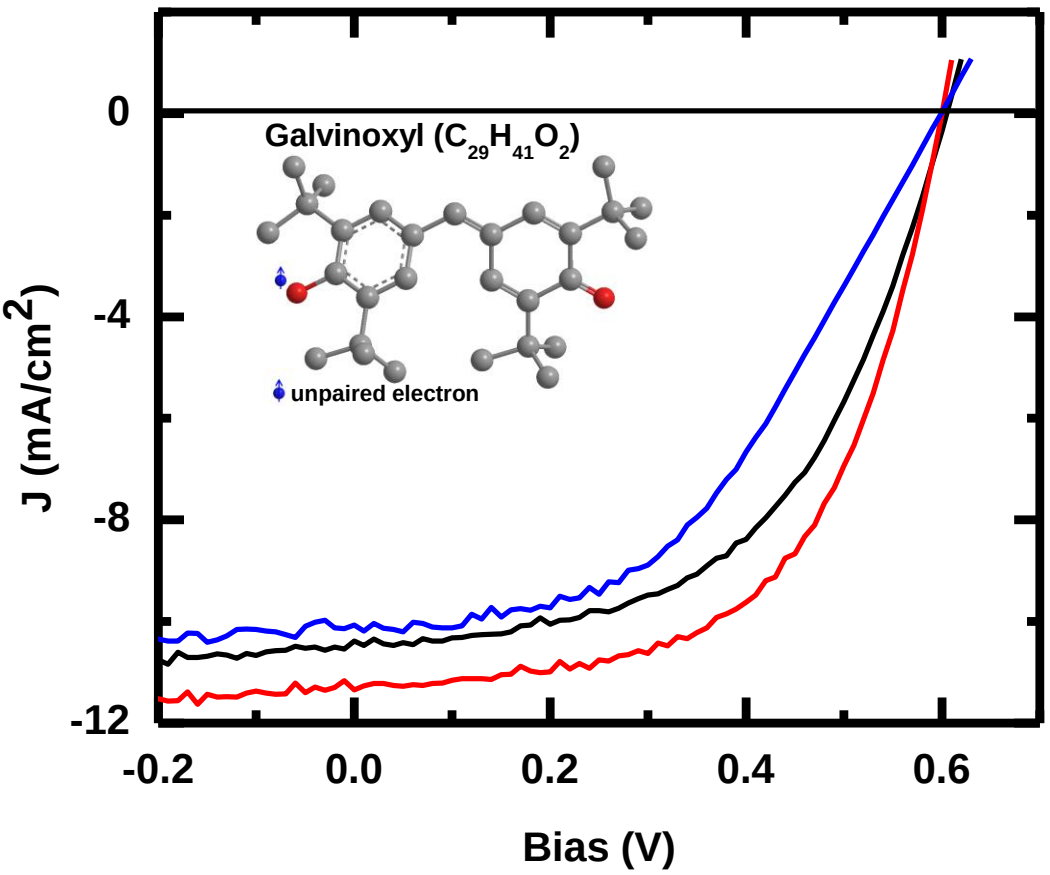

Figure 5.2. J-V characteristics of OPV solar cells of pristine P3HT/PCBM blend (η = 3.4%, Black line), the blend doped with 3 wt% galvinoxyl radicals (η = 4.0%, Red line) and the blend doped with 3 wt% precursor (η = 2.8%, Blue line) under AM1.5 'sun illumination' condition. The inset shows the galvinoxyl molecular structure.

unambiguously enhances the device η-values. The 8.7% increase in J_{sc} that accounts for about half of the improvement in the device η indicates that carrier generation is enhanced, or carrier recombination is reduced, or both.

Figure 5.3 summarizes the device properties for all investigated doping concentrations (1.5-17 wt%). The enhancement in J_{sc} and η induced by the galvinoxyl radicals peaks at ~3 wt%, and gradually vanishes with further increased doping. Actually,

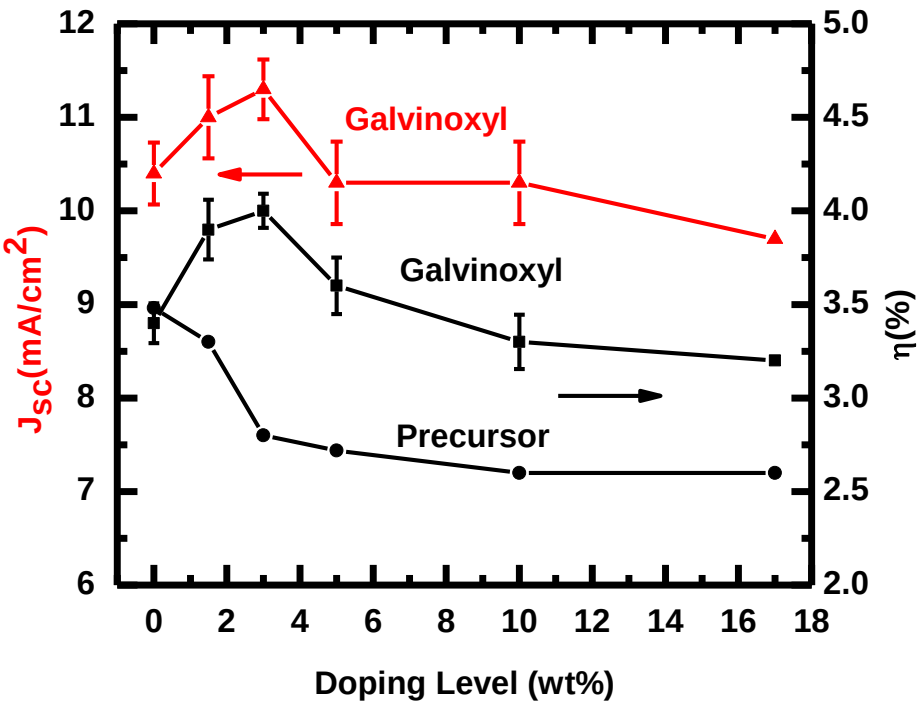

Figure 5.3. The change in OPV device properties with galvinoxyl-additive concentration; J_{sc} (triangles) and η (squares) are shown versus galvinoxyl wt% in the P3HT/PCBMblend. η of OPV devices doped with galvinoxyl precursor that does not possess spin 1/2 radical is also shown for comparison (circles).

at high doping level (>10 wt%) galvinoxyl suppresses the device performance. The optimum doping concentration (~3 wt%) at which η is maximum and divides the effect of galvinoxyl doping into two regimes: an "enhancement" regime, where η increases with doping; and a "suppression" regime, where η decreases with doping.

We also performed (MPC) measurements on the galvinoxyl-doped OPV devices to unravel the underlying mechanism for the increase in *J*sc with wt%. Figure 5.4 shows the obtained MPC response of OPV devices having various galvinoxyl wt%. It is clearly seen that galvinoxyl additives reduce the MPC value without changing the field response. It has been known that MPC in OPV blends is due to magnetic field manipulation of spin

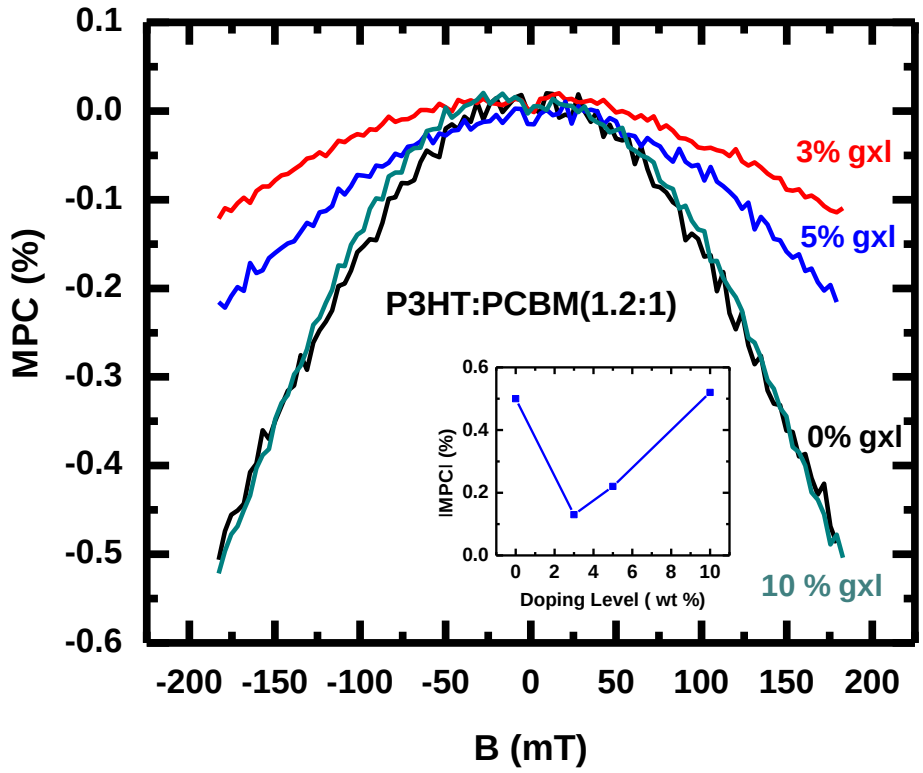

Figure 5.4. MPC response of OPV devices doped with galvinoxyl up to field, *B* of 190 mT. The inset summarizes the MPC value at 190 mT versus galvinoxyl wt%.

triplet and singlet states within the PP species [99-101]. Therefore, the reduction of MPC with wt% shows that the spin 1/2 radicals interfere with the intersystem crossing rates among the various spin states of the PP species, revealing the importance of the galvinoxyl spin rather than its ability to serve as donor or acceptor. We therefore conclude that reduced PP geminate recombination at the D–A interfaces is responsible for the enhanced carrier photogeneration upon galvinoxyl doping. The remaining enhancement in η with the galvinoxyl additives is due to an increase in *FF*, which indicates a reduced series resistance that results from improved carrier transport.

We note that the MPC reduction with galvinoxyl wt% follows the same trend as that of the OPV enhancement with wt%. Figure 5.4 inset shows that the most MPC reduction occurs at 3 wt%; the MPC response comes back to that of pristine device at 10 wt%. This further shows the existing correlation between the spin 1/2 properties of the galvinoxyl additives and the OPV enhancement. We also performed several 'control experiments' for understanding the OPV enhancement upon galvinoxyl doping.

In order to investigate whether the enhancement in J_{sc} with doping is due to an increase in the device active layer absorption, we compared the absorption spectra of the pristine and doped P3HT/PCBM films, as shown in Figure 5.5(a). Since the two spectra are very similar to each other, and in particular, the galvinoxyl absorption peak at 430 nm is not discerned in the doped sample, it suggests that the change in film absorption due to the addition of galvinoxyl is within the experimental error. We thus conclude that the enhancement in J_{sc} is not caused by a change in absorption with doping. In Figure 5.5(b), we compare the External Quantum Efficiency (EQE) of the pristine and 'galvinoxyl doped' devices. The enhancement in EQE of the doped device does not appear at 430 nm where the galvinoxyl absorption is the strongest; rather, EQE increases across the entire spectrum. We conjecture that galvinoxyl does not act as a donor molecule in this blend system.

Morphology change and its impact on exciton diffusion towards the D-A interfaces also plays an important role in determining J_{sc}. In order to investigate whether the film morphology changes due to the addition of galvinoxyl molecules, we compared XRD patterns of the pristine and doped P3HT/PCBM films (Figure 5.5(c)). The P3HT (100) peaks of both films exhibit identical XRD diffraction patterns. Using the peak

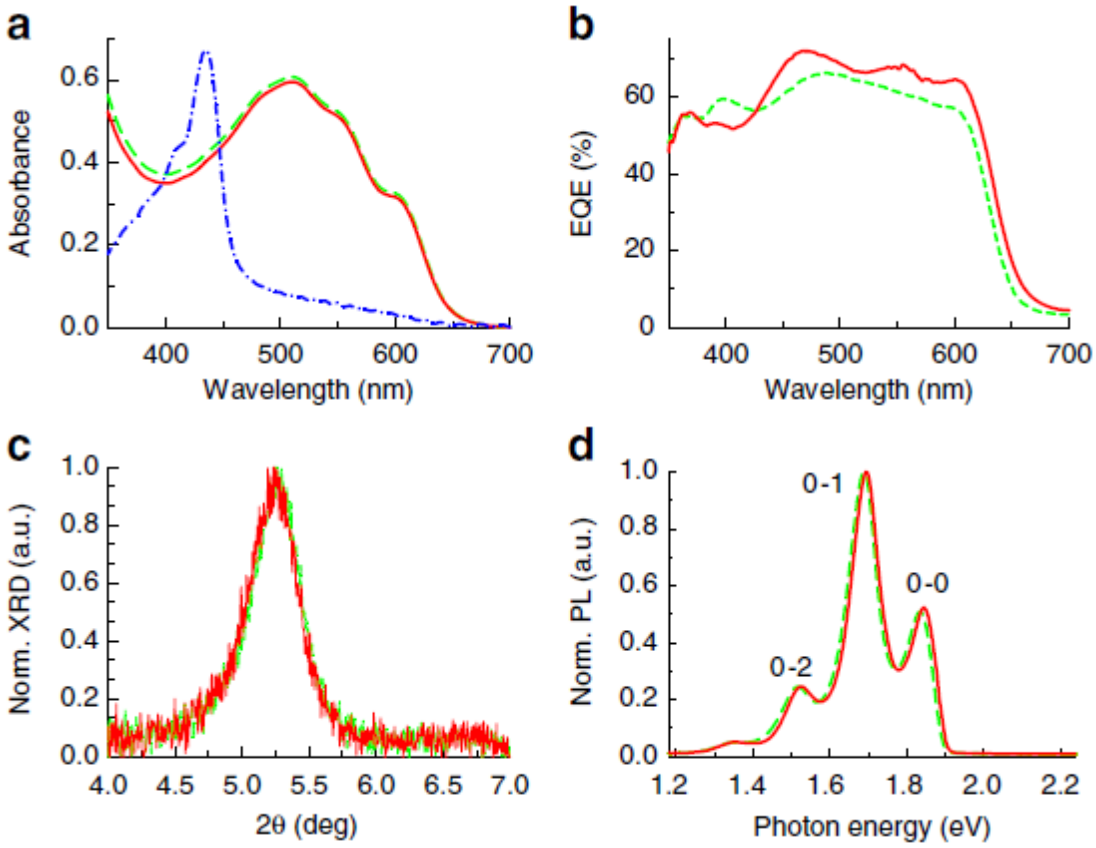

Figure 5.5. The UV/Vis absorption spectrum of pure galvinoxyl (dash-dot line), pristine (dashed line) and doped (solid line) P3HT/PCBM blend (a). The EQE spectrum of OPV solar cells based on pristine (dashed line) and galvinoxyl-doped (solid line) P3HT/PCBM blend (b). The XRD pattern of pristine (green dash) and doped (red solid) P3HT/PCBM films (c). PL spectrum of pristine (dashed line) and doped (solid line) P3HT/PCBM. The phonon replicas are assigned. Norm., normalized (d).

position and full width at half maximum (FWHM) as extracted from XRD scans, we estimated via the Scherrer's relation that the P3HT domain size in both films are ~19 nm. This size is ideally suited to the commonly accepted 10 nm exciton diffusion length the P3HT domains [85].

The relative intensity of 0-0 and 0-1 peaks of photoluminescence (PL) provides another way to determine the degree of crystallization of the P3HT domains [102].The normalized PL of pristine and doped (3 wt%) P3HT/PCBM films are shown in Figure 5.5(d). The identical PL spectra indicate that the packing order of polymer chains in the P3HT domains is not affected by the addition of galvinoxyl, and thus, the exciton lifetime in the P3HT domains is unchanged. Similar to the XRD and PL results, the TEM images (not shown here) show no observable morphology change caused by the galvinoxyl doping. We therefore conclude that no change in film morphology can be responsible for the increase in J_{sc}. Consequently, the only viable mechanism for J_{sc} increase is the charge carrier recombination upon galvinoxyl doping.

To further check the importance of the galvinoxyl spin 1/2 properties rather than its doping ability, we measured the OPV device performance with the addition of 'galvinoxyl precursor' molecule that has one extra hydrogen atom, and thus does not possess a spin 1/2 radical. In contrast to galvinoxyl doping, we found that doping with this precursor monotonically reduces the OPV performance (Figure 5.3). We therefore conclude that the viable mechanism for the OPV η increase with galvinoxyl additives is suppression of PP recombination at the D-A interfaces due to spin 1/2 radicals.

The experimental evidence indicates that the cause for the enhanced η-value in the galvinoxyl-doped OPV devices is the reduced PP recombination rate at the P3HT/PCBM domain interfaces due to the spin 1/2 radical additives. We still need to unravel the mechanism by which galvinoxyl reduces PP recombination. As galvinoxyl is a spin 1/2 radical, we propose a 'spin-flip' mechanism that facilitates PP separation at the P3HT/PCBM interfaces by converting photogenerated PP from spin singlet to triplet

(Figure 5.6(a)) via spin exchange interaction between the PP and galvinoxyl. As triplet PP has longer lifetime than singlet PP, the enhanced intersystem crossing results in a longer-lived species having a better chance to dissociate.

Consider that a photogenerated exciton in the P3HT domain has spin-up electron in the LUMO level and spin-down hole in the HOMO level. Upon arrival at the D–A interface, the electron transfers to the PCBM LUMO level, forming a singlet PP (Figure 5.6(a); upper left), with the spin-down hole in the P3HT HOMO level. The singlet PP species can either dissociate into free carriers (polarons) in the P3HT and PCBM separate domains, or geminately recombine. When a spin 1/2 radical such as galvinoxyl, which has spin-polarized singly occupied molecular orbital (SOMO) and LUMO levels with designated spin orientations, is introduced next to the singlet PP, then it may form a complex with PCBM providing a spin-down polarized empty LUMO level in resonance (Figure 5.6(b)) with the spin-up filled PCBM LUMO level next to the charged PCBM molecule (Figure 5.6(a) right). This mediates an exchange interaction between the up-spin negative polaron and the ‘virtual’ down-spin of galvinoxyl LUMO that flips the polaron up-spin to down-spin, thereby forming a lower-energy triplet PP (Figure 5.6(a) bottom left). The PP triplet species has a longer lifetime because it is ‘spin-forbidden’, having a reduced geminate recombination rate. This may facilitate its dissociation into free polarons. The same mechanism can be equally applied for a photogenerated PP with spin-down electron in the P3HT LUMO level, via exchange interaction with a spin-up defined LUMO level of galvinoxyl radical.

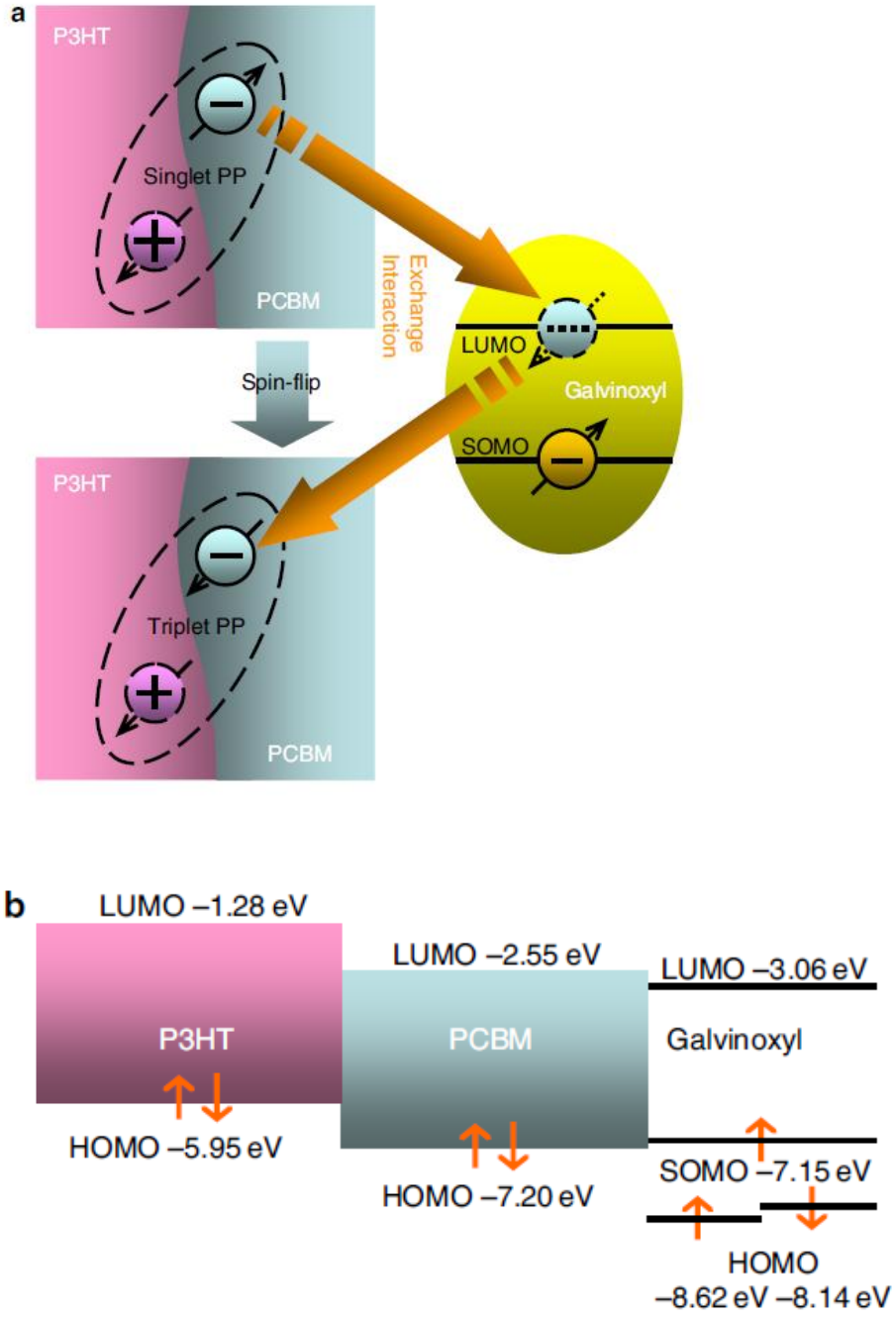

Figure 5.6. The spin exchange mechanism where the photogenerated PP at the D–A domain interface changes its spin configuration from singlet to triplet augmented by the galvinoxyl spin 1/2 radical (a). The calculated HOMO, LUMO, and SOMO levels of P3HT, PCBM, and galvinoxyl that show a clear resonance between the radical and acceptor LUMO levels (b).

5.1.3.2 Low Band Gap Organic Bulk Heterojunction Photovoltaic Devices

Although P3HT is the most studied polymer in OPVs, based on BHJ with a PCBM as an accepter, efficiency of the device based on this BHJ it is still significantly lower that of inorganic photovoltaic devices. Even after optimizing the parameters such as material weight ratio, active layer thickness, and annealing temperature, its efficiency is around 5 % [96]. In spite of its intense absorption in the visible region (Figure 5.7), it is not energetically optimized for light harvesting from the solar spectrum, especially in the near infrared (IR) region. In order to maximize the light harvesting in OPV devices, low band gap polymers are currently being synthesized and studied [5, 89]. After an extensive structural optimizations, Liang et al. synthesized a new polymer (E_g ~1.6 eV) from the poly-thienothiophene-benzodithiophene (PTB) family, called PTB7 [89], which exhibited an excellent photovoltaic effect due to the extension of spectral absorption profile into the IR region, as shown in Figure 5.7 .

PTB7 shows weak absorption below 500 nm (Figure. 5.7) whereas $PC_{71}BM$ exhibits absorption in the wavelength range below 600 nm [103]. Therefore, the PTB7/$PC_{71}BM$ blend shows a strong spectral absorption profile in the solar spectrum range, as shown in Figure 5.8.

We fabricated the OPV devices based on PTB7/$PC_{71}BM$ with and without the dio additive. Figure 5.9 shows the performance of the photovoltaic effect in this low band gap polymer blend system. We observed 5.3 % PCE with short circuit current: J_{sc}=13 mA/cm^2, open circuit voltage: V_{oc}=0.76 V, fill factor: *FF*=0.53.

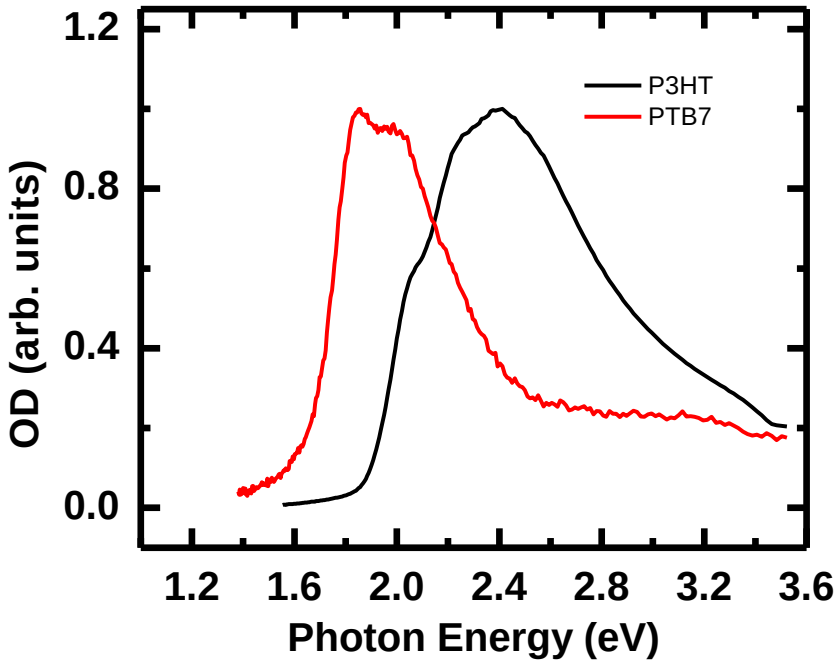

Figure 5.7. Linear absorption spectrum of P3HT and PTB7 polymer.

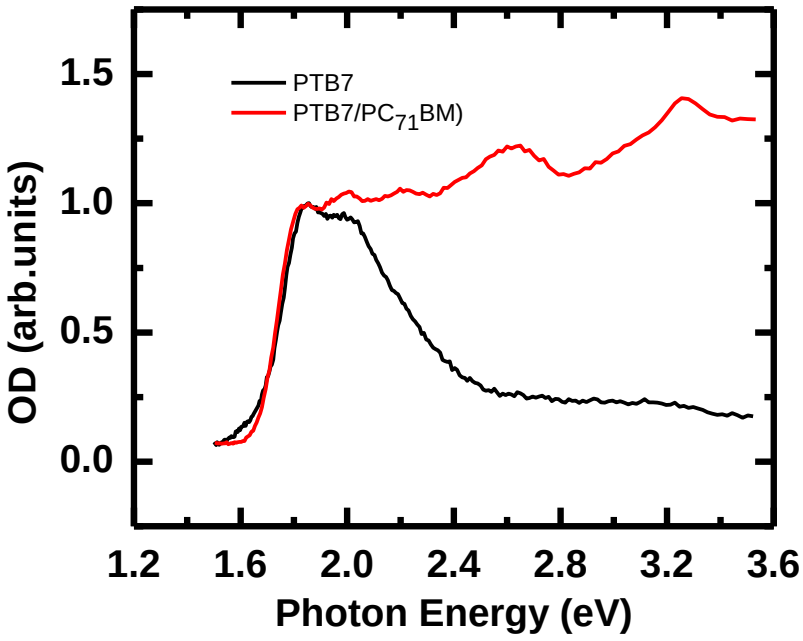

Figure 5.8. Linear absorption spectrum of PTB7 and its blend with $PC_{71}BM$.

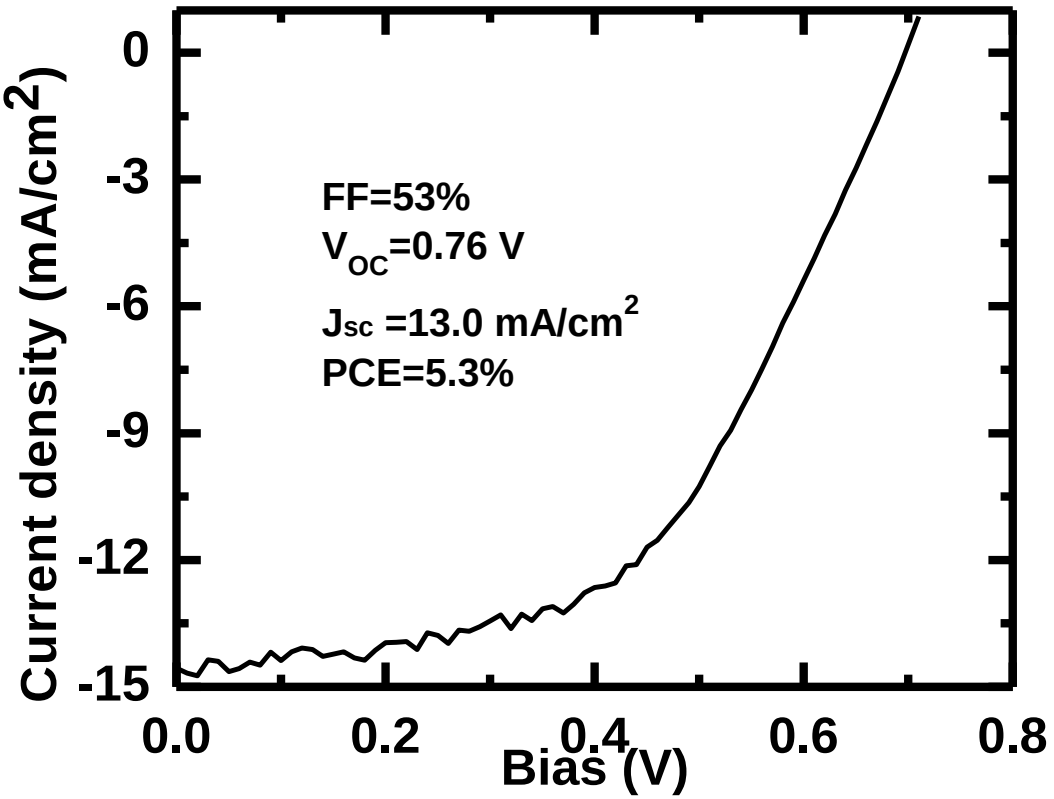

Figure 5.9. J-V characteristics of PTB7/ $PC_{71}BM$ device under AM 1.5 illumination.

Figure 5.10 shows the J-V characteristics of the OPV devices of PTB7/ $PC_{71}BM$ at different weight percentage of dio under the same spin coating and 1.5 AM illumination condition. It is clearly seen in the figure that performance of OPV devices first increases, reaches a maximum at 3wt% dio, and then decreases with increase in the dio percentage.

We observed maximum PCE (6.9 %) with short circuit current: J_{sc}=16 mA/cm^2, open circuit voltage: V_{oc}=0.7 V, fill factor: *FF*=0.60 at 3% dio percentage. We have achieved a significant increase of η of the 3 wt% -doped device relative to devices based

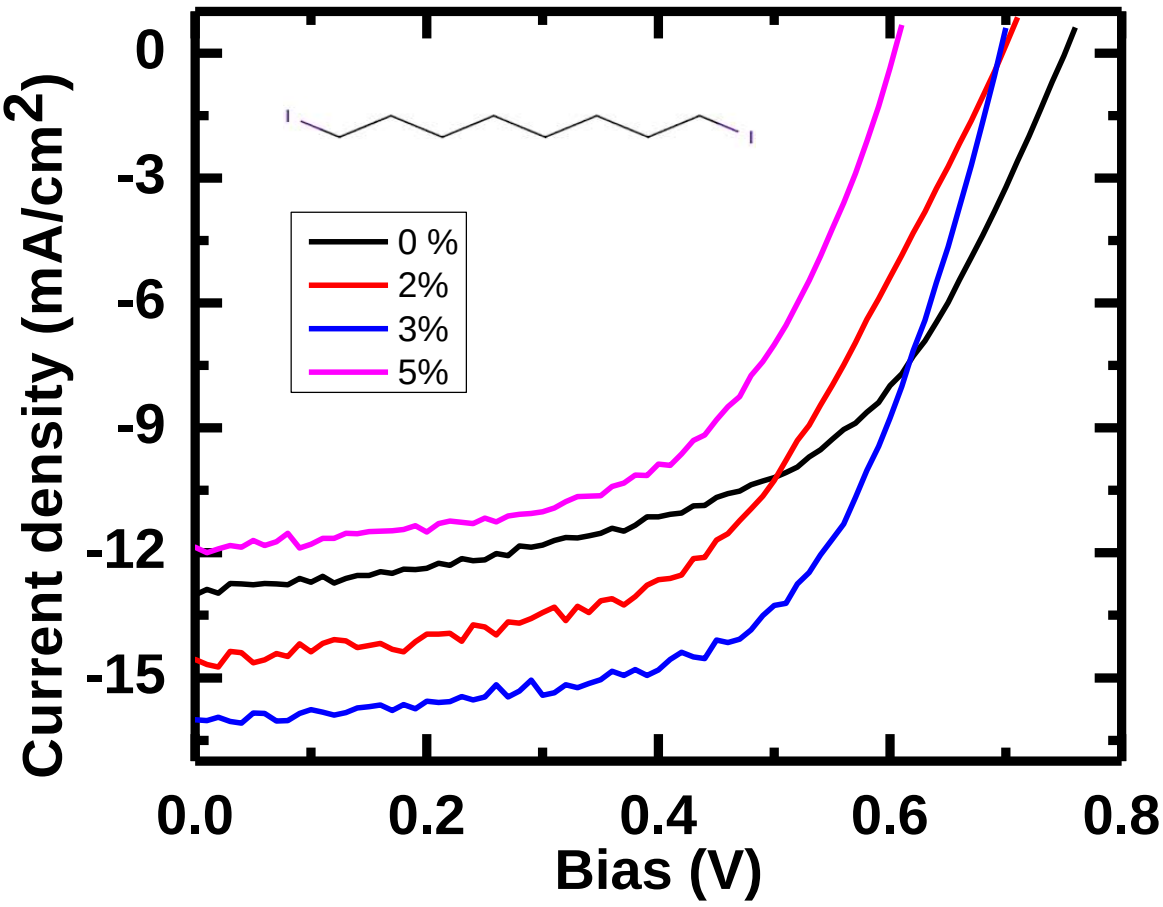

Figure 5.10. J-V characteristics of PTB7/$PC_{71}BM$ OPV devices at different percentage of dio under AM 1.5 illumination; inset shows the chemical structure of dio.

on pristine blend. The enhancement in the performance of OPV solar cell efficiency by doping the device active layer with dio is due to the change in nanomorphology of the blend film. The device with 3 wt% dio has optimal phase separation and interpenetrating networks [5, 89] so that minimum recombination and maximum charge photogeneration occur in this device. The improved morphology causes an increase in J_{SC} and FF and hence the η.

5.1.4 Conclusion

We conclude that galvinoxyl additives activate a spin-flip process that converts PP species at the D–A interfaces from spin singlet to triplet, and this reduces the overall PP recombination rate and hence enhances the PP separation into free charges in the device. We believe that galvinoxyl forms a complex with the PCBM at the P3HT/PCBM interfaces (η enhancement was not observed on PCBM only device). Also, the OPV enhancement is maximized at certain galvinoxyl optimal concentration; this can be understood if nearest neighbour galvinoxyl/PCBM complex molecules at high wt% are spin-paired to form spin singlet. Therefore, overdose of galvinoxyl molecules may reduce their ability to provide the spin-flip mechanism necessary for reducing the PP recombination rate. Also, a low band gap blend system (PTB7/PC_{71}BM) that has a strong spectral absorption profile covering the solar spectrum has higher η value compared to P3HT/PCBM system. Doping with an additive (dio) in the active layer of PTB7/PC_{71}BM device indicates that morphology plays an important role in the performance of photovoltaic devices.

5.2 Magneto-photocurrent of Charge Transfer Complex in Organic Blends for Photovoltaic Applications

5.2.1 Introduction

The formation of a charge transfer complex (CTC) has been shown to be a crucial intermediate step in the charge separation process [36, 37, 38, 39, 104] of efficient organic photovoltaic (OPV) cells [5, 84, 89] based on blends of 1-[3-(methoxycarbonyl)propyl]-1-1-phenyl)[6,6]C_{60} (PCBM) and an organic donor, such as poly 3-hexylthiophene (P3HT). CTC is a D-A interface bound pair of negatively charged polaron (P^-) located on PCBM and positively charged polaron (P^+) localized on donor. The efficiency of OPV cells is critically dependent on the ability of the photogenerated singlet exciton (SE), localized on the donor, to partially charge separate into a singlet CTC on a short timescale before SE radiative recombination can occur. Subsequently, and not less important, on a longer timescale, the cell photo-current is determined by the ability of the CTC to fully separate into positive and negative charge carriers either directly or through an intermediate step forming polaron pairs (PP) that eventually dissociate to mobile charges. Since the blend is in general of amorphous structure, the P^+--P^- separations is not fixed giving rise to a distribution of CTC binding energies; PP can then be regarded as CTC with large P^+--P^- separations (>1-2 nm), low binding energy, and negligible exchange interaction. Importantly, CTC and photogenerated excitons can be distinguished by their characteristic exchange coupling, J. For photogenerated excitons in a donor such as P3HT, J may be as large as 0.4 eV (approximately half the energy difference between SE and triplet exciton, TE), while the exchange interaction is

exceedingly small for CTC (and PP) due to their ionic nature having negative and positive charges on different molecules.

Magneto-conductance (MC) and MPC in OPV cells, as well as magneto-photoluminescence (MPL) and magneto-photoinduced absorption (MPA) in films made of organic polymers and blends of D-A [72], have been studied over the recent years. Various mechanisms accounting for these magnetic field effects (MFE) have emerged from these studies. Among them we note several that are relevant to this work: (a) spin-mixing by the hyperfine (HF) interaction within polaron pairs (PP) and bipolarons [24,33,42], (b) the difference, Δg, in the electron and hole g-factors in polymer/fullerene blends [72, 31], and (c) a number of mechanisms that involve triplet excitons (TE) [72, 22, 55]. Here, we address the role of CTC in OPV cells made of D-A blends by studying the effect of external magnetic field on their photocurrent (PC).

5.2.2 Experimental

A solvent-cast layer of organic D-A blend is sandwiched between the cathode and anode of an OPV cell whose fabrication procedure is explained in detail in Section 5.1.1. We have used several different organic donors obtained from various sources (described in Section 2.1): regio-regular poly(3-hexylthiophene) (RR P3HT), regio-random P3HT (RRa P3HT), PTB7 with and without 1-8-diiodooctane (dio) molecules additive [89], and MEHPPV. These blends are known to form bulk hetero-junctions (BHJ) of nano-sized domains that facilitate both charge photogeneration and charge transport and collection in the blend. The power conversion efficiency (PCE) of the OPV cells made for this study varies between 0.1-7%. All the measurements reported here were performed at room

temperature. For the MPC measurements, the OPV devices were transferred to a cryostat that was placed in between the two poles of an electromagnet producing magnetic field, B up to ~ 0.3 T. The devices were illuminated with either a tungsten lamp or a UV-visible light emitting diode and measured at zero bias (V_b=0) while sweeping the external magnetic field. The MPC is defined as MPC (B) = [PC(B)/PC(0) − 1].

5.2.3 Experimental Results and Discussion

Figures 5.11-5.15 show the PCE and MPC response in a series of OPV cells made of blends of the above organic donors and PCBM. They are all characterized by a broad nonsaturating (up to at least B~0.3 T) component, MPC_W, whose magnitude still varies at the highest field employed. This broad and nonsaturating component is unlikely to arise from spin mixing due either to the HF interaction or triplet mechanism, since a typical HFI constant for protons in organics [33] is $a/2\mu_B$ ~3 mT (μ_B is the Bohr magneton) while the typical ZFS parameter D for TE in P3HT is of order [105] $D/2\ \mu_B$ ~ 60 mT, or less; thus, none of these mechanisms can account for a response that varies strongly beyond B=300 mT. Depending on the organic donor used, MPC_W is either decreasing or increasing with increasing |B| (Figures 5.11-5.15)). The response contains also a narrow contribution, MPC_N, whose half width at half maximum is HWHM~1-2 mT and its magnitude is ~0.02-0.03 % (Figures 5.11-5.15)). Such a narrow response may originate at the polaron-proton HFI within the organic donor molecule.

In order to shed light on the origin of MPC (B) response, we have measured the MPA of a film of RRP3HT/PCBM (1.2:1 by weight) blend. The black line in Figure 5.16

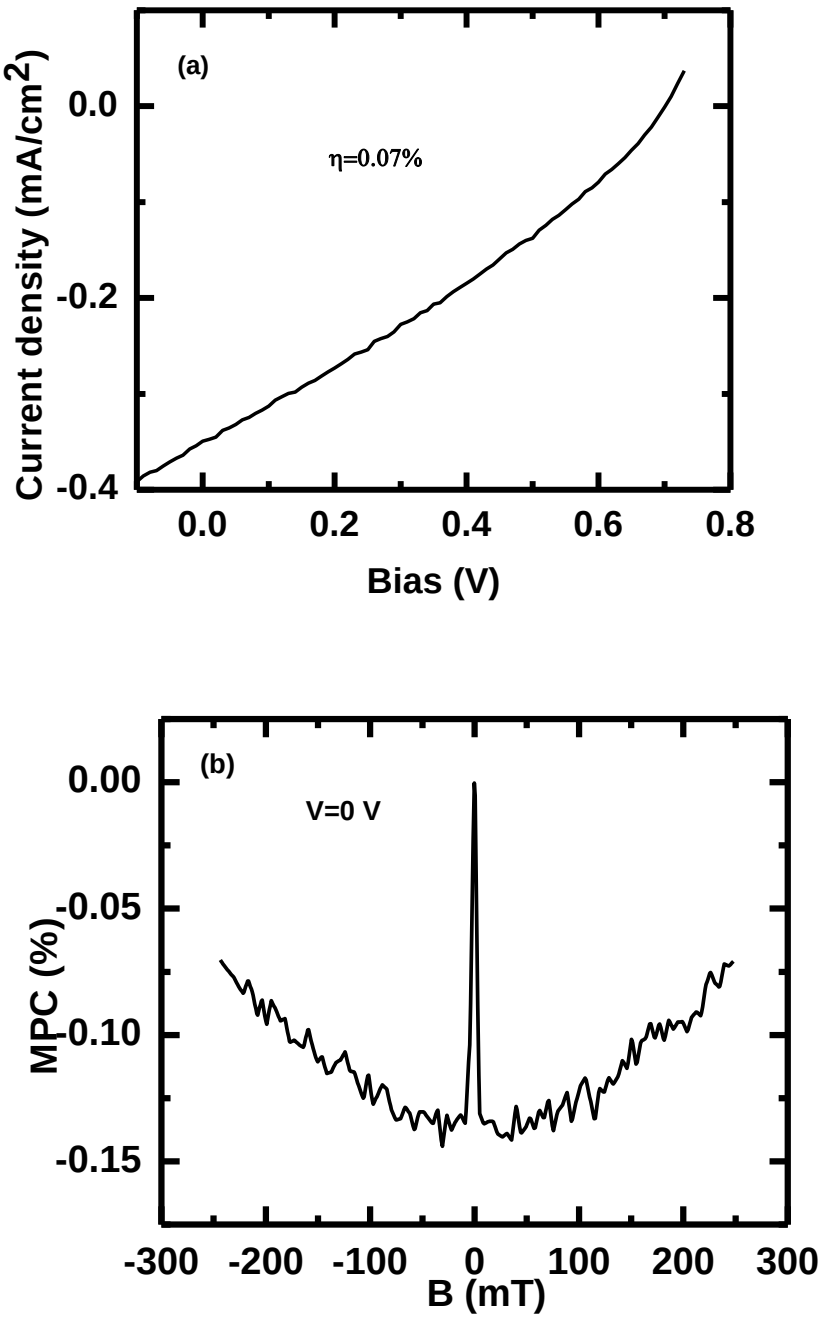

Figure 5.11 The PCE and MPC(B) response of RRa P3HT/$PC_{61}BM$ (1:2) based OPV cell.

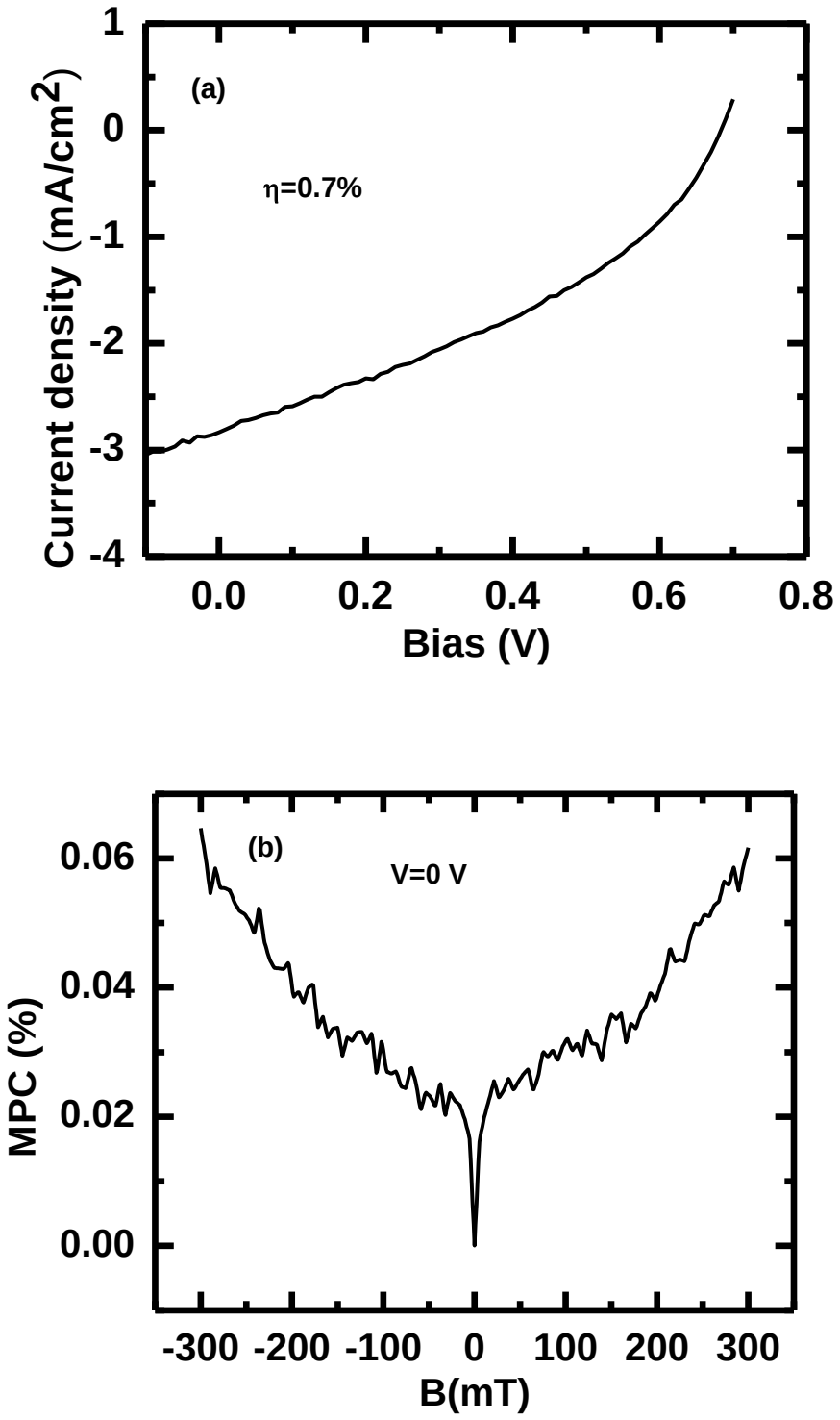

Figure 5.12 The PCE and MPC(B) response of MEH-PPV/$PC_{61}BM$ (1:4) based OPV cell.

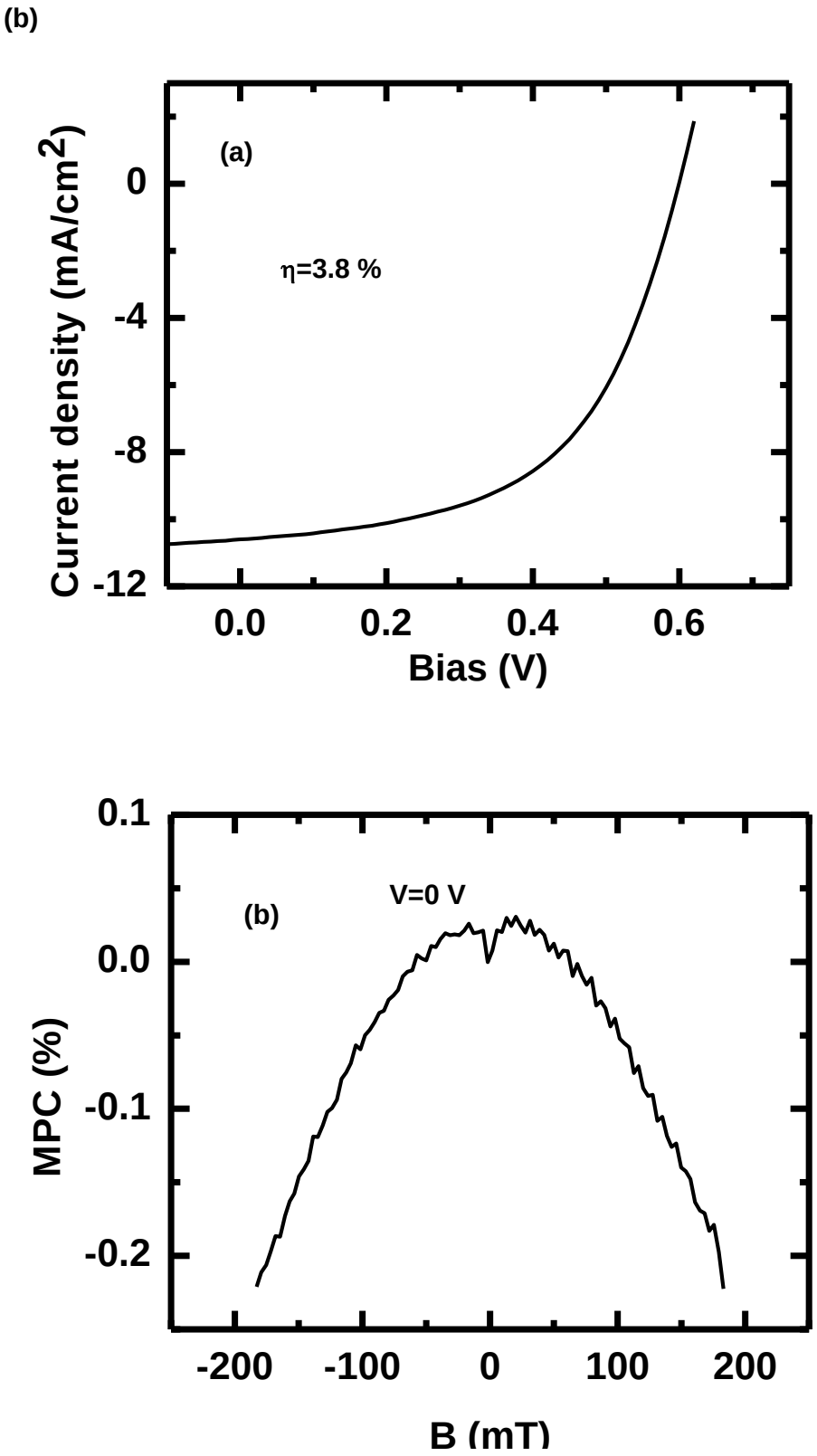

Figure 5.13 The PCE and MPC(B) response of RR P3HT/$PC_{61}BM$ (1.2:1) based OPV cell.

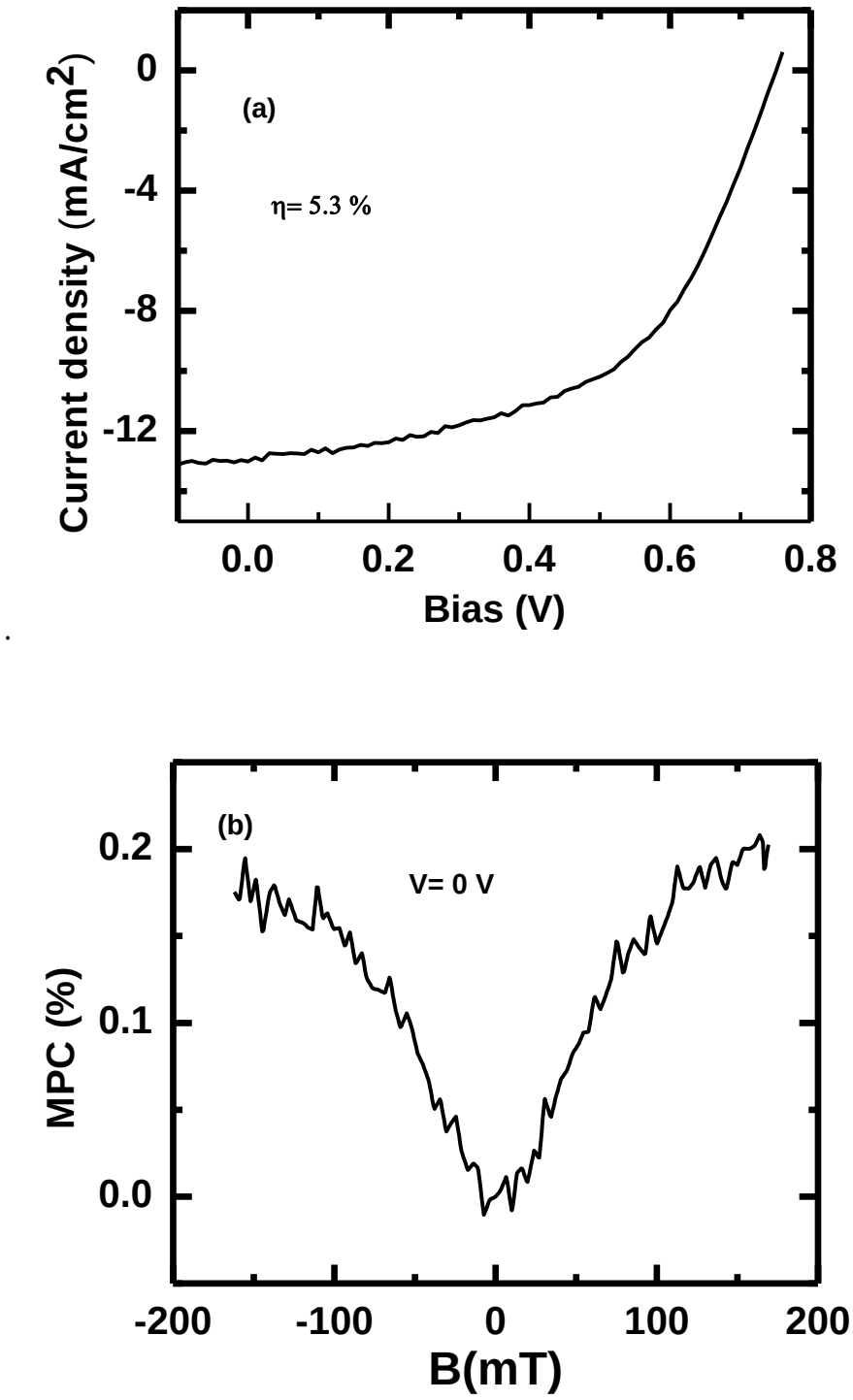

Figure 5.14 The PCE and MPC(B) response of PTB7/$PC_{71}BM$ (1:1.5) based OPV cell.

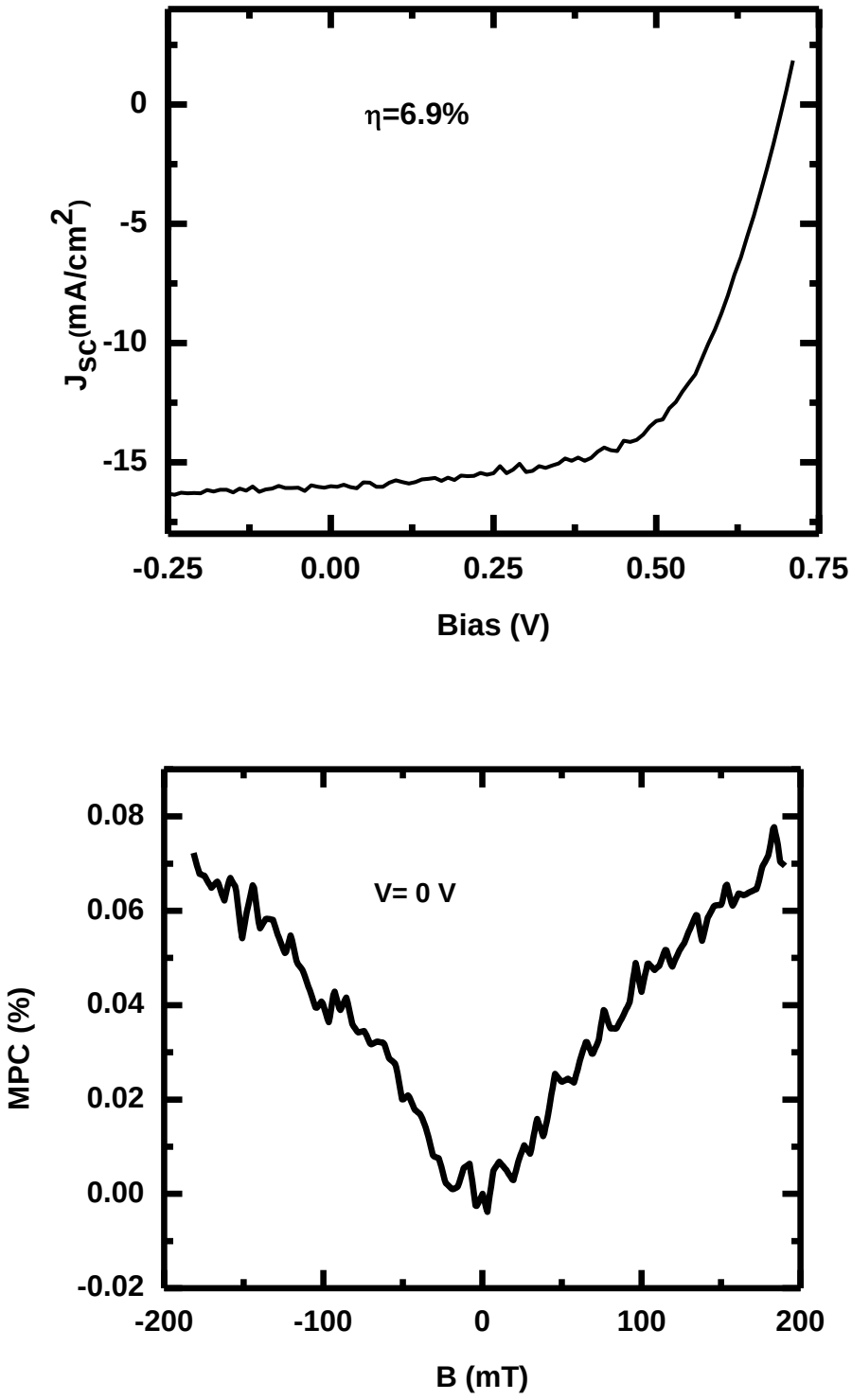

Figure 5.15 The PCE and MPC(B) response of PTB7/$PC_{71}BM$ (1:1.5) based OPV cell with 3 wt% of 1,8-diiodooctane.

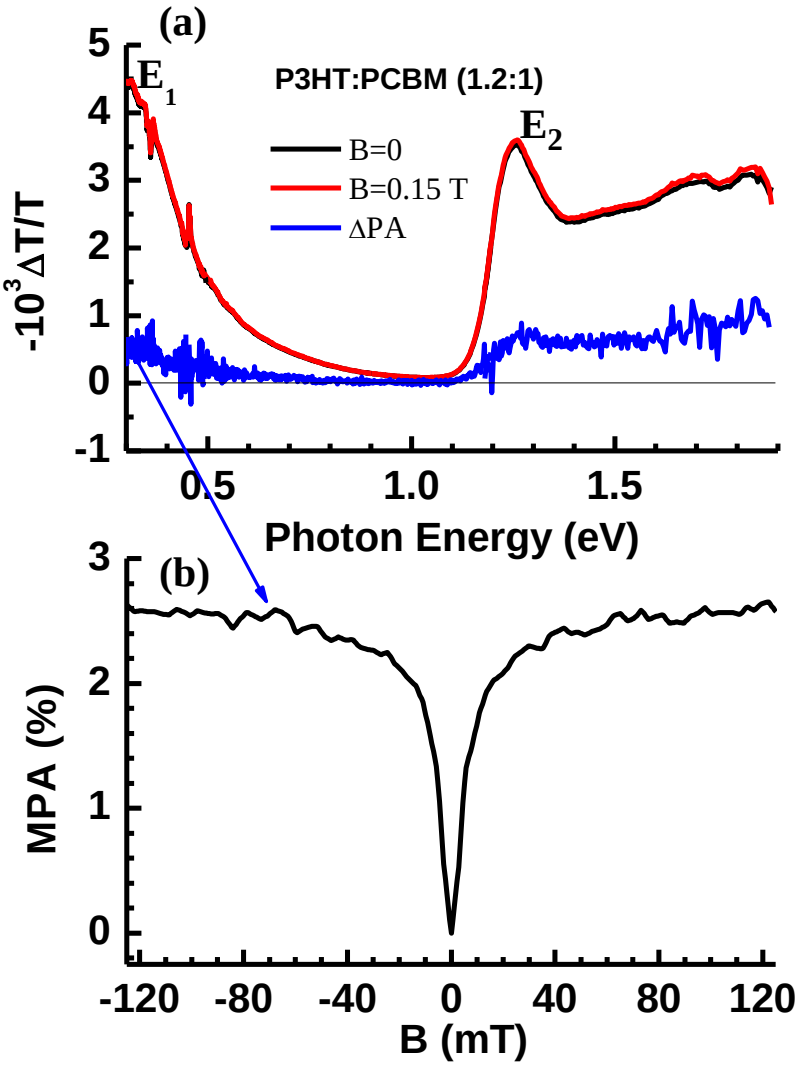

Figure 5.16 PA spectra of a ~100 nm thick film of P3HT/PCBM (1.2:1 by weight) blend at B=0 (black line) and B=150 mT (red line). The difference ΔPA (enlarged) is plotted as a blue line (a). The MPA(B) response monitored at E_1=0.35 eV (b).

(a) displays the measured steady state PA spectrum of the film at B_1=0. The PA measures the steady state absorber density, and because of the efficient charge separation, the PA spectrum shows primarily the long-lived polaron bands that appear here at E_1~0.35 eV and E_2~1.3 eV. At B_2=0.15 T, the PA spectrum (Figure 5.16 (a), red line) has nearly identical shape, but it is slightly larger. The difference $\Delta PA(B_2)=PA(B_2)-PA(0)$ (Figure 5.16 (a), blue line) is positive and shows clearly the two polaron bands. The MPA response measured at the lower energy (E_1) polaron band and defined as $MPA(B)=\Delta PA(B)/PA(0)$ is shown in Figure 5.16 (b). The response is characterized by a relatively narrow line (FWHM~12 mT) that gets saturated for B>~50 mT. This is typical to PP magnetic field response in which the HF interaction is the primary spin mixing mechanism [33]. It is thus unlikely that the broad nonsaturating $MPC_W(B)$ response comes from spin mixing within long-lived polaron pairs.

The broad and nonsaturating MPC response presented in Figures 5.11-5.15 is a "high-field" effect in the sense that considerable changes in MPC occur in magnetic fields much higher than fields that correspond to either the HFI coefficient *a* or triplet ZFS parameters (*D* and *E*) or the exchange interaction constant *J*. The expected response due to either of these interactions should saturate for $|B|>a/g\mu_B$ or $D/g\mu_B$ or $J/g\mu_B$. For pairs of spins (e.g., radical pairs, PP or CTC) that are constituted of two spin ½ species with different g-factors, a known spin mixing mechanism which in fact is more efficient at higher fields is the so called "Δg mechanism" [28, 31, 106, 107]. From the classical point of view, for $B\neq0$, the nonidentical precession frequencies of the two individual spins transform a singlet pair state to a triplet pair state and vice versa [83] at a rate $2\Delta\omega_p=2\ \mu_B\ \Delta gB/\hbar$. As *B* increases, $\Delta\omega_p$ increases too and when the pair dissociation or

recombination rate is spin-dependent, the photo-current varies with *B*. This mechanism is more effective at higher fields, giving rise to the observed "high-field" effect.

As pointed out above, the MPC (B) response can be viewed as composed of two separate contributions: a broad MPC_W and a narrow MPC_N component. The narrow component MPC_N can be accounted for by spin mixing due to the HFI within long-lived PP. This interpretation is strengthened by the observation of a narrow MPA(B) positive response measured on P3HT/PCBM blend (Figure 5.16). Such a narrow MPA response was shown before [72] to arise from long lived PP.

We propose that the broad MPC_W component arises from spin mixing due to the Δg mechanism. The g-factors for photoinduced positive and negative polarons in the RR P3HT/PCBM blends were measured by light induced electron spin resonance technique [108]: $g(P^+)=2.0017$ and $g(P^-)=1.9997$. Therefore, with $\Delta g=2.0017-1.9997=0.002$, the MPC_W response with width larger than $B_W>0.5$ T can be explained if the species decay time $\tau<\hbar/(\Delta g \mu_B B_W)=10$ ns (detailed calculation including the dispersive relaxation is not shown here). The effective dissociation time of PP is much longer (>1 μs) [6]; thus, it is not likely that PP are responsible for the broad MPC_W component. We therefore further propose that the Δg mechanism operates within the CTC that are known to exist as an intermediate short lived transitory step between the strongly bound photoexcited SE and fully separated charges contributing to the photocurrent. Indeed, recent studies revealed that CTC decay on a sub-ns time scale [109] via either dissociation, directly or indirectly, to separate free charges or by recombination that decreases the photocurrent and thereby the cell efficiency. Since the magnitude of the response still increases at B>0.2 T (Figures 5.11-5.15), the CTC decay time must be much shorter than 10 ns. Furthermore, if the

CTC decay time is indeed in the sub-ns range [109], say of the order of $\tau \approx 1$ ns, then we expect the MPC HWHM to be ≈ 5 T and to reach saturation above 10 T.

5.2.4 Conclusion

The magneto-photocurrent (MPC) response of bulk heterojunction organic photovoltaic cells is found to be nonsaturating with increasing magnetic field up to at least B~300 mT. We attribute the observed broad MPC to short-lived charge transfer complex species where spin mixing is caused by the difference Δg of the donor/acceptor g factors; a mechanism that is increasingly more effective with increasing magnetic field. On the other hand, the observed small magnitude narrow component can be accounted by spin mixing due to the HFI within long lived PP.

CHAPTER 6

CONCLUSION

In this thesis work, we studied the magnetic field effect on various organic films and devices, including organic light emitting diodes (OLEDs) and organic photovoltaic (OPV) cells.

To unravel the role of the hyperfine interaction in determining the magnetic field effect (MFE) response in organic devices, we studied magneto-conductance (MC) and magneto-electroluminescence (MEL) response in a number of *unipolar* and *bipolar* organic diodes based on π-conjugated polymers and small molecules. We found that in addition to regular MFE at intermediate fields (<100 mT), there also exists an ultra-small magnetic field effect (USMFE) at very low fields ($|B|$<1-2 mT). We measured the MFE response of three isotopes of DOO-PPV and showed that the characteristic width (ΔB) of normal MFE and the position of the dip or peak (B_m) of USMFE are isotope-dependent. Also, the USMFE component scales with the regular MFE response, and hence is due to the HFI influence on the spin polaron pair. Isotope-dependent ΔB and B_m indicate that HFI plays a crucial role in determining MFE response of organic diodes. No electroluminescence was detected in the unipolar devices, since electron-hole pairs are not formed here, in contrast with the bipolar devices. Negative MC was observed in both e-unipolar and h-unipolar diodes. In addition, the width ΔB of e-unipolar device is larger

than the h-unipolar device, indicating a larger hyperfine constant for the electron polaron than the hole polaron. We found that B_m scales with ΔB also in unipolar devices. In addition, our findings show that via the USMFE component, relatively small *B* is capable of substantially altering both electrical and electro-optical response in organic diodes, as well as *chemical, and biological reactions.*

Performance of the organic diodes can be dramatically changed by the prolonged illumination of the organic layer. We found at least two times enhancement in MC of bipolar devices, and sign reversal in h-unipolar devices upon illumination. Positive MC observed in irradiated unipolar devices supports the polaron-pair mechanism.

We studied magneto-photoinduced absorption (MPA) and magneto-photoluminescence (MPL) responses in a derivative of poly(phenylene vinylene), namely MEH-PPV, which is a well-known π-conjugated polymer, in three different forms, namely: pristine film; film exposed to prolonged UV illumination; and electron donor in MEH-PPV/PCBM blend having weight ratio 1:1. Laser excitation intensity (I_L)-dependent MPA response was observed in pristine MEH-PPV, which can be explained by two different spin mixing mechanisms: one that dominates at low I_L, this is a 'single-TE' mechanism; and the other that increases at large I_L, and therefore involves 'triplet-triplet annihilation' (TTA) mechanism. We observed the positive, monotonically increasing MPA response similar to the MC or MEL responses of a diode with the same active layer (namely MEHPPV). We found that the MPA and MC responses of MEHPPV blend have two components: a low-field component that sharply decreases with *B*, followed by a high-field component that increases slowly with *B.* Owing to the finite Δg for the polarons in the blend, the observed MPA(*B*) and MC(*B*) response can be

accounted for the PP model that includes the HFI (low-field component) and Δg mechanism (high-field component). The ultra-small magnetic field effect at B<1-2 mT in organic diodes is also observed in the MPA response of the irradiated MEH-PPV and blended films that support polaron photoexcitations, thereby identifying the underlying mechanism as being due to spin-mixing of polaron-pairs by the hyperfine interaction. By directly comparing the MPA and MPL responses in films to those of MC and MEL in organic diodes based of the same organic active layer, we are able to relate the magnetic field effect in organic diodes to the spin *densities* of the excitations formed in the device, regardless of whether they are formed by photon absorption or carrier injection from the electrodes.

We also performed spectroscopy of the MFE, including MPA and MPL at steady state conditions in annealed and pristine fullerene C_{60} thin films, as well as MC in organic diodes based on C_{60} interlayer. The hyperfine interaction has been shown to be the primary spin mixing mechanism for the MFE in the organics. In this respect, C_{60} is a unique material because 98.9% of the carbon atoms are ^{12}C isotope, having spinless nucleus and thus lacking hyperfine interaction. In spite of this, we obtained substantial MPA (up to ~15%) and significant MC and MPL in C_{60} films and devices, and thus, mechanisms other than the hyperfine interaction are responsible for the MFE in this material. Specifically, we found that the MFE(*B*) response is composed of narrow (~10 mT) and broad (>100 mT) components. The narrow MFE(*B*) component is due to spin-dependent triplet exciton recombination in C_{60}, which dominates the MPA(*B*) response at low pump intensities in films, or the MC response at small current densities in devices. In contrast, the broad MFE(*B*) component dominates the MPA(*B*) response at high pump

intensities (or large current densities for MC(*B*)), and is attributed to spin mixing in the polaron pairs spin manifold due to g-factor mismatch between the electron- and hole-polarons in C_{60}.

We fabricated organic solar cells based on bulk heterojunction of P3HT:PCBM (1.2:1) blend doped with galvinoxyl spin ½ radical. We performed both power conversion efficiency (PCE) and magneto-photocurrent (MPC) measurements in the fabricated OPV devices to unravel the underlying mechanism for possible increase in short circuit current density (*J*sc) and hence PCE with radical wt%. We found that the MPC reduction with galvinoxyl wt% follows the same trend as that of the PCE enhancement. With MPC and other control experiments such as X-ray diffraction, photoluminescence, absorption, and external quantum efficiency (EQE), we conclude that galvinoxyl spin ½ radical additives act as spin flip initiator rather than donor or acceptor. We demonstrated that the spin ½ radicals facilitate the intersystem crossing of polaron pairs (PP) from singlet to triplet spin configuration, thereby enhancing the PP separation into free charges in the device.

In order to address the role of charge transfer complex (CTC) in OPV cells, we fabricated a series of OPV cells made of blends of various organic donors and PCBM and studied the effect of magnetic field on their photocurrent. The magneto-photocurrent (MPC) response on these devices is composed of two separate contributions: a broad nonsaturating component, i.e., MPC_W and a narrow MPC_N component. We attribute the observed broad MPC to short-lived charge transfer complex species where spin mixing is caused by the difference Δg of the donor/acceptor g factors and narrow component due to HFI within long-lived PPs.

APPENDIX

LIST OF PUBLICATIONS

1. Organic bulk heterojunction solar cells enhanced by spin interaction, Y. Zhang, **B. R. Gautam**, T. P. Basel, D. J. Mascaro, and Z. V. Vardeny, *Synthetic Metals,* **173,** 2-9 (2013).

2. Magnetic field effect spectroscopy of C_{60}-based films and devices which lack hyperfine interaction, **B. R Gautam,** T. D. Nguyen, E. Ehrenfreund, and Z. V. Vardeny, *Journal of Applied Physics*, **113**,143102 (2013).

3. Spin-enhanced organic bulk heterojunction photovoltaic solar cells, Y. Zhang, T. P. Basel, **B. R. Gautam**, X. Yang, D. J. Mascaro, F. Liu, and Z. V. Vardeny, *Nature Communications*, **3**, 1043 (2012).

4. Magnetic field effect on excited state spectroscopies in organic semiconductor films, **B. R Gautam,** T. D. Nguyen, E. Ehrenfreund, and Z. V. Vardeny, *Physical Review B* **85**, 205207 (2012).

5. Magneto-conductance of π-conjugated polymer based unipolar and bipolar diodes, T. D. Nguyen, **B. R. Gautam**, E. Ehrenfreund, and Z. V. Vardeny, *Synthetic Metals,* **161**, 604 (2011).

6. Magnetoconductance response in unipolar and bipolar organic diodes at ultrasmall fields, T. D. Nguyen, **B. R. Gautam**, E. Ehrenfreund, and Z. V. Vardeny, *Physical Review Letters*, **105**, 166804 (2010).

REFERENCES

[1] H. Shirakawa, E. J. Louis, A. G. MacDiarmid, C. K. Chiang and A.J. Heeger. J. Chem. Soc., Chem. Commun**. 578** (1977).

[2] J. H. Burroughes, D. D. C. Bradley, A. R. Brown, R. N. Marks, K. Mackay, R. H.Friend, P. L. Burns, and A. B. Holmes, *Nature*, **347**, 539 (1990).

[3] D. Braun and A. J. Heeger, Appl. Phys. Lett. **58**, 1982 (1991).

[4] Z. Bao, Organic Field-Effect Transistors, CRC Press, Boca Raton (2007).

[5] J. Peet, J. Y. Kim, N. E. Coates, W. L.MA, D. Moses, A. J. Heeger, and G. C. Bazan, *Nat. Mater.* **6**, 497-500 (2007).

[6] N. S. Sariciftci, L. Smilowitz, A. J. Heeger, and F. Wudl, Science **258,** 1474 (1992).

[7] Z. H. Xiong, D. Wu, Z. V. Vardeny and J. Shi, Nature **427** (6977), 821-824 (2004).

[8] V. Dediu, M. Murgia, F. C. Matacotta, and S. Barbanera. Solid State Commun. **122**, 181 (2002).

[9] W.J. Baker, K. Ambal, D.P. Waters, R. Baarda, H. Morishita, K. van Schooten, D.R. McCamey, J.M. Lupton and C. Boehme, Nat. Commun. **3**, 898 (2012).

[10] A. J. Heeger, S. Kivelson, J. R. Schrieffer, and W. P. Su, Reviews of Modern Physics, **60**,781 (1988).

[11] W. P. Su, J. R. Schrieffer, and A. J. Heeger, Physical Review B **22** 2099 (1980).

[12] S. Mazumdar and S. N. Dixit, Physical Review Letters 51 (1983) 292.

[13] F. J. Wang, Ph.D thesis, University of Utah, 2009.

[14] D. K. Campbell and A. R. Bishop, Nuclear Physics B **200** 297 (1982).

[15] H. Bässler, Phys. Stat. Sol. (b) **175**, 15 (1993).

[16] A. Miller and E. Abrahams, Phys. Rev. 120, 745 (1960).

[17] C. W. Tang and S. A. Van Slyke. Appl. Phys. Lett., **14**, 913 (1987).

[18] U. Niedermeier,. Ph.D. thesis, Technische Universitat Darmstadt (2010).

[19] O. Mermer, G. Veeraraghavan, T. L. Francis, Y. Sheng, D. T. Nguyen, M. Wohlgenannt, A. Kohler, M. K. Al-Suti and M. S. Khan, Phys. Rev. B **72**, 205202 (2005).

[20] Y. Iwasaki, T. Osasa, M. Asahi, M. Matsumura, Y. Sakaguchi and T. Suzuki, Phys. Rev. B **74**, 195209 (2006).

[21] V. Prigodin, J. Bergeson, D. Lincoln, and A. Epstein, Synth. Met. **156**, 757 (2006).

[22] P. Desai, P. Shakya, T. Kreouzis, W. P. Gillin, N. A. Morley and M. R. J. Gibbs, Phys. Rev. B **75** (9), 094423 (2007).

23] Y. Wu, Z. Xu, B. Hu, and J. Howe, Phys. Rev. B **75**, 035214 (2007).

[24] P. A. Bobbert, T. D. Nguyen, F. W. A. v. Oost, B. Koopmans and M. Wohlgenannt, Phys. Rev. Letters **99**, 216801 (2007).

[25] F. L. Bloom, W. Wagemans, M. Kemerink, and B. Koopmans, Phys. Rev. Lett. **99**, 257201 (2007).

[26] B. Hu and Y. Wu, Nature Mater. **6**, 985 (2007).

[27] J. D. Bergeson, V. N. Prigodin, D. M. Lincoln and A. J. Epstein, Phys. Rev. Letters **100**, 067201 (2008).

[28] F. Wang, H. Bassler, and Z. V. Vardeny, Phys. Rev. Lett. **101,** 236805 (2008).

[29] S. Majumdar, H. S. Majumdar, H. Aarnio, and R. Osterbacka, Phys. Status Solidi RRL **3**, 242-244 (2009).

[30] F. L. Bloom, M. Kemerink, W.Wagemans, and B. Koopmans, Phys. Rev. Lett. **103**, 066601 (2009).

[31] H. Hayashi, *Introduction to dynamic spin chemistry; MFE and biochemical reactions,* World Scientific Lecture and Course Notes in Chemistry Vol. 8 (2004).

[32] T. D. Nguyen, Y. Sheng, J. Rybicki and M. Wohlgenannt, Phys. Rev. B **77**, 235209 (2008).

[33] T. D. Nguyen, G. Hukic-Markosian, F. J. Wang, L. Wojcik, X. G. Li, E. Ehrenfreund and Z. V. Vardeny, Nat Mater **9** (4), 345-352 (2010).

[34] C. W. Tang, Appl. Phys. Lett. **48**, 183 (1986).

[35] J. You, L. Dou, K. Yoshimura, T. Kato, K. Ohya, T. Moriarty, K. Emery, C. Chen, J. Gao, G. Li and Y. Yang, Nat. Commun. **4**, 1446 (2013).

[36] S. Singh, B. Pandit, T. P. Basel, S. Li, D. Laird, and Z. V. Vardeny, Phys. Rev. B **85,** 205206 (2012).

[37] A. A. Bakulin, A. Rao, V. G. Pavelyev, P. H. M. van Loosdrecht, M. S. Pshenichnikov, D. Niedzialek, J. Cornil, D. Beljonne and R. H. Friend, Science, **335**, 1340 (2012).

[38] J. J. Benson-Smith, L. Goris, K. Vandewal, K. Haenen, J. V. Manca, D. Vanderzande, D. D. C. Bradley, and J. Nelson, Adv. Funct. Mater.**17**, 451 (2007).

[39] T. Drori, J. Holt, Z. V. Vardeny, Physical Review B **82,** 075207 (2010).

[40] P. W. M. Blom, M. J. M de Jong, and J. J. M. Vleggaar, Appl. Phys. Lett. **68**, 3308-3310 (1996).

[41] R. H. Parmenter and W.Ruppel, J. Appl. Phys. **30**, 1548-1558 (1959).

[42] T. D. Nguyen, B. R. Gautam, E. Ehrenfreund and Z. V. Vardeny, Phys. Rev. Lett. **105** (16) (2010).

[43] B. Brocklehurst, J.Chem.Soc. Faraday Trans II, **72**, 1869 (1976).

[44] I.A. Shkrob, V. F. Tarasov, and A. L. Buchachenko, Chem. Phys., **153**, 443 (1991).

[45] V. O. Saik and S. Lipsky, Chem. Phys. Lett., **264**, 649 (1997).

[46] D. R. McCamey, K. J. van Schooten, W. J. Baker, S.-Y. Lee, S.-Y. Paik, J. M. Lupton, and C. Boehme, Phys. Rev. Lett. **104**, 017601 (2010).

[47] D. R. McCamey, H. A. Seipel, S.-Y. Paik, M. J. Walter, N. J. Borys, J. M. Lupton & C. Boehme, Nature Mater. **7**, 723 (2008.

[48] C. R. Timmel, U. Till, B. Brocklehurst, K. A. Malauchlan, and P. J. Hore, *Mole. Phys.* **95**, 71 (1998).

[49] T. Drori, E. Gershman, C. X. Sheng, Y. Eichen, Z. V. Vardeny and E. Ehrenfreund, Phys. Rev. B **76**, 033203 (2007).

[50] J. Rybicki et, R. Lin, F. Wang, M. Wohlgenannt, C. He, T. Sanders, and Y. Suzuki, Phys. Rev. Lett. **109**, 076603 (2012).

[51] U. Niedermeier, M. Vieth, R. Patzold, W. Sarfert, and H. von Seggern, Appl. Phys. Lett., **92**, 193303 (2008).

[52] S. A. Bagnich, U. Niedermeier, C. Meizer, W. Sarfert, and H. von Seggern, J. Appl. Phys., **105**, 123706 (2009).

[53] B. Hu, L. Yan and M. Shao, Adv Mater **21**, 1500–1516 (2009).

[54] F. Wang, J. Rybicki, K. A. Hutchinson and M. Wohlgenannt, Phys. Rev. B **83** (24), 241202 (2011).

[55] R. E. Merrifield, Pure and Applied Chemistry **27**, 481-498 (1971).

[56] J. Rybicki, T. D. Nguyen, Y. Sheng and M. Wohlgenannt, Synthetic Met **160**, 280-284 (2010).

[57] T. D. Nguyen, J. Rybicki, Y. Sheng and M. Wohlgenannt, Phys. Rev. B **77**, 035210 (2008).

[58] T. D. Nguyen, B. R. Gautam, E. Ehrenfreund and Z. V. Vardeny, Synthetic Met **161**, 604-607 (2011).

[59] K. Maeda, K. B. Henbest, F. Cintolesi, I. Kuprov, C. T. Rodgers, P. A. Liddell, D. Gust, C. R. Timmel and P. J. Hore, Nature **453**, 387-391 (2008).

[60] X. Wei, Z. V. Vardeny, N. S. Sariciftci and A. J. Heeger, Phys Rev B **53** (5), 2187 (1996).

[61] A. Konkin, U. Ritter, P. Scharff, H. K. Roth, A. Aganov, N. S. Sariciftci and D. A. M. Egbe, Synthetic Met **160** (5-6), 485-489 (2010).

[62] T. D. Nguyen, G. Hukic-Markosian, X.-G. L. F. Wang, E. Ehrenfreund and Z. V. Vardeny, Synthetic Met **161**, 598-603 (2011).

[63] J. Kalinowski, M. Cocchi, D. Virgili, P. Di Marco and V. Fattori, Chem Phys Lett **380** (5-6), 710-715 (2003).

[64] J. Tang and J. R. Norris, Chem Phys Lett **92** (2), 136-140 (1982).

[65] X. Wei, B. C. Hess, Z. V. Vardeny and F. Wudl, Phys Rev Lett **68** (5), 666 (1992).

[66] T. L. Francis, Ö. Mermer, G. Veeraraghavan and M. Wohlgenannt, New J Phys **6**, 185 (2004).

[67] B. Koopmans, W. Wagemans, F. L. Bloom, P. A. Bobbert, M. Kemerink and M. Wohlgenannt, Phil. Trans. R. Soc. A **369** 3602-3616 (2011).

[68] T. D. Nguyen, T. P. Basel, Y.-J. Pu, X.-G. Li, E. Ehrenfreund and Z. V. Vardeny, Phys. Rev. B **85**, 245437 (2012).

[69] A. Carrington and A. D. McLachlan, *Introduction to magnetic resonance*. (Harper & Row, New York, 1967).

[70] I. V. Khudyakov, Y. A. Serebrennikov and N. J. Turro, Chem. Rev. **93**, 537-570 (1993).

[71] U. E. Steiner and T. Ulrich, Chem. Rev. **89**, 51-147 (1989).

[72] B. R. Gautam, T. D. Nguyen, E. Ehrenfreund and Z. V. Vardeny, Phys. Rev. B **85**, 205207 (2012).

[73] A. Abragam and B. Bleaney, *Electron Paramagnetic Resonance of Transition Ions*. (Clarendon Press Oxford, 1970).

[74] D. Dick, X. Wei, S. Jeglinski, R. E. Benner, Z. V. Vardeny, D. Moses, V. I. Srdanov and F. Wudl, Phys. Rev. Letters **73**, 2760-2763 (1994).

[75] X. Wei, Z. V. Vardeny, D. Moses, V. I. Srdanov and F. Wudl, Synthetic Met **54**, 273-279 (1993).

[76] P. A. Heiney, J. E. Fischer, A. R. McGhie, W. J. Romanow, A. M. Denenstein, J. P. McCauley Jr, A. B. Smith and D. E. Cox, Phys Rev Lett **66** (22), 2911-2914 (1991).

[77] P. A. Lane, L. S. Swanson, Q. X. Ni, J. Shinar, J. P. Engel, T. J. Barton and L. Jones, Phys Rev Lett **68** (6), 887-890 (1992).

[78] X. Wei and Z. V. Vardeny, Phys. Rev. B **52**, R2317-R2320 (1995).

[79] E. Ehrenfreund and Z. V. Vardeny, Israel Journal of Chemistry **52**, 552-562 (2012).

[80] P.-M. Allemand, G. Srdanov, A. Koch, K. Khemani, F. Wudl, Y.Rubin, F. Diederich, M. M. Alvarez, S. J. Anz and R. L. Whetten, J. Am. Chem. Soc. **113**, 2780-2781 (1991).

[81] R. A. J. Janssen, J. C. Hummelen, K. Lee, K. Pakbaz, N. S. Sariciftci, A. J. Heeger and F. Wudl, J. Chem. Phys. **103**, 788-793 (1995).

[82] L. Dunsch, F. Ziegs, C. Siedschlag and J. Mattay, Chem. Eur. J **6**, 3547-3550 (2000).

[83] N. J. Turro, Proc. Natl. Acad. Sci. **80**, 609-621 (1983).

[84] J. You, L. Dou, K. Yoshimura, T. Kato, K. Ohya, T. Moriarty, K. Emery, C. Chen, J. Gao, G. Li and Y. Yang, Nat. Commun. **4**, 1446 (2013).

[85] J. Behrends, A. Sperlich, A. Schnegg, T. Biskup, C. Teutloff, K. Lips, V. Dyakonov, and R. Bittl, Physical Review B 85, 125206. (2012).

[86] J. Holt, S. Singh, T. Drori, Y. Zhang, and Z. V. Vardeny, *Phys. Rev. B* **79**, 195210 (2009).

[87] D. H. Wang, J. S. Moon, J. Seifter, J. Jo, J. H. Park, O. O. Park, and A. J. Heeger, *Nano Lett.* **11**, 3163-3168 (2011).

[88] M.D. Perez, C. Borek, S.R. Forrest, M.E. Thompson, J. Am. Chem. Soc. **131** 9281–9286 (2009.

[89] Y. Liang, Z. Xu, J. Xia, S. T. Tsai, Y. Wu, G. Li, C. Ray and L. Yu, Adv. Energy Mater. **22**, E 135- E 138 (2010).

[90] K. Vandewal, K. Tvingstedt, A. Gadisa, O. Inganas, J.V. Manca, Nature Materials **8** (2009) 904–909.

[91] R. B Ross, C. M. Cardona, D. M. Guldi, S. G. Sankaranarayanan, M. O. Reese, N. Kopidakis, J. Peet, B. Walker, G. C. Bazan, E. V. Keuren, B. C Holloway, and M. Drees, *Nat. Mater.* **8**, 208-212 (2009).

[92] C. J. Ko, Y. K. Lin, F. C. Chen, and C. W. Chu, *Appl. Phys. Lett.* **90** (2007).

[93] J. Y. Kim, K. Lee, N. E. Coates, D. Moses,T.Q. Nguyen, Mark Dante, A. J. Heeger, *Science* **317**, 222-225 (2007).

[94] S. H. Park, A. Roy, S. Beaupre, S. Cho, N. Coates, J. S. Moon,D. Mose, M. Leclerc, K. Lee and A. J. Heeger, *Nat. Photonics* **3**, 297-302 (2009).

[95] F. Deschler, E. D. Como, T. Limmer, R. Tautz, T. Godde, M. Bayer, E. von Hauff, S. Yilmaz, S. Allard, U. Scherf, and J. Feldmann, Phys. Rev. Lett. **107** 127402 (2011).

[96] G. Dennler, M. C. Scharber, and C. J. Brabec, Adv. Mat. **21**, 1323-1338 (2009).

[97] I. Novak and B. Kovac, *Chem. Phys. Lett.* **413**, 351-355 (2005).

[98] R. Tipnis, D. Laird, and M. Mathai, *Material Matters* **3**, 92 (2008).

[99] P. Shakya, P. Desai, T. Kreouzis, W.P. Gillin, S.M. Tuladhar, A.M. Ballantyne, and J. Nelson, Journal of Physics: Condensed Matter 20 (2008) 452203.

[100] H. Zang, Z. Xu, B. Hu, The Journal of Physical Chemistry B **114** 5704–5709 (2010).

[101] Y. Lei, Q. Song, Y. Zhang, P. Chen, R. Liu, Q. Zhang, and Z. Xiong, Organic Electronics **10** (2009) 1288–1292.

[102] J. Clark, C. Silva, R.H. Friend, F.C. Spano, Physical Review Letters **98**, 206406 (2007).

[103] Y. Kouhei, H. Kamioka, T. Yasuda, L. Han, and Y. Moritomo, Appl. Phys. Express, **5**, 042302 (2012).

[104] T. M. Clarke and J. R. Durrant, *Chemical Reviews* **110**, 6736-6767 (2010).

[105] L. S. Swanson, J. Shinar, and K. Yoshino, *Phys. Rev. Letters* **65**, 1140-1143 (1990).

[106] Y. Tanimoto, H. Hayashi, S. Nagakura, H. Sakuragi, and K. Tokumaru, *Chem. Phys. Letters* **41**, 267-269 (1976).

[107] K. Schulten, and I. R. Epstein, *J. Chem. Phys.* **71**, 309-316 (1979).

[108] V. I. Krinichnyi, E. I. Yudanova, and N. G. Spitsina, *Journal of Physical Chemistry C* **114**, 16756-16766 (2010).

[109] G. Grancini, D. Polli, D. Fazzi, J. Cabanillas-Gonzalez, G. Cerullo, and G. Lanzani, *J. Phys. Chem. Lett.* **2**, 1099-1105 (2011).